Perovskite-Like Layered Structure $A_2B_2O_7$ Ferroelectrics and Solid Solutions

Zhipeng Gao

A thesis submitted for the degree of Doctor of Philosophy

School of Engineering and Materials Science,
Queen Mary, University of London
November 2012

Abstract

In this project, the ferroelectric materials $Pr_2Ti_2O_7$, $La_2Ti_2O_7$, $Sr_2Nb_2O_7$, $La_{2-x}Ce_xTi_2O_7$ (x=0.15, 0.25, 0.35), $Nd_{2-x}Ce_xTi_2O_7$ (x=0.05, 0.25, 0.5, 0.75) and $Sr_{2-x}Ba_xNb_2O_7$ (x=0.1, 0.2, 0.3, 0.4, 0.5) were investigated. They have a provskite-like layered structure (PLS), and are well known for their super-high Curie points (>1200 ˚C). Their ceramics were fabricated using Spark Plasma Sintering.

For $Pr_2Ti_2O_7$, single phase, dense and textured ceramics were prepared. The Curie point is greater than 1560 ℃ which is the highest known Curie Point so far for ferroelectric materials. $Pr_2Ti_2O_7$ was shown for the first time to be ferroelectric because it showed piezoelectric activity after poling.

For the $La_{2-x}Ce_xTi_2O_7$ solid solution system, the ferroelectric and dielectric properties of cerium (Ce) substituted $La_2Ti_2O_7$ (LTO) were investigated. The solubility limit of Ce in $La_{2-x}Ce_xTi_2O_7$ was found to be between 0.35 and 0.5 supported by XRD results. The a-, b- and c-axes of the unit cell decrease with increasing Ce substitution. The Curie points (Tc) of $La_{2-x}Ce_xTi_2O_7$ (x=0, 0.15, 0.25, 0.35) also decreases. The dielectric constant and loss increase with increasing Ce substitution. Electrical resistivity decreases due to Ce substitution. Cerium can increase the d_{33} of $La_2Ti_2O_7$. The highest d_{33} was 3.9 ± 0.1pC/N for $La_{1.85}Ce_{0.15}Ti_2O_7$. In the $Nd_{2-x}Ce_xTi_2O_7$ system, the cell volume increases from $Nd_2Ti_2O_7$ to $Nd_{1.25}Ce_{0.75}Ti_2O_7$ and the Curie point (Tc) decreases with Ce increase.

For the $Sr_{2-x}Ba_xNb2O_7$ solid solution system, the effect of Ba substitution on the structure and ferroelectric properties of $Sr_{2-x}Ba_xNb_2O_7$ (x<1.0) was investigated. The a-, b-, c- axes and cell volume increase with Ba addition because Ba^{2+} is a relatively large ion. A atomic displace move model was developed to explain the spontaneous lattice strain, spontaneous polarization and Curie point change in the orthorhombic phase ($Cmc2_1$) with increasing Ba substitution. The critical point of $Sr_{2-x}Ba_xNb_2O_7$ solid solution (x<0.6) was determined by XRD and was supported by the XPS spectra of Ba 2p and O 1s. Textured ceramics of $Sr_{2-x}Ba_xNb_2O_7$ compounds were prepared using the spark plasma sintering technique and the piezoelectric activity can be improved by Ba substitution, which increases the domain switch mobility. The highest d_{33} was measured as 3.6 ± 0.1pC/N for $Sr_{1.8}Ba_{0.2}Nb_2O_7$.

The thermal depoling behaviors of $La_2Ti_2O_7$, and $Sr_2Nb_2O_7$ were investigated due to their relatively high d_{33} piezoelectric constant and high Curie point. Both of them have a high resistance to thermal depoling, especially $La_2Ti_2O_7$. Ginzburg - Landau theory was used to explain their behavior. The electric resistivity degradation of $Sr_2Nb_2O_7$ was studied at different temperatures, and it was found to be stable below 800 ℃.

Acknowledgement

First and foremost, I feel very privileged to have worked with my super - great supervisor, Prof. Mike Reece. I really appreciate his insightful guidance, invaluable advice and constant encouragement and support throughout the whole project. Sometimes I am annoying and down, however he is always patient and supportive.

I am also very grateful to Dr. Haixue Yan for his great help with nice suggestions and discussions about my thesis.

I am appreciate Dr. Huanpo Ning for his help with the experimental work.

I would like to thank Dr. Zofia Luklinska and Dr. Rory Wilson, for their generous help.

I wish to thank all of students in our group and my office for their consistent help and friendship.

I am deeply indebted to my parents and my girlfriend, Snow Yang for their constant support and encouragement during my PhD project.

Thanks for the financial support from Chinese Scholarship Council.

Table of Contents

Chapter I. Introduction

Ferroelectricity is a property of certain materials which possess a spontaneous electric polarization (Ps) that can be reversed by the application of an external electric field.[1] A consequence of Ps switching in ferroelectric materials is the occurrence of the ferroelectric hysteresis loop (Fig.1.1.1). Ferroelectric materials have non-centrosymmetric structures, which leads to the spontaneous polarization and ferroelectric property.[1,2] All ferroelectrics are piezoelectric materials. Piezoelectricity is the ability of certain crystalline materials to develop an electric charge proportional to an applied mechanical stress. So, some of them are good candidates for piezoelectric applications due to their sensitivity, low cost and robustness. Many of these applications can be categorized into: ignitors, displacement transducers, accelerometers, and piezoelectric sensors.[3-5] However, for all of these applications, the maximum operating temperature is limited by the "Curie point". The Curie point is the temperature at which the ferroelectric - paraelectric transition happens. Paraelectric phase has a centrosymmetric structure and no Ps, hence the paraelectric phase has no ferroelectric properties, and the Curie point sets the upper temperature limit on ferroelectric applications.[6,7] Some extreme environments, such as aerospace, and power generating industries, involve applications that require them to work up to high temperature. Therefore, ferroelectric materials with a high Curie points are desirable for high temperature applications. Some typical ferroelectric materials with high Tc (>650 ℃)

are lithium niobate, $LiNbO_3$ (Tc =1140 ℃), lithium tantalate, $LiTaO_3$ (Tc = 620 ℃), and Aurivillius phase materials, represented by $Bi_4Ti_3O_{12}$ (Tc=675 ℃) and $CaBi_2Nb_2O_9$ (Tc= 943 ℃).[5,8-11]

The perovskite-like layer structure materials with formula $A_nB_nO_{3n+2}$ are well known for their super-high Curie points (many are above 1000 ^oC). Especially, when n=4, the materials with formula of $A_2B_2O_7$, such as $Pr_2Ti_2O_7$, $Sr_2Nb_2O_7$, $Ca_2Nb_2O_7$, $La_2Ti_2O_7$ and $Nd_2Ti_2O_7$, have the highest Curie points of all ferroelectrics.[12-16] Hence, they have great potential for high temperature applications. Except their high Curie points, the $A_2B_2O_7$ ferroelectric materials have a high permittivity and relatively low loss.[11] The permittivity of a material describes how much electric field is 'generated' per unit charge in the material and it. In other words, permittivity is a measure of how an electric field affects a material.[11,12] The materials with high permittivity have a widely use in electronic industry, for example, capacitors, energy storage unit, and inductors.

However, as piezoelectric materials, the $A_2B_2O_7$ polycrystalline ceramics have a relatively small piezoelectric constant and relatively high coercive field, which makes them difficult to pole. Grains in ceramics, oriented in different directions, restrict the movement of domain walls under electrical poling, making the coercive field (Ec), which is the electric field strength required to switch the Ps, of ceramics much larger than that for single crystals.[17,18] On the other hand, ceramics have more single crystal-like properties when all of the grains are oriented (textured) in a certain direction.

There have been some techniques to make grain-oriented $A_2B_2O_7$ ceramics by texturing such as Templated Grain Growth (TGG) and Hot Working (HW), but few results have been reported on their ferroelectric properties.[19-23]

Due to their unique properties and requirements, it is very desirable to find ferroelectric materials which can be used in the extreme environment and find a proper way to fabricate. This thesis is focused on the investigation of these $A_2B_2O_7$ ceramics and their solid solutions, fabricated by spark plasma sintering (SPS) and their properties were controlled by compositional modifications. Textured ceramics were obtained by a two-step method using SPS. Their dielectric, piezoelectric and ferroelectric properties were investigated and the stability of the properties have been studied.

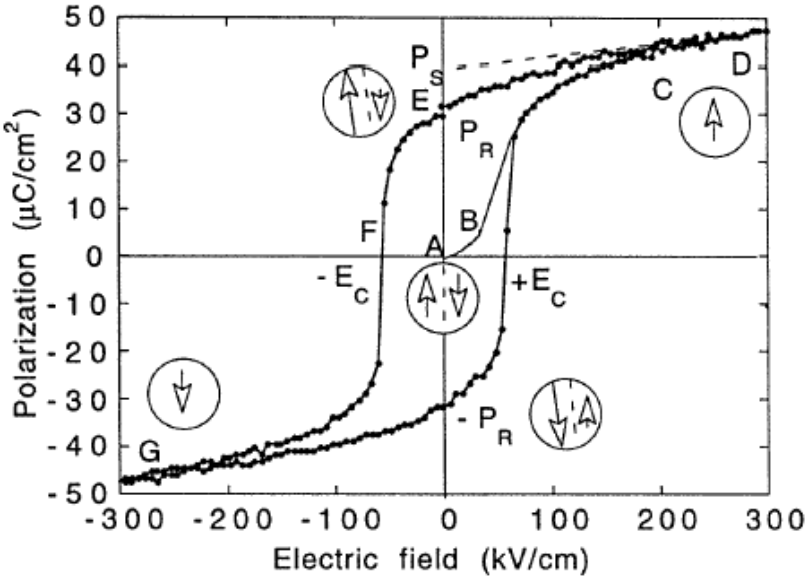

Fig.1.1.1. Typical hysteresis loop of ferroelectric materials. Circles with arrows represent the polarization state of the material at the indicated fields; Ps is spontaneous polarization; Pr is the residual polarization which is the value of polarization at zero field (point E); Ec is the field necessary to bring the polarization to zero called the coercive field,[24]

References

(1). Turner, R.C., P.A. Fuierer, R.E. Newnham, and T.R. Shrout, *Applied Acoustics*, 1994. **41**(4): p. 299-324.

(2). Damjanovic, D., *Current Opinion in Solid State and Materials Science*, 1998. **3**(5): p. 469-473.

(3). Kanzig, W., *Ferroelectrics and Antiferroelectrics*, Academic Press, 1957. 5.

(4). Lines, M., and Glass, A., *Principles and applications of ferroelectrics and related materials*, Clarendon Press, Oxford ed., 1979.

(5). Ishibashi, Y., Shiosaki, T., Yoshino, K., and Ichinose, N., *Japanese Journal of Applied Physics,* 1991. **30**: p. U2145.

(6). Jaffe, B., Cook, W., and H. Jaffe, Piezoelectric ceramics. 1971. London and New York: Academic Press.

(7). Damjanovic, D., *Reports on Progress in Physics*, 1998. **61**: p. 1267-1324.

(8). Fouskova, A., and Cross, L., *Journal of Applied Physics*, 1970. **41**(7): p. 2834-2838.

(9). Shulman, H.S., D. Damjanovic, and N. Setter, *Journal of the American Ceramic Society*, 2000. **83**(3): p. 528-532.

(10). Yan, H., Zhang, H., Ubic, R., Reece, M., Liu, J., Shen, Z., and Zhang, Z., *Advanced Material*, 2005. **17**: p. 1261-5.

(11). Yan, H., M. J. Reece, J. Liu, Z. Shen, Y. Kan, and P. Wang, *Journal of Applied Physics*, 2006. **100**(7): p. 076103-3.

(12). Kimura, M., Nanamats.S, Doi, K., Matsushi. S., Igarashi, S., and Takahash.M., *Nec Research and Development*, 1973. **17**: p. 10-14.

(13). Nanamatsu, S., and Kimura, M., *Journal of the Physical Society of Japan*, 1974. **36**: p. 1495.

(14). Kimura, M., Nanamatsu, S, Kawamura, T., and Matsushita, S., *Japanese Journal of Applied Physics*, 1974. **13**: p. 1473-1474.

(15). Nanamats, S., Kimura, M., and Yamada, N., *Nec Research and Development*, 1974. **19**: p. 39-42.

(16). Lichtenberg, F., A. Herrnberger, and K. Wiedenmann, *Progress in Solid State Chemistry*, 2008. **36**(4): p. 253-387.

(17). Shoji, K., Aikawa, M., Uehara, Y., and Sakata, K., *Japanese Journal of Applied Physics*, 1998. **37**: p. 5273-5276.

(18). Li, J., Rogan, R., Ustundag, E., and Bhattacharya, K., *Nature Materials*, 2005. **4**(10): p. 776-781.

(19). Fuierer, P., and Newnham, R., *Journal of the American Ceramic Society*, 1991. **74**(11): p. 2876-2881.

(20). Fukuhara, M., Huang, C., Bhalla, A., and Newnham, R., *Journal of Materials Science*, 1991. **26**: p. 61-66.

(21). Prasadarao, A., Selvaraj, U., Komarneni, S., and Bhalla, A., *Materials Letters*, 1991. **12**(5): p. 306-310.

(22). Messing, G., Trolier-McKinstry, S., Sabolsky, E., Duran, C., Kwon, S., Brahmaroutu, B., Park, P., Yilmaz, H., Rehrig, P., Eitel, K., Suvaci, E., Seabaugh, M., and Oh, K., *Critical Reviews in Solid State & Materials Science*, 2004. **29**(2): p. 45-96.

(23). Zhang, F., Lian, J., Becker, U., Ewing, R., Wang, L., Hu, J., and Saxena, S., *Journal of Solid State Chemistry*, 2007. **180**(2): p. 571-576.

(24). Burfoot J. C. and Taylor G. W., *Polar dielectrics and their applications*, London: Macmillan, 1979.

Chapter II. Literature Review

2.1. Perovskite and perovskite-like layer structure

The perovskite structured materials have been researched for many years because of their excellent properties. The standard structure is shown in Fig.2.1.1, B^{b+} is in the center of an oxygen octahedron while the O^{2-} are sited on the apices of octahedrons, and the positions between the octahedra are occupied by A^{a+}.

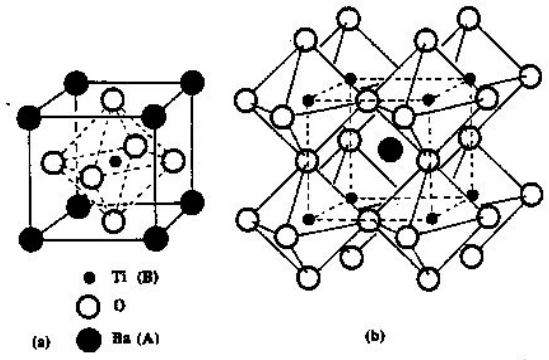

Fig.2.1.1. (a) A cubic perovskite-type unit cell($BaTiO_3$); (b) Network of O^{2-} ions octahedra in the structure.[1]

There are three different basic layered structures based on the perovskite structure (ABO_3) with oxygen rich layers. These structures are effectively produced by cutting the cubic perovskite structure accross the (100), (110), (111) planes and by insertion of additional oxygen atoms. They are known as Dion-Jacobson type structures, Perovskite-like layered structures (PLS) and hexagonal type structures, which have general forms of $A'A_{k-1}B_kO_{3k+1}$, $A_nB_nO_{3n+2}$ and $A_mB_{m-1}O_{3m}$, respectively.[2,3] The Aurivillius ferroelectrics also have a perovskite layered structure. However the structure

is described as resulting from the regular stacking of $[Bi_2O_2]^{2+}$ slabs and perovskite-like $[A_{m-1}B_mO_{3m+1}]^{2-}$ blocks.[4]

In the $A_nB_nO_{3n+2}$ formula of PLS compounds, n represents the number of BO_6 octahedra that span one layer, and therefore specifies the thickness of the perovskite-layer. Sometimes, n is non-integral due to a mixture of layers with different thicknesses, and it then indicates the average number of octahera per layer. In this structure alkaline earth or lanthanide metals often occupy the A positions while the B cations are usually titanium or niobium.[2,3,5] Some $A_nM_nO_{3n+2}$ structures are shown in Fig. 2.1.2.

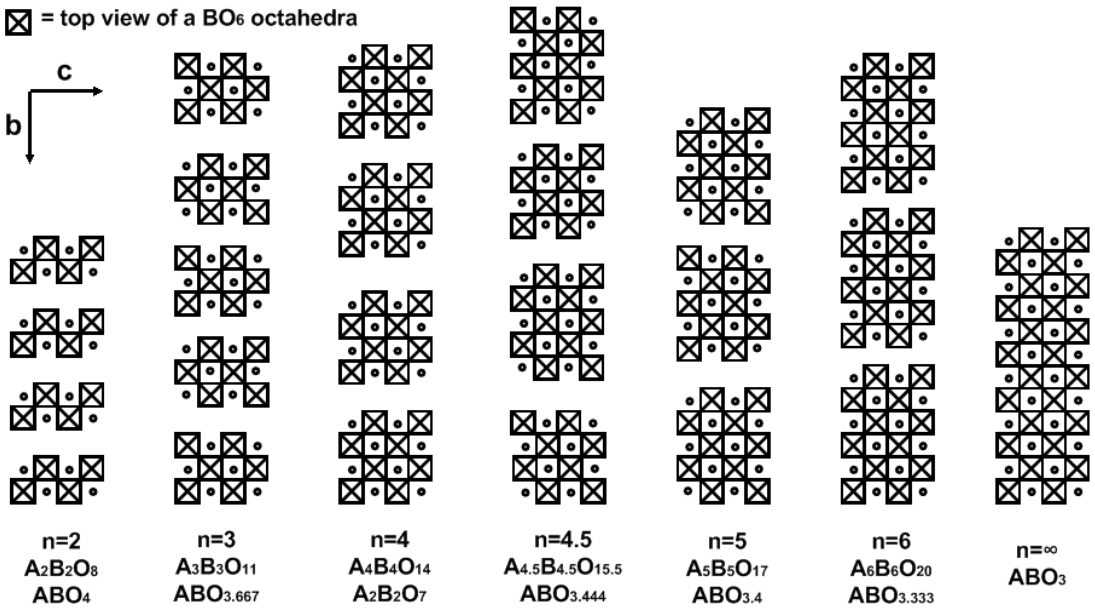

Fig.2.1.2. Skeleton diagram of the non-distorted crystal structures of $A_nB_nO_{3n+2}$ members projected along a-axis.[3]

2.2. $A_nB_nO_{3n+2}$ compounds

Though they have the same formula, the $A_nB_nO_{3n+2}$ PLS compounds have different crystallographic structures. The different crystal structures correspond to different distortions of the layers relative to the ideal centro-symmetric, orthorhombic structure. In these systems, the typical distortions are produced by tilting of the BO_6 octahedra and displacement of either or both the A and B cations.[6] Due to this, some of them have a centro-symmetric structure while some are noncentro-symmetric. An overview of the structure and properties of many $A_nB_nO_{3n+2}$ compounds is presented in Tables 2.1-2.5, 2.8 which contains the data and results of integer ratio compounds from the literature.

2.2.1. n=2 group in $A_nB_nO_{3n+2}$

For n=2 members in the $A_nB_nM_{3n+2}$ family, the formula is ABO_4. Several compounds have been investigated. $LaTaO_4$ is potentially a ferroelectric material, and has two structures, orthorhombic and monoclinic. The orthorhombic $LaTaO_4$ (O-$LaTaO_4$) has a noncentro-symmetric structure with space group $Cmc2_1$ and the lattice parameters are (a, b, c, β) = (3.92 Å, 14.70Å, 5.65 Å, 90°).[7,8] Monoclinic $LaTaO_4$ (M-$LaTaO_4$) has centro-symmetric structure with space group $P2_1/c$ and the lattice parameters are (a, b, c, β) = (7.615 Å, 5.565Å, 7.810 Å, 101.49°).[8] The monoclinic phase exists at a high temperature (>1470K) and gradually transforms into the orthorhombic phase when the temperature is below 1470 K. The rate of monoclinic to orthorhombic transformation is slow in the temperature range 423-1470 K, and decreases with decreasing temperature.

The rate of this transformation becomes negligible below 423 K.[9-11] So the two phases of orthorhombic and monoclinic $LaTaO_4$ can be observed to coexist below 423 K. The spontaneous polarization in orthorhombic $LaTaO_4$ was estimated as 1.6 $\mu C/cm^2$.[9-11] $LaTaO_4$ can be made by calcining powder mixtures of La_2O_3 and Ta_2O_3 at 1200℃-1400℃ for 10 hours.[12,13] The structure is shown in Fig.2.2.1.

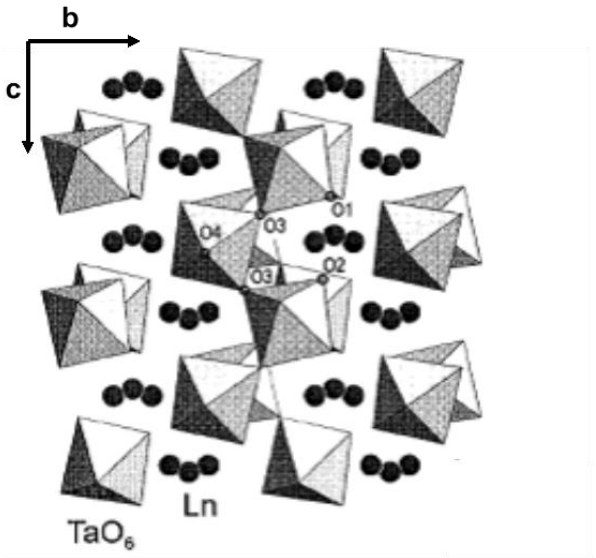

Fig.2.2.1. The structure of $LaTaO_4$ along the a axis.[14]

$LaNbO_4$ has monoclinic and orthorhombic structures.[10] $LaNbO_4$ prepared under normal pressure (LP) has I2/a space group with monoclinic structure, so it is centro-symmetric. Orthorhombic $LaNbO_4$ can be prepared through hydroxide co-precipitation and heating to 1570K with a high pressure (HP) of 8GPa. $LaNbO_4$ with orthorhombic structure is noncentro-symmetric with $Cmc2_1$ and the unit parameters are (a, b, c, β) = (3.94 Å, 14.40 Å, 5.68 Å, 90°). It potentially has ferroelectric properties and the spontaneous polarization was estimated as 2 $\mu C/cm^2$. $LaNbO_4$ (HP) can transform into $LaNbO_4$(LP)

at 870K under normal pressure. This transition is a second-order phase transition. There is no report about its ferroelectric properties.

The solid solution system of $LaNb_{1-x}Ta_xO_4$ have been investigated by X-Ray diffraction (XRD).[15] A two-phase region was observed in the composition region, $0.4<x<0.8$, at room temperature. Single-phase $LaNb_{1-x}Ta_xO_4$ ($0<x<0.4$) with the monoclinic structure (I2/a) at room temperature was observed to transform to a tetragonal structure by high-temperature XRD. The phase transition temperature was shown to increase with increasing Ta-content (Fig.2.2.2) and these phase transition are all second order (Fig.2.2.3).[15] Single-phase $LaNb_{1-x}Ta_xO_4$ ($0.8<x<1$) with a monoclinic crystal structure ($P2_1/c$) was shown to transform to an orthorhombic crystal structure by XRD and differential scanning calorimetry (DSC) (Fig.2.2.2).[15]

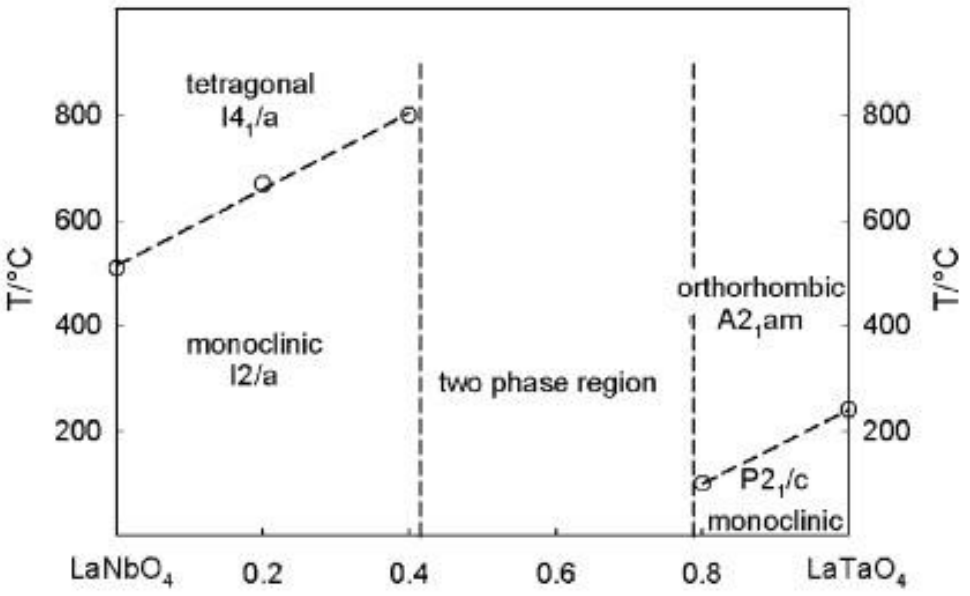

Fig.2.2.2. Phase diagram for $LaNbO_4$-$LaTaO_4$ system.[15]

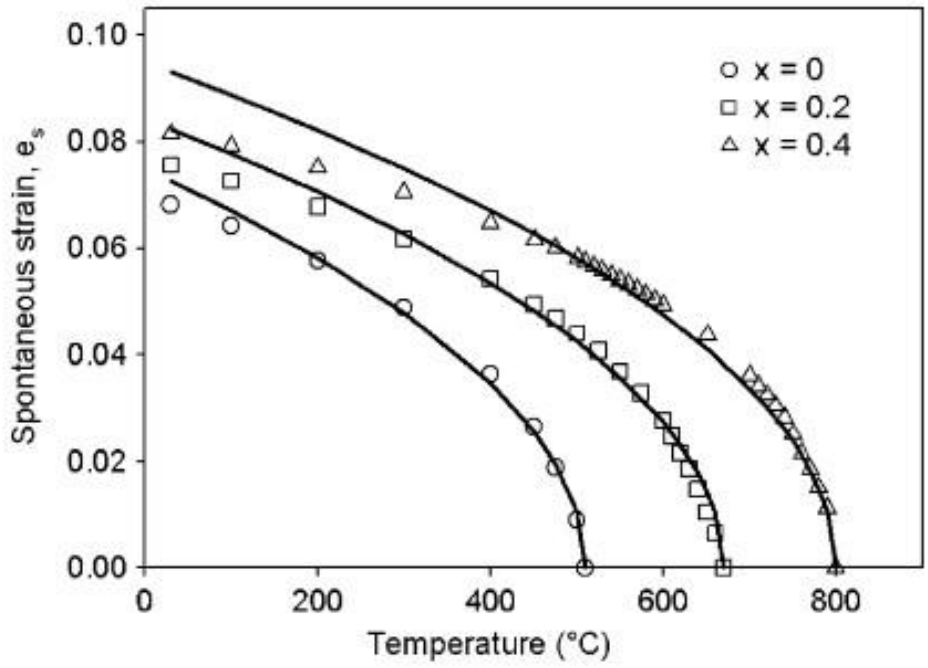

Fig.2.2.3. The relationship between spontaneous strain and temperature for $(LaNbO_4)_{1-x}(LaTaO_4)_x$ system.[15]

Table.2.1. ABO_4, n=2.

Compounds	Symmetry	Structure	Ferroelectric	Tc/℃	Space Group
$PrTaO_4$[2,16]	Centro	Monoclinic	No	N/A	$P2_1/c$
$NdTaO_4$(HP)[17]	Centro	Monoclinic	No	N/A	$P2_1/c$
$NdTaO_4$(LP) [17]	Centro	Monoclinic	No	N/A	I2/a
$CeTaO_4$[14,18]	Centro	Monoclinic	No	N/A	$P2_1/c$
$CeNbO_4$[19]	Centro	Monoclinic	No	N/A	$P2_1/c$
$LaTaO_4$[8]	Centro	Monoclinic	No	N/A	$P2_1/c$
$LaTaO_4$[8,14]	Non-centro	Orthorhombic	Possible	Unknown	$Cmc2_1$
$LaNbO_4$(LP)[10]	Centro	Monoclinic	No	N/A	I2/a
$LaNbO_4$(HP)[10]	Non-centro	Orthorhombic	Possible	Unknown	$Cmc2_1$

Centro means centro-symmetric; Non-centro means non-centrosymmetric.

Ferro: ferroelectric; Antiferro: anti-ferroelectric.

HP: The sample was made under high pressure. LP: The sample was made under normal pressure.

2.2.2. n=3 group in $A_nB_nO_{3n+2}$

The n=3 compounds can be divided into two smaller groups according to their structure. One has three perovskites layers (n=3, Type I) and the other is a combination of two (n=2) and four (n=4) layers (Type II) as shown in Fig.2.2.4.

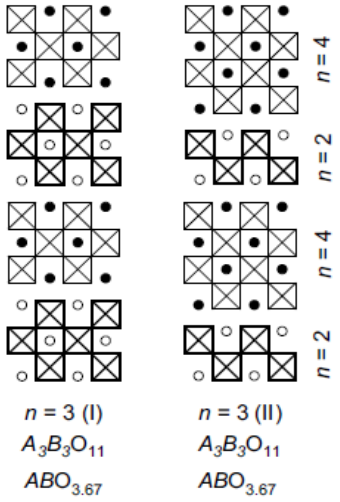

Fig.2.2.4. Structures of type I and II members of n=3 compounds.[2,3]

The type II group, $La_3Ti_2TaO_{11}$ and $Pr_3Ti_2TaO_{11}$ have been found to be noncentro-symmetric. The crystalline materials were obtained by a coprecipitation process.[20] Both $Pr_3Ti_2TaO_{11}$ and $La_3Ti_2TaO_{11}$ belong to noncentro-symmetric orthorhombic, space group $Pmc2_1$. The lattice parameters are (a, b, c, β) = (3.87Å, 20.30Å, 5.51Å, 90 °) for $Pr_3Ti_2TaO_{11}$ and (a, b, c, β) = (3.91Å, 20.20Å, 5.59Å, 90°) for $La_3Ti_2TaO_{11}$.[2,3,20]

Titov et al. estimated the spontaneous polarization (Ps) for $La_3Ti_2TaO_{11}$ and $Pr_3Ti_2TaO_{11}$ as 6 μC/cm^2 and 4 μC/cm^2 respectively.[20] However, there is no literature to support the evaluation. In contrast, compounds in the type I group, such as $Sr_2LaTa_3O_{11}$, were found

to have centro-symmetric structures.[21]

$Sm_3Ti_2TaO_{11}$ with a pyrochlore structure (a=10.29Å) can be obtained using coprecipitation process. However, the pure phase of $Nd_3Ti_2TaO_{11}$ was not obtained using coprecipitation.[20]

Table.2.2. $A_3B_3O_{11}$, n=3.

Compounds	Symmetry	Structure	Ferroelectric	Tc/℃	Space Group
$La_3Ti_2TaO_{11}$[20]	Non-centro	Orthorhombic	Possible	Unknown	$Pmc2_1$
$Pr_3Ti_2TaO_{11}$[20]	Non-centro	Orthorhombic	Possible	Unknown	$Pmc2_1$
$Sr_2LaTa_3O_{11}$[21]	Centro	Orthorhombic	No	N/A	Immm

2.2.3. n=4 group in $A_nB_nO_{3n+2}$

The n=4 group is the most researched group in the $A_nB_nO_{3n+2}$ family, due to their excellent ferroelectric properties. Some of them have been confirmed as ferroelectric materials with super high Curie points, such as $Sr_2Nb_2O_7$ (1327 ℃);[22,23] $Ca_2Nb_2O_7$ (>1525 ℃);[22,24] $La_2Ti_2O_7$ (1461 ℃)[25-27] and $Nd_2Ti_2O_7$(1482 ℃).[25,28] Their properties are discussed in detail in section.2.3.

2.2.4. n=5 group in $A_nB_nO_{3n+2}$

In the n=5 group, most of the materials investigated are centro-symmetric. $Sr_5Nb_4TiO_{17}$ was found to be anti-ferroelectric below Tc ≥ 587 ℃.[29] The crystal structure of $Sr_5Nb_4TiO_{17}$ is orthorhombic with lattice parameters (a, b, c, β) = (3.95Å, 32.52Å, 5.66Å, 90 °) with space group Pnnm and is isostructural with $Ca_5Nb_4TiO_{17}$.[2,29,30] For $Ce_5Ti_5O_{17}$ and $Pr_5Ti_5O_{17}$, just the lattice parameters are available, which are (a, b, c, β) = (7.85Å, 5.52Å, 31.24Å, 97 °) and (7.85Å, 5.52Å, 31.03Å, 96.5 °).

$Sr_5Nb_5O_{16}$ is a special compound in this group. Though it does not look like $A_nB_nO_{3n+2}$ according to its formula, it can be considered as an oxygen-deficient n=5 type compared with ordered oxygen vacancies, so the formula can be represented as $Sr_5Nb_5O_{17-\delta}$ (δ=1).[2] $Sr_5Nb_5O_{16}$ has a noncentro-symmetric structure, which indicates it could be a ferroelectric material. The lattice parameters are (a, b, c, β) = (3.99Å, 32.48Å, 5.68Å, 90 °).[31] However, its physical properties have not yet been reported. The structure is shown in Fig.2.2.5.

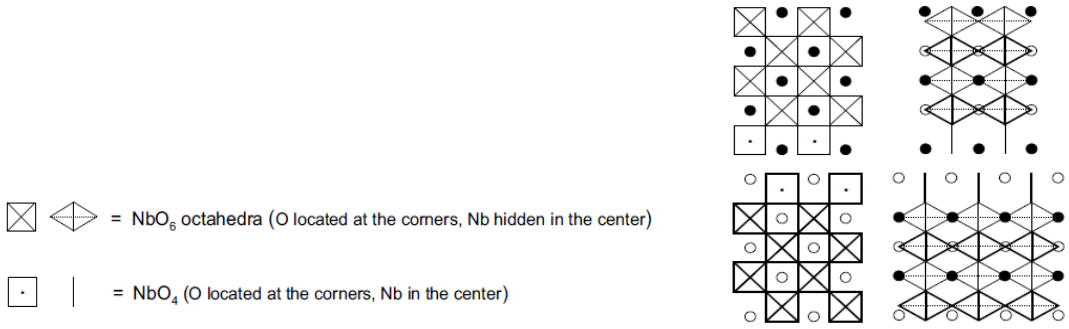

Fig.2.2.5. Skeleton drawing of $Sr_5Nb_5O_{16}$.[2]

Table.2.3. $A_5B_5O_{17}$, n=5.

Compounds	Symmetry	Structure	Ferroelectric	Tc/ ℃	Space Group
$Ca_5Nb_5O_{17}$[32]	Centro	Monoclinic	No	N/A	$P2_1/c$
$La_5Ti_5O_{17}$[2,3]	Centro	Monoclinic	No	N/A	$P2_1/c$
$Pr_5Ti_50_{17}$[2,3]	Centro	Monoclinic	No	N/A	Unknown
$Nd_5Ti_5O_{17}$[2,3]	Centro	Monoclinic	No	N/A	$P2_1/c$
$Sr_5Nb_5O_{17}$[2]	Centro	Orthorhombic	No	N/A	$P2_1/c$
$Sr_5Nb_5O_{16}$[31]	Non-centro	Orthorhombic	Possible	Unknown	$Pmn2_1$
$Sr_5Nb_4TiO_{17}$[29]	Centro	Orthorhombic	Anti-ferro	587	Pnnm
$Ce_5Ti_5O_{17}$[3]	Centro	Monoclinic	No	N/A	Unknown
$Ca_5Nb_4TiO_{17}$[2,3]	Centro	Monoclinic	No	N/A	$P2_1/c$
$Ca_4NaNb_5O_{17}$[2,3]	Centro	Monoclinic	No	N/A	$P2_1/c$
$NaCa_4Nb_5O_{17}$ [33]	Centro	Monoclinic	No	N/A	$P2_1/c$
$La_5Ti_4GaO_{17}$[2,3]	Centro	Monoclinic	No	N/A	Pmnn
$La_5Ti_4FeO_{17}$[2,3]	Centro	Monoclinic	No	N/A	Pmnn
$Pr_5Ti_4GaO_{17}$[2,3]	Centro	Monoclinic	No	N/A	$P2_1/c$
$Pr_5Ti_4FeO_{17}$[2,3]	Centro	Monoclinic	No	N/A	$P2_1/c$
$Nd_5Ti_4GaO_{17}$[2,3]	Centro	Monoclinic	No	N/A	$P2_1/c$
$Nd_5Ti_4FeO_{17}$[2,3]	Centro	Monoclinic	No	N/A	$P2_1/c$

2.2.5. n=6 and n=7 groups in $A_nB_nO_{3n+2}$

With an increasing number of perovskite layers, it becomes more difficult to form long range order in the structure, so that there are more defects and there are less compounds with an integral ratio. For the n=6 group, $Sr_6Nb_4Ti_2O_{20}$ has been confirmed as a ferroelectric material with Curie point Tc= 630 ℃.[2,34] Its lattice parameters are (a, b, c, β) = (3.94Å, 38.4Å, 5.63Å, 90 °). The dielectric constant was measured as 77 at 20 ℃, 100kHz.[35] $Nd_4Ca_2Ti_6O_{20}$ was suggested to be a ferroelectric material based on second harmonic generation. The structure parameters are (a, b, c, β) = (7.66Å, 36.64Å, 5.44Å, 90).[6,36] There are some other compounds in this group that are potentially ferroelectric due to their noncentro-symmetric structure.

The n=7 compounds are difficult to synthesize due to their instability. The structure of $Sr_7Ti_3Nb_4O_{23}$ was studied. It has centro-symmetric structure. The crystal lattice is orthorhombic with parameters (a, b, c, β) = (3.93Å, 43.61Å, 5.61Å, 90°). The relative dielectric permittivity at 20 ℃ has been reported as 61 at 100kHz. Another compound is $Ca_4Na_3Nb_7O_{23}$, which is also centro-symmetric. The structure is orthorhombic and the lattice parameters are (a, b, c, β) = (3.86Å, 5.5Å, 43.8Å, 90°).[34,35]

To sum up, it seems to be a general rule that noncentro-symmetric and ferroelectric compounds exist in the even type structures n=2, n=3(II), n=4 and n=6. The uneven type structures n=3, n=5 have centro-symmetric space groups and are anti-ferroelectrics sometimes.[2,3]

Table.2.4. $A_6B_6O_{20}$, n=6.					
Compounds	Symmetry	Structure	Ferroelectric	Tc/℃	Space Group
$Sr_6Nb_4Ti_2O_{20}$[35]	Non-centro	Orthorhombic	Yes	630	$Cmc2_1$
$Nd_4Ca_2Ti_6O_{20}$[37]	Non-centro	Orthorhombic	Possible	No report	$P2_1$
$Ca_6Nb_4Ti_2O_{20}$[2]	Non-centro	Monoclinic	Possible	No report	$P2_1$
$La_4Ca_2Ti_6O_{20}$[2]	Non-centro	Monoclinic	Possible	No report	$P2_1$

2.3. $A_2B_2O_7$ ($A_4B_4O_{14}$ n=4) compounds

In the perovskite-like layered structure (PLS) family, the n=4 group has attracted the most attention, because of their high Curie points. In this relatively big group, many compounds have excellent ferroelectric properties. This group can be divided into two main sub-series: 1) rare earth element titanates; 2) niobates and tantalates. These are summarized in table.2.5 and table.2.8, respectively.

Table.2.5. Rare earth element titanates ($A_2Ti_2O_7$).

Compounds	Symmetry	Structure	Ferroelectric	Tc/ ℃	Space Group
$La_2Ti_2O_7$[26]	Non-centro	Monoclinic	Yes	1461	$P2_1$
$Ce_2Ti_2O_7$[38]	Non-centro	Monoclinic	Yes	No report	$P2_1$
$Pr_2Ti_2O_7$[38]	Non-centro	Monoclinic	Yes	1750	$P2_1$
$Nd_2Ti_2O_7$[28]	Non-centro	Monoclinic	Yes	1482	$P2_1$
$Sm_2Ti_2O_7$(LP)[3]	Centro	Cubic	No	N/A	Fd3m
$Sm_2Ti_2O_7$(HP)[4]	Non-centro	Monoclinic	Yes	1247	$P2_1$
$Eu_2Ti_2O_7$(LP)[41]	Centro	Cubic	No	N/A	Fd3m
$Eu_2Ti_2O_7$(HP)[4]	Non-centro	Monoclinic	Yes	1077	$P2_1$

2.3.1. Lanthanum Titanate ($La_2Ti_2O_7$) and solid solution

The ferroelectric properties of $La_2Ti_2O_7$ (LTO) were first characterized in the 1970s.[26,27] At room temperature, $La_2Ti_2O_7$ has been found to possess a monoclinic structure (a, b, c, β) = (7.80Å, 13.011Å, 5.546Å, 98.6°) with space group $P2_1$.[26,27] The structure transforms into an orthorhombic structure (a, b, c, β) = (3.954Å, 25,952Å, 5.607Å, 90°) with space group $Cmc2_1$ at 780 °C. At about 1500 °C, it transforms into a paraelectric phase with space group Cmcm.[25,43] The structure of $La_2Ti_2O_7$ can also change reversibly under high pressure and the phase transition takes place at 16.7GPa at room temperature.[44] The space group of high-pressure phase was suggested to be either P2, Pm, P2/m, or $P2_1$.[44] The structural change between the orthorhombic $Cmc2_1$ and monoclinic $P2_1$ $La_2Ti_2O_7$ at 780 ℃ is shown in Fig.2.3.1 and Fig.2.3.2.[45] Displacements of the La atoms take place within the respective planes perpendicular to the a-axis, and by rotations of TiO_6 octahedra around an axis parallel to the b axis and through the respective Ti atoms.[26,27,45]

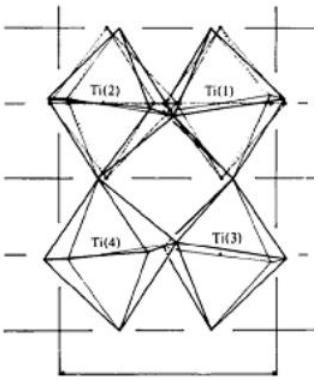

Fig.2.3.1. The linkages of TiO_6 octahedra in the phase transition at 780 ˚C ($P2_1$: solid and $Cmc2_1$: dotted).[45]

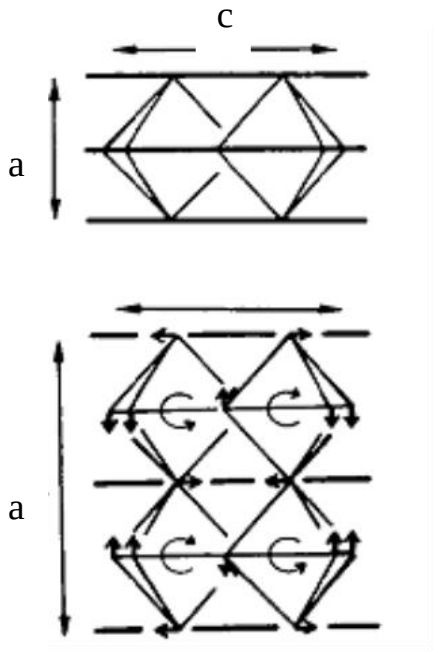

Fig.2.3.2. A schematic drawing of structural transition from the $Cmc2_1$ (upper) to the $P2_1$ (lower).[45]

$La_2Ti_2O_7$ melts at 1790 ℃ and the single crystal growth was carried out by a floating zone technique. It has density of 5.79g/cm^3 and spontaneous polarization is along the c-axis. The piezoelectric constant d_{33} was measured as 16 pC/N. The D-E hysteresis loop applying a maximum electric field of 86 kV/cm is shown in Fig.2.3.3.[43,46]

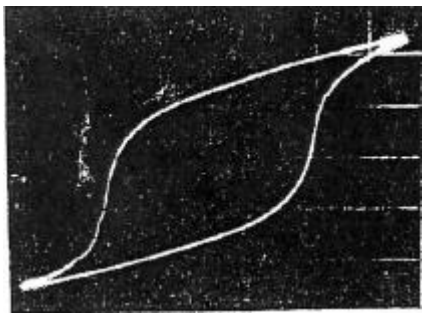

Fig.2.3.3. D-E hysteresis loop of single crystal $La_2Ti_2O_7$ at room temperature and 50Hz along c-axis. Ps=5 μC/cm2, Ec=45 kV/cm at 86 kV/cm.[26]

In 1991, $La_2Ti_2O_7$ ceramics were made using conventional solid-state reaction of mixed oxides (La_2O_3 and TiO_2); evaporative decomposition of solutions; molten salt synthesis; and hot forging. Compared to other methods, the sample made by hot forging had the highest density (99%) and highest degree of grain orientation (Lotgering factor f = 0.79). Anisotropy of dielectric constants and other electrical properties was also observed. The electric structure of $La_2Ti_2O_7$ was identified by Bruyer.[47] Band structure calculations predicted an insulating ground state for $La_2Ti_2O_7$ with a band gap energy of about 2.84 eV.[47,48]

Textured $La_2Ti_2O_7$ ceramic was fabricated by sparking plasma sintering (SPS) (The texture technique will be discussed in section 2.6). These were poled and shown to be piezoelectrically active. After texturing, generally, most of the grains are plate-like and oriented.(Fig.2.3.4) The direction along which the grains are orientated is perpendicular to the SPS pressing direction. The degree of grain orientation is high (Lotgering factor f = 0.82). The piezoelectric constant was measured as 2.6 pC/N.[25]

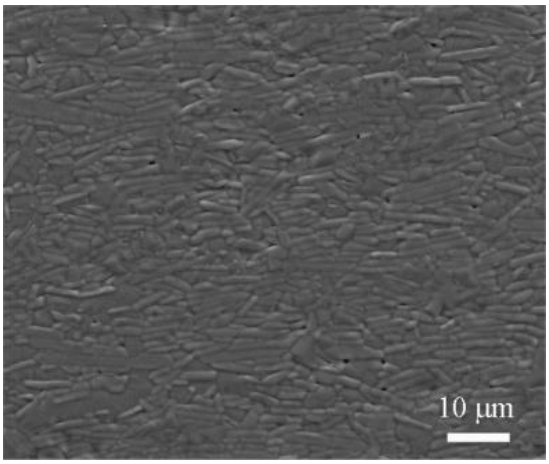

Fig.2.3.4. Scanning electron microscope micrograph of the textured $La_2Ti_2O_7$.[25]

The Curie point could be observed through the temperature dependence of the dielectric constant and loss tangent, which is 1461℃ (Fig.2.3.5). The permittivity of $La_2Ti_2O_7$ ceramic was measured to be from 45 to 50.[25] The resistivity of the ceramics are shown in Fig.2.3.8.

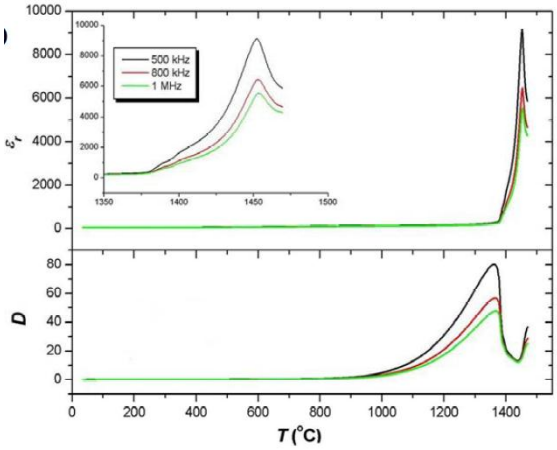

Fig.2.3.5. Temperature dependence of the dielectric constant (ε) and loss (D) of $La_2Ti_2O_7$ under 1MHz, 800kHz and 500kHz.[25]

Because $La_2Ti_2O_7$ has very high Curie point and high coercive field for a ceramic, some studies have been done on $La_2Ti_2O_7$ based solid solution to improve properties.

$(La_{1-x}Nd_x)_2Ti_2O_7$ compounds have been investigated by Shao et al.[49] A series of compounds with the general formula $(La_{1-x}Nd_x)_2Ti_2O_7$ ($0.0<x<1.0$) was prepared by the sol–gel method. The XRD patterns of the series compounds are shown in Fig.2.3.6.[49] They all have a monoclinic structure with $P2_1$ space group. With the increase of x, an anisotropic evolution of the lattice parameters can be observed in the insert of Fig.2.3.6. The c-axis is constant with increasing x while a- and b-axes decrease.[49]

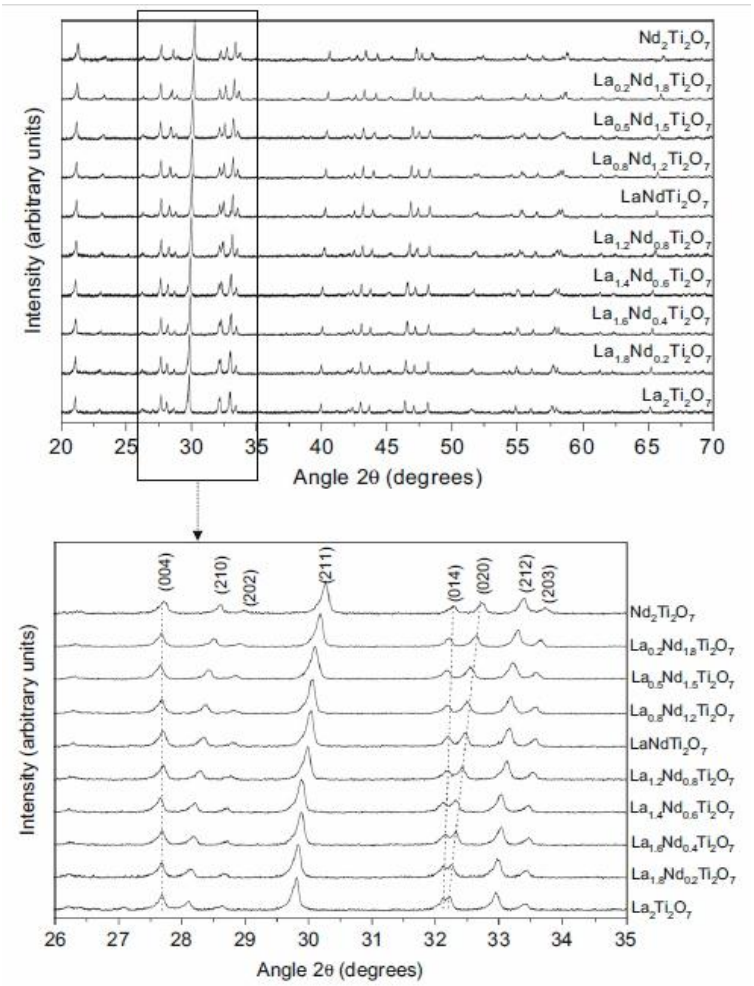

Fig.2.3.6. XRD patterns of $(La_{1-x}Nd_x)_2Ti_2O_7$ powders.[49]

The dielectric properties of $(La_{1-x}Nd_x)_2Ti_2O_7$ have been studied.[49] At low frequency, the dielectric constant increases with increasing x at first up to a maximum value when x=0.5, then it decreases.

Recently, the solid solution system with the general formula $(La_{1-x}Sm_x)_2Ti_2O_7$ ($0<x<1$) has been synthesized and characterized. These compounds are isostructural with perovskite-type $La_2Ti_2O_7$ until x = 0.8. Above this value (x>0.8), a mixture was obtained between the substituted perovskite layered phase and the pyrochlore $Sm_2Ti_2O_7$ phase.[39] Electronic structure calculations of $(La_{0.9}Sm_{0.1})_2Ti_2O_7$ show that this compound

is an insulator with a band gap of about 2.77eV. [39]

Some other solid solution compounds of $La_2Ti_2O_7$ have been reported, but the structure symmetry and ferroelectric properties have not been investigated. $La_{1.5}Ln_{0.5}Ti_2O_7$ (Ln= Pr, Gd, Er) were prepared using a polymeric complex method. The cell volume decreases from $La_2Ti_2O_7$ to $La_{1.5}Er_{0.5}Ti_2O_7$. The details of the lattice parameters are shown in Table.2.6. [50,51]

Table.2.6. Lattice constant of $La_{1.5}Ln_{0.5}Ti_2O_7$ (Ln= Pr, Gd, Er).[50]

Lattice parameter	$La_2Ti_2O_7$	$La_{1.5}Pr_{0.5}Ti_2O_7$	$La_{1.5}Gd_{0.5}Ti_2O_7$	$La_{1.5}Er_{0.5}Ti_2O_7$
a (Å)	13.011	13.006	12.945	12.928
b (Å)	5.546	5.535	5.495	5.489
c (Å)	7.812	7.784	7.744	7.718
V($Å^3$)	557.31	554.00	544.60	541.47

2.3.2. Neodymium Titanate ($Nd_2Ti_2O_7$) and solid solution

Single crystals of $Nd_2Ti_2O_7$ (NTO) were synthesized by a floating zone technique. $Nd_2Ti_2O_7$ has a similar structure to $La_2Ti_2O_7$. It is a monoclinic structure with space group $P2_1$. The lattice parameters are (a, b, c, β) = (7.68Å, 13.02Å, 5.48Å, 98.47°) at room temperature. The ferroelectric phase changes into paraelectric phase at 1481℃. The spontaneous polarization is along the c-axis.[25,28,52]

The melting point of $Nd_2Ti_2O_7$ is 1800℃ and the theoretical density is 6.08 g/cm^3. For the single crystal, the coercive field (Ec) is 200 kV/cm and d_{33} is 6.5 pC/N.[28] The band gap of $Nd_2Ti_2O_7$ was predicted to have an energy of 1.63-3.65 eV.[48,51]

$Nd_2Ti_2O_7$ ceramics can be prepared by solid state calcination of the mixed oxide (Nd_2O_3 and TiO_2) and sintering in air from 1300 ^{o}C to 1500 ^{o}C.[53] The highest density achieved was 95% at about 1375 ^{o}C.

Textured ceramics of $Nd_2Ti_2O_7$ were prepared by two-step sintering and hot forging in graphite dies in a SPS furnace. $Nd_2Ti_2O_7$ ceramic was dark-blue in colour.[25]

The dielectric constant was measured to be around 36 for the $Nd_2Ti_2O_7$ ceramic. The Curie point can be confirmed using the dielectric anomalies in the temperature dependence of dielectric constant and loss (Fig.2.3.7).

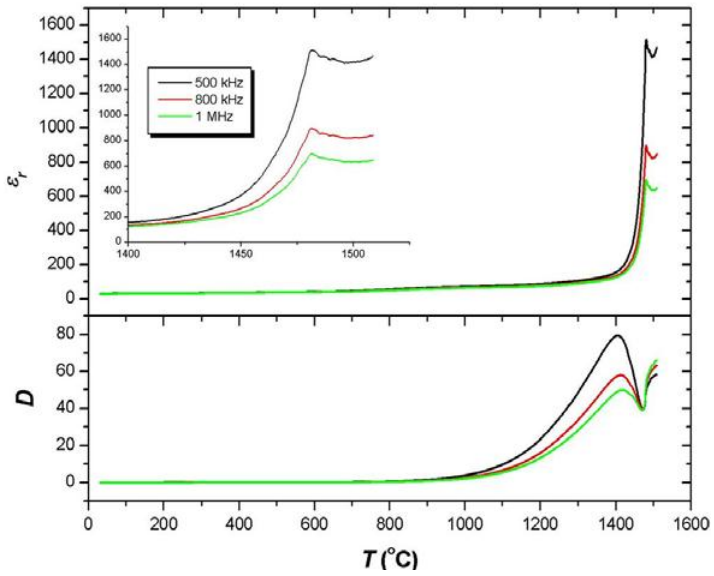

Fig.2.3.7. Temperature dependence of dielectric constant and loss of $Nd_2Ti_2O_7$ ceramic sintered at 1550 ℃.[25]

The electrical resistivities of $La_2Ti_2O_7$ and $Nd_2Ti_2O_7$ have been reported. Both of them are excellent dielectric materials. Even at high temperature up to 500 ℃, their resistivity is still about 10^8 to 10^9 Ω.cm (Fig.2.3.8).

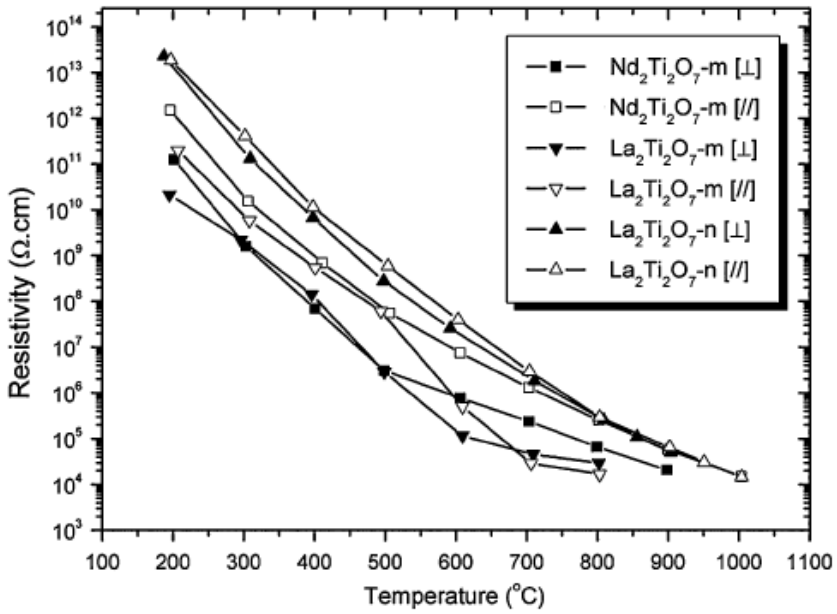

Fig.2.3.8. DC resistivity of textured ceramics as a function of temperature.[25]

$Nd_{2-x}Li_xTi_2O_{7-\delta}$ (x=0, 0.1, 0.15) solid solution has been obtained using a gel entrapment technique by Pai et al.[54] The structure details are shown in Table. 2.7. With Li doping, the conductivity increases.

Table.2.7. Cell parameters of $Nd_{2-x}Li_xTi_2O_{7-\delta}$.[54]

Sample	a(Å)	b(Å)	c(Å)	β(°)	V(Å^3)
$Nd_2Ti_2O_7$	5.4677	13.027	7.6784	98.58	540.79
$Nd_{1.9}Li_{0.1}Ti_2O_7$	5.4636	13.036	7.6802	98.69	540.50
$Nd_{1.85}Li_{0.15}Ti_2O_7$	5.4662	13.012	7.6843	98.61	540.37

The $Nd_2(Zr_{1-x}Ti_x)_2O_7$ (x=0.2, 0.4, 0.6, 0.8) series compounds were investigated by Harvey.[55] With increasing $Nd_2Zr_2O_7$ content, the structure transforms from monoclinic PLS ($P2_1$) to cubic pyrochlore with space group Fd3m.[55] The unit cell volumes decreases with increasing $Nd_2Ti_2O_7$ content (Fig.2.3.9).[55]

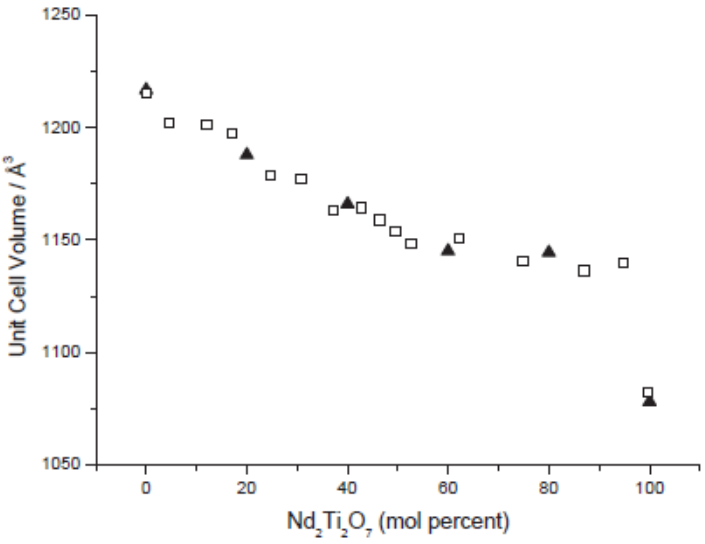

Fig.2.3.9. Unit cell volumes for series $Nd_2(Zr_{1-x}Ti_x)_2O_7$.[55]

Some other compounds were synthesized, such as $NdSmTi_2O_7$, $NdEuTi_2O_7$ and $NdPrTi_2O_7$, but no literature is available about their ferroelectric properties.[5]

The $Gd_{2-x}Nd_xTi_2O_7$ compounds were synthesized and prepared by ceramic sintering. Using XRD, an increase in lattice parameter was observed as a function of x in the series $Gd_{2-x}Nd_xTi_2O_7$ in the composition range $0.0<x<0.8$. Compositions $Gd_{2-x}Nd_xTi_2O_7$ in the range $0.8<x<1.4$ were biphasic. Above x=1.6, the solid solutions are monoclinic, isostructural with $Nd_2Ti_2O_7$.[56] The XRD patterns are shown in Fig.2.3.10.

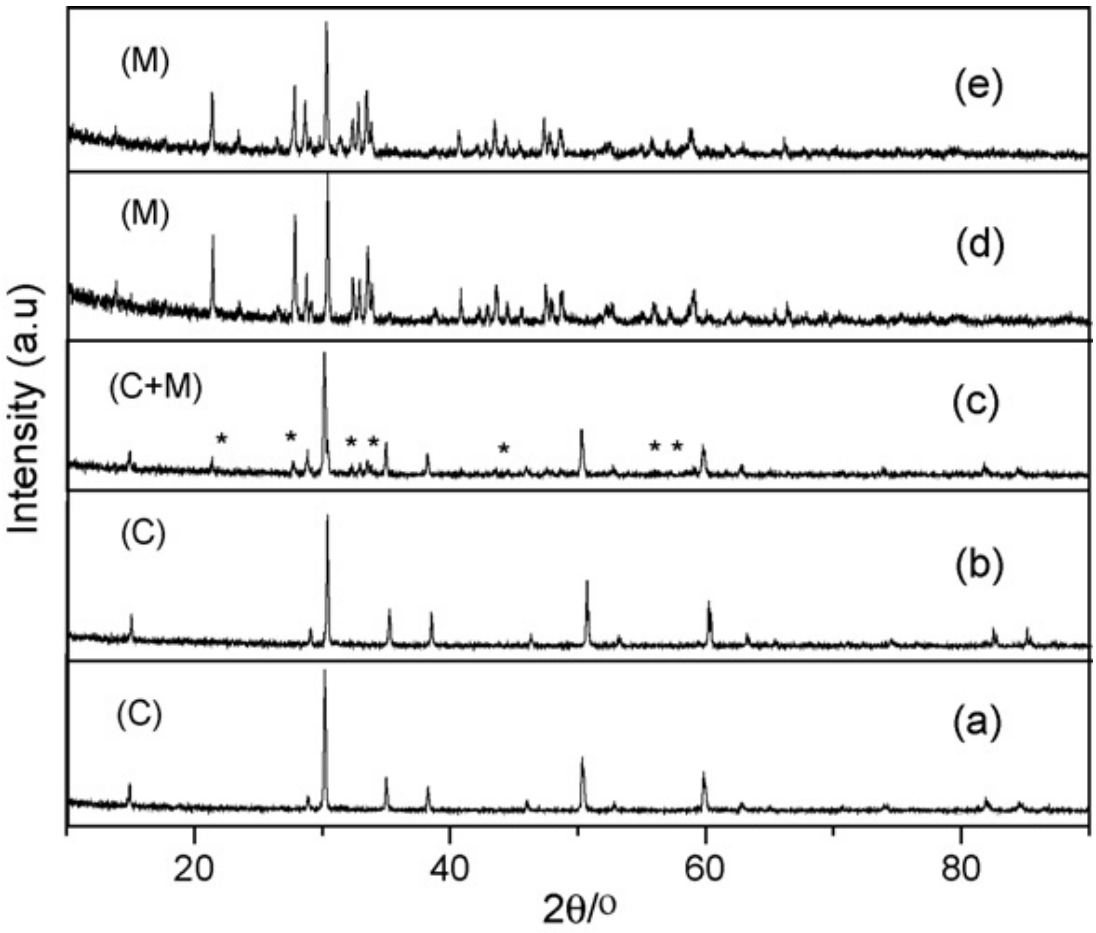

Fig.2.3.10. XRD patterns of (a) $Gd_2Ti_2O_7$, (b) $Gd_{1.8}Nd_{0.2}Ti_2O_7$, (c) $GdNdTi_2O_7$, (d) $Nd_2Ti_2O_7$. C=cubic pyrochlore; M=monoclinic. (*) indicate the presence of peaks for monoclinic phase along with cubic pyrochlore phase.[56]

2.3.3. Cerium Titanate ($Ce_2Ti_2O_7$)

It is difficult to prepare cerium titanate ($Ce_2Ti_2O_7$) at high temperature, because Ce (III) compounds tend to form the thermodynamically stable Ce(IV) when the temperature is above 400 ^oC.[3,57,58] The thermogravimetric analysis of several Ce compounds is shown in Fig.2.3.11. For all of the compounds, there is an increase of oxygen content between 200 and 400 ^oC, which indicates the Ce^{3+} is not stable in air.

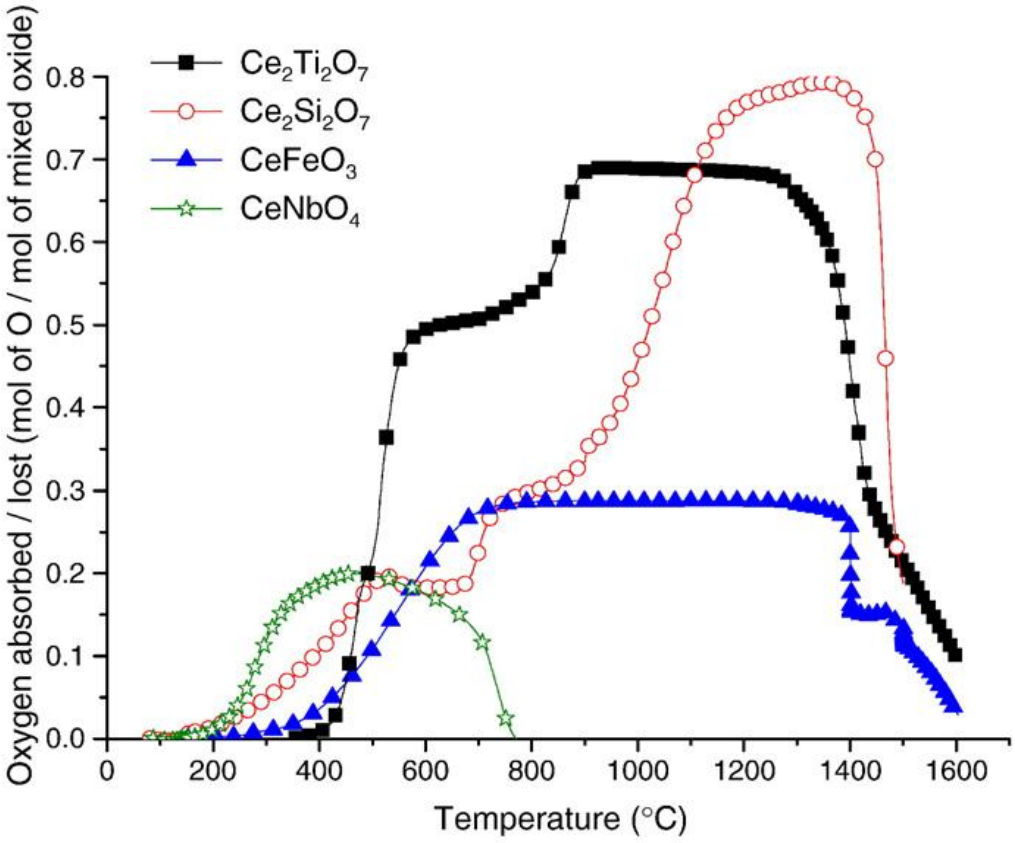

Fig. 2.3.11. Thermo gravimetric analysis of $Ce_2Ti_2O_7$, $Ce_2Si_2O_7$, $CeFeO_3$ and $CeNbO_4$ under air at atmospheric pressure.[57]

To prepare $Ce_2Ti_2O_7$ (CTO) compounds, it is preferable to use CeO_2 and Ti_2O_3 as the starting materials. The mixture is placed in an argon atmosphere at 1200 ^oC to get

$Ce_2Ti_2O_7$ powder. Alternatively, the floating zone melting method was used with starting materials of TiO_2 and CeO_2 for synthesis of single crystals. An atmosphere of 98% argon and 2% hydrogen was used. Its structure is monoclinic with space group $P2_1$. The lattice constant is (a, b, c, β) = (7.74Å, 12.99Å, 5.5Å, 98.6°). The melting point is 1790 ℃.[3,59,60]

In 1985, the assumption of a linear dependence of Tc on the ionic radius of the rare-earth element in compounds $Ln_2Ti_2O_7$ with PLS structure was made to speculate the Tc of CTO and NTO.[60] But, for the NTO Tc is not 1885 ℃ as assumed, which was confirmed as 1481 ℃.[25] Also, there is no experiment confirming the Tc of CTO. Lichtenberg has reported that the crystal is ferroelectric based on the structure, but there are no details about its ferroelectric properties.[2,3,60]

$Ce_2Ti_2O_7$ films were made by a spin-coating method on Pt/Ti/SiO_2/Si and Y_2O_3/Si substrates. Subsequently, the films were annealed under low-vacuum (6.664 Pa) at 800 ℃ for 30 min in a tube furnace.[61] It was found that CTO and LTO had similar crystal structures at room temperature. Fig.2.3.12 shows the frequency dependence of dielectric constant and loss of the CTO, while the P-E loop is shown in Fig.2.3.13. The domain switch cannot be observed and the round shape indicates that $Ce_2Ti_2O_7$ film has a relatively high conductivity. There is no literature reported on solid solutions based on $Ce_2Ti_2O_7$ due probably to its instability in air at high temperature.

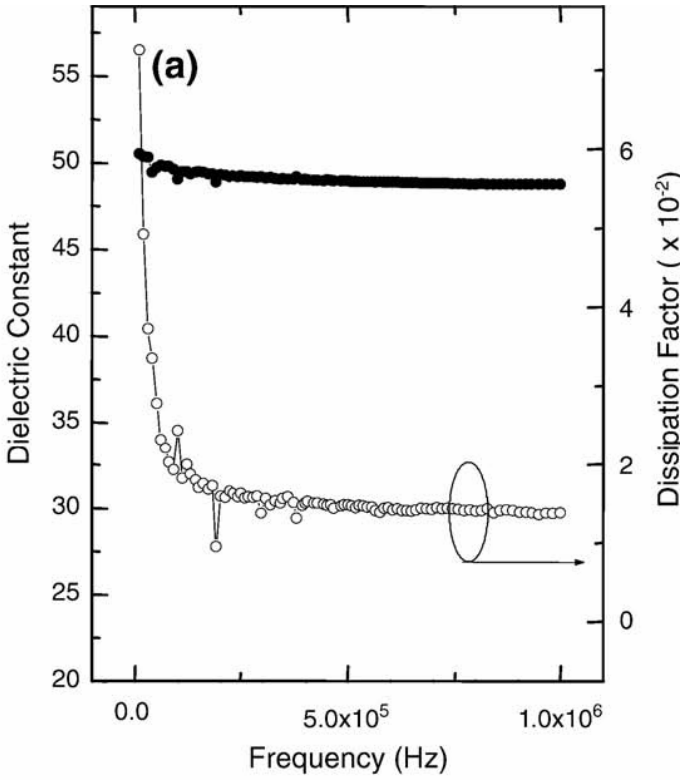

Fig.2.3.12. Dielectric constant and loss of $Ce_2Ti_2O_7$ film.[61]

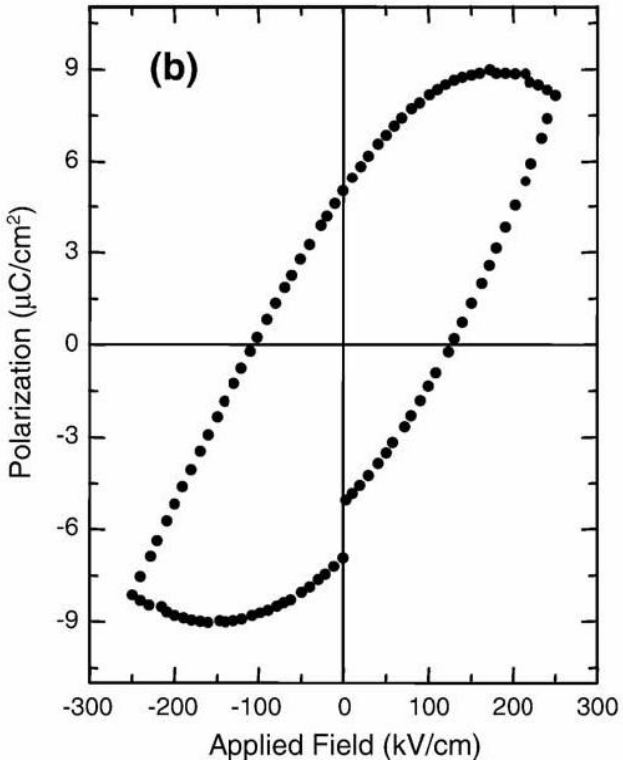

Fig.2.3.13. P-E hysteresis loop of the Pt/$Ce_2Ti_2O_7$/Pt structure.[61]

2.3.4. Praseodymium titanate ($Pr_2Ti_2O_7$)

A Single crystal of Praseodymium titanate ($Pr_2Ti_2O_7$, PTO) was prepared by floating zone melting in a nitrogen atmosphere from a stoichiomeric mixture of Pr_6O_{11} and TiO_2. The crystal is transparent and grass green in color. $Pr_2Ti_2O_7$ can also be made by solid phase synthesis. A powder mixture of Pr_6O_{11} and TiO_2 was calcinated at 850 ℃ for 10 hours followed by 1150^{o}C for 10 hours under static air conditions.[2,51,62]

The structure was confirmed as monoclinic with space group $P2_1$. The lattice constant is (a, b, c, β) = (7.704Å, 12.996Å, 5.485Å, 98.51°). The spontaneous polarization is along c-axis. The XRD data showed $Pr_2Ti_2O_7$ is isostructural with $La_2Ti_2O_7$. The distortion of the TiO_6 octahedra is accompanied by changes in Ti-O bond length (1.78-2.25Å) and O-Ti-O bond angles (80.3 °-103.4 ° and 163.3 °-172.8 °).[2,3,62,63]

The $Pr_2Ti_2O_7$ ceramic was made by self-propagated high temperature synthesis (SHS).[64] The density was measured to be 5.95g/cm^3. The thermal properties were characterized by thermo gravimetric analysis (TG), differential thermogravimetric analysis (DTG) and differential thermal analysis (DTA).[64] The SHS sample lost weight at about 430 ℃ in nitrogen.[64] Its dielectric constant at room temperature was found to be about 40.[65]

The ferroelectric properties of PTO were first reported in 1980 for the first time.[63] A phase transition corresponding to the Curie point occurs at 1750 ℃ below its melting point at 1790 ℃. The electronic band gap was reported by Dong et al to be 2.99eV.[51]

2.3.5. Europium titanate ($Eu_2Ti_2O_7$) and Samarium titanate ($Sm_2Ti_2O_7$)

$Eu_2Ti_2O_7$ (ETO) prepared at atmospheric pressure has the pyrochlore structure (cubic), and has PLS structure if prepared at high pressure. The pyrochlore structure is centro-symmetric and has space group Fd3m with a=10.192Å.[40,42] $Eu_2Ti_2O_7$ with PLS structure was fabricated by a two-stage method. At room temperature (25 ℃), a pressure of 3~4 GPa was applied, then powder was sintered up to 1750 ℃ under a pressure 8 GPa.[40,42]

Other literature reported $Eu_2Ti_2O_7$ with PLS structure could be synthesized under ambient-pressure at 800 ℃ for 15h by using $EuTiO_3$ as the precursor by a one step method (Fig.2.3.14).[66] The PLS phase of $Eu_2Ti_2O_7$ has monoclinic structure with space group of $P2_1$, which is isostructural with $La_2Ti_2O_7$ and the unit-cell parameters are (a, b, c, β) = (7.54Å, 12.86Å, 5.39Å, 98.3°).[2,3,66] The ferroelectric properties of $Eu_2Ti_2O_7$ have been studied by second harmonic generation. The curie point was estimated as ~1520 ℃ and spontaneous polarization as 2.7 uC/cm^2.[2,3,60] The electrical conductivity of single crystal $Eu_2Ti_2O_7$ has been investigated. Below 700K, The conductivity is due to extrinsic conduction suggested by the low activation energy and intrinsic charge carriers become dominant above 700K as most of the impurity charge carriers are exhausted up to the temperature supported by the high activation energy. The band gap for cubic $Eu_2Ti_2O_7$ was measured as 2.5eV.[40,42,66-68]

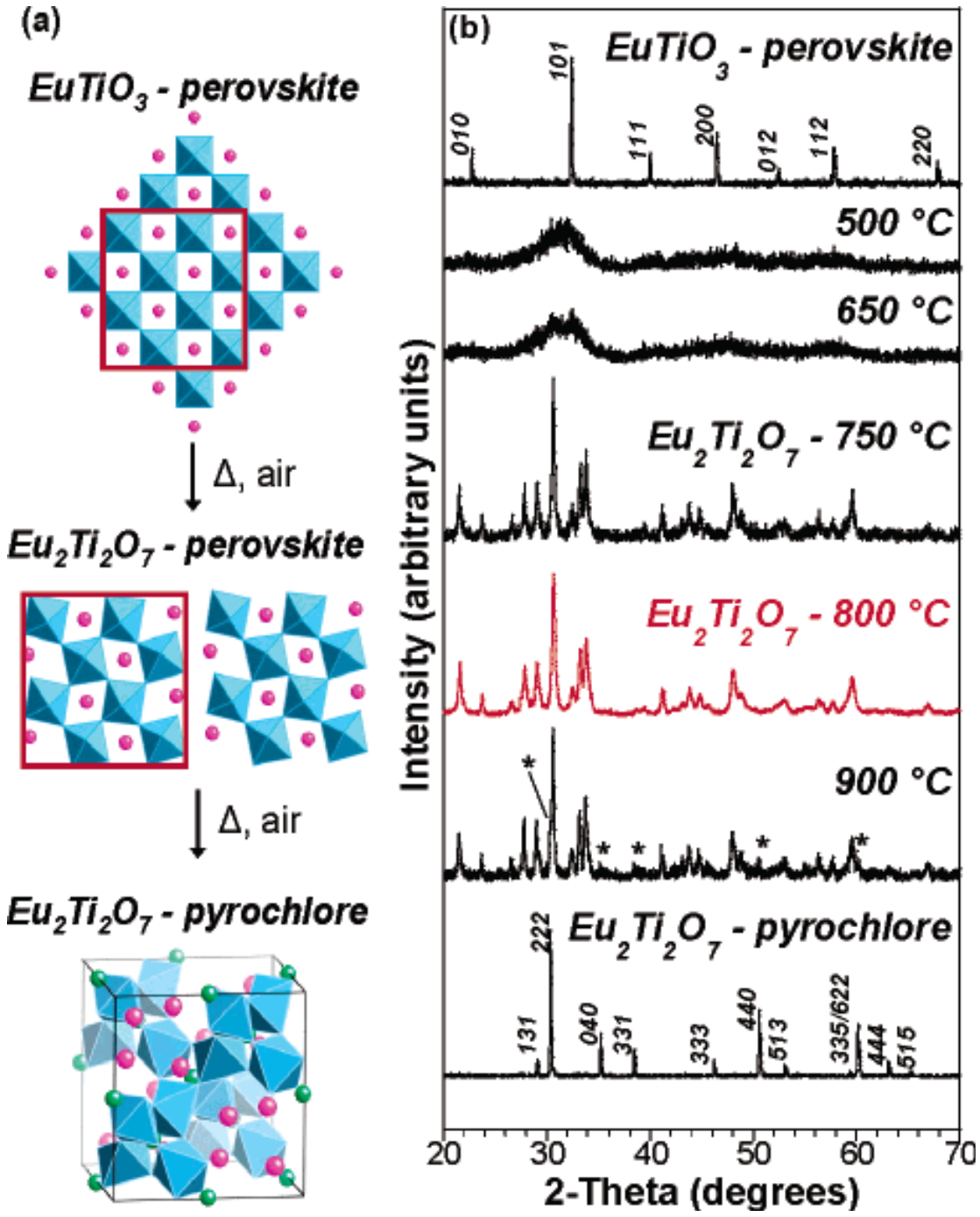

Fig.2.3.14. (a) The ambient-pressure synthetic pathway. The light blue polyhedron: TiO_6 octahedra; the pink spheres: Eu cations. In the pyrochlore structure, green pheres: oxygen atoms which are not part of the TiO_6 octahedra. (b) Powder XRD data for the $EuTiO_3$ precursor. The amorphous PLS intermediate were generated at 500 and 650 ℃, and the crystallization of PLS $Eu_2Ti_2O_7$ was observed at 750, and 800 ℃. At 900 ℃, the $Eu_2Ti_2O_7$ pyrochlore phase was come out (*) and it forms at higher temperatures.[66]

$Sm_2Ti_2O_7$ (STO) is similar to $Eu_2Ti_2O_7$, it also has the pyrochlore structure (cubic) at atmosphere pressure and converts into the PLS structure under high pressure (5.4GPa).[67] The pyrochlore $Sm_2Ti_2O_7$ compound was synthesized by solid-state reaction methods. Sm_2O_3 and TiO_2 (anatase) were well mixed with nominal composition of $Sm_2Ti_2O_7$ and pressed into pellets. The mixture was heated up to 1100 ℃ for 48h. The pyrochlore phase has cubic structure with Fd3m space group and a=10.211Å. The PLS phase has monoclinic structure with $P2_1$ space group. The lattice parameters for PLS structure are (a, b, c, β) = (7.62Å, 5.43Å, 12.90Å, 98.4°). The pyrocholre phase is not ferroelectric. In contrast, the PLS structure like that of $Eu_2Ti_2O_7$ is ferroelectric and the ferroelectric properties were estimated by second harmonic generation. The Tc was reported as 1077 ℃. The spontaneous polarization is 2.1 uC/cm^2.[69-71]

Overall, in rare earth element titanates of general formula $A_2Ti_2O_7$, the PLS structure material tends to be more stable with larger A-site cations.[59] Lanthanide titanates $Ln_2Ti_2O_7$ (Ln=La, Ce, Pr, Nd) with radius ratios of the cations $rLn^{3+}/rTi^{4+} \geq 1.5$ prefer the PLS structure and prefer to have $P2_1$ space group at room temperature. On the other hand, $Ln_2Ti_2O_7$ (Ln=Gd-Lu) with radius ratios $1.22 \leq rLn^{3+}/rTi^{4+} \leq 1.5$ crystallize as the cubic pyrochlore structure. $Sm_2Ti_2O_7$ and $Eu_2Ti_2O_7$, which are in the middle of the series, crystallize with the PLS structure under high pressure conditions and pyrochlore structure under atmospheric pressure.[72]

2.3.6. Strontium Niobate ($Sr_2Nb_2O_7$) and solid solution

Single-crystal $Sr_2Nb_2O_7$ (SNO) has been investigated by Nanamatsu et al.[23] It was produced by the floating zone melting method. $SrCO_3$ and Nb_2O_5 were used as raw materials. $Sr_2Nb_2O_7$ crystal is colourless and transparent with density 5.17g/cm^3. The crystal is orthorhombic with space group of $Cmc2_1$.[23] The lattice parameters are (a, b, c, β) = (3.95Å, 26.77Å, 5.69Å, 90°).[23,73,74] The Ps direction is along c-axis. The structure is shown in Fig.2.3.15.

Table.2.8. Niobates ($A_2Nb_2O_7$) and Tantalates ($A_2Ta_2O_7$).

Compounds	Symmetry	Structure	Ferroelectric	Tc/℃	Space Group
$Ca_2Nb_2O_7$[22]	Non-centro	Monoclinic	Yes	>1525	$P2_1$
$Sr_2Nb_2O_7$[22]	Non-centro	Orthorhombic	Yes	1327	$Cmc2_1$
$Ca_2Ta_2O_7$[75]	Poly type	Poly type	Unknown	Unknown	Poly type
$Sr_2Ta_2O_7$[76]	Non-centro	Monoclinic	Yes	-107	$P2_1$
$Ba_2Ta_2O_7$	No report	No report	No report	N/A	No report

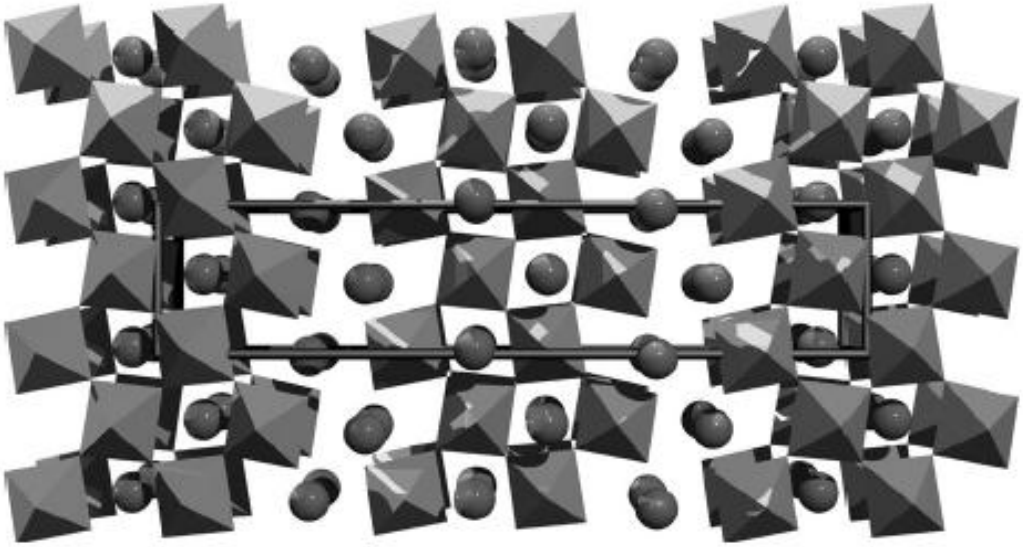

Fig.2.3.15. View along a of the basic crystal structure of $Sr_2Nb_2O_7$. NbO_6 octahedra are shown as light gray shaded octagons. Spheres represent the Sr atoms.[77]

$Sr_2Nb_2O_7$ is ferroelectric and has three phase transitions. Below -156 ℃ it is ferroelectric with Ps in the bc-plane. The Ps rotate at 215 ℃ into the c-axis and it becomes a paraelectric phase at 1342 ℃.[23] The ferroelectric properties of single crystal $Sr_2Nb_2O_7$ have been demonstrated by the dielectric constant anomaly and the P-E hysteresis loop shown in Fig.2.3.16 and Fig.2.3.17 respectively. The Pr = 7uC/cm^2, Ec = 6kV/cm at maximum applied field E_0=25 kV/cm.[23,78]

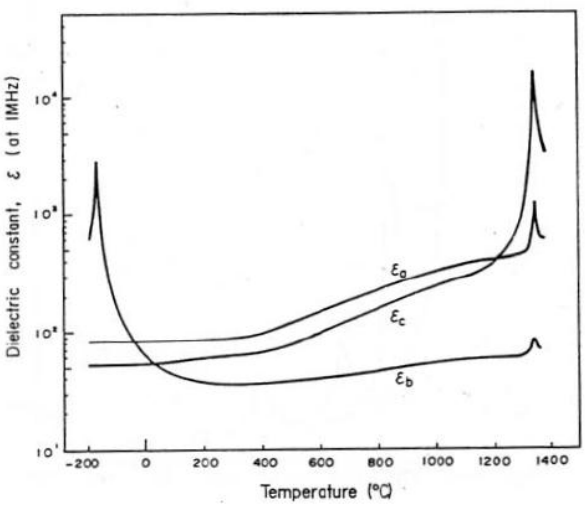

Fig.2.3.16. Temperature dependence of dielectric constants of $Sr_2Nb_2O_7$ crystal at 1MHz.[79]

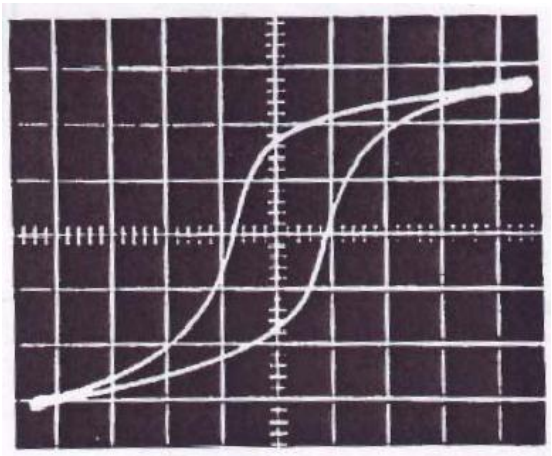

Fig.2.3.17. D-E hysteresis loop of $Sr_2Nb_2O_7$ b-plate crystal at room temperature and 50Hz.[23]

The ferroelectric properties of $Sr_2Nb_2O_7$ textured ceramics have been investigated by Ning et al.[22] The ceramics was textured by SPS using a two-step method (Section.2.4). The Curie point was reported to be ~1327 ℃ and d_{33} was measured as 2.8pC/N.[22] The grains were plate like and oriented (Fig.2.3.18). The temperature dependence of the dielectric constants and P-E, I-E loops are shown in Fig.2.3.19 and Fig.2.3.20.

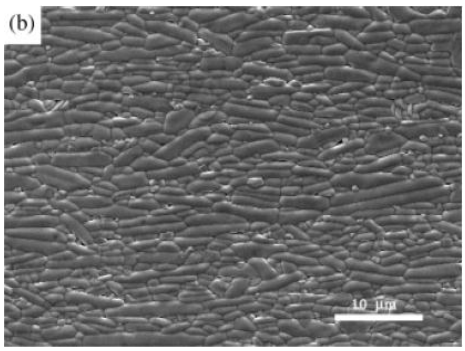

Fig.2.3.18. Scanning electron microscopic micrographs of $Sr_2Nb_2O_7$ ceramic surfaces perpendicular to the SPS pressing direction.[22]

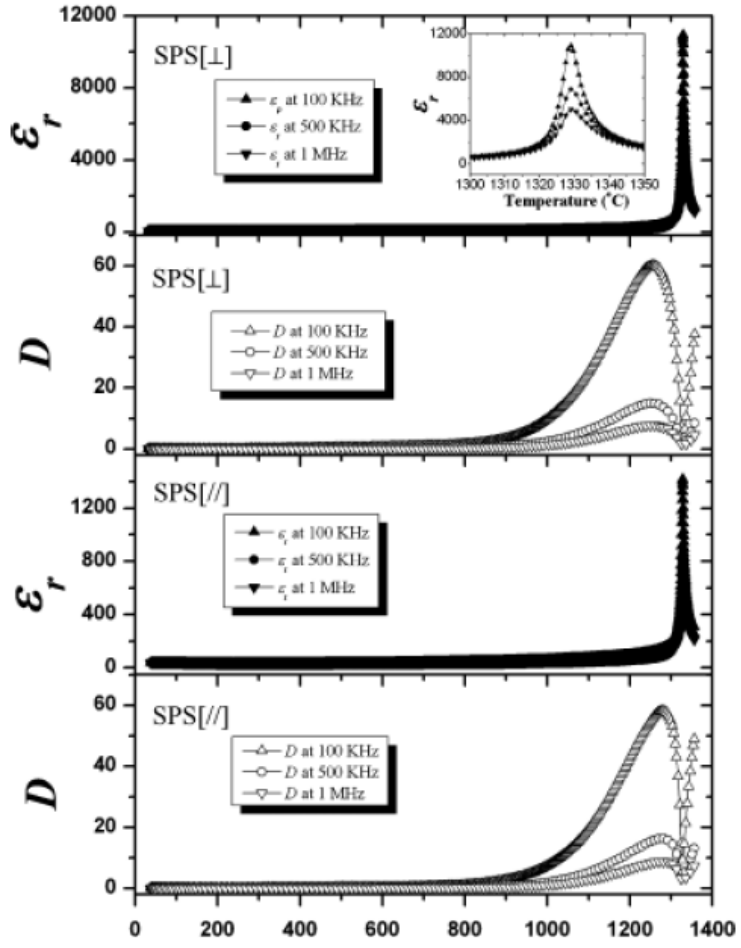

Fig.2.3.19. Temperature dependence of the dielectric constant and loss of textured $Sr_2Nb_2O_7$ ceramics perpendicular and parallel to the spark plasma sintering (SPS) pressing direction.[22]

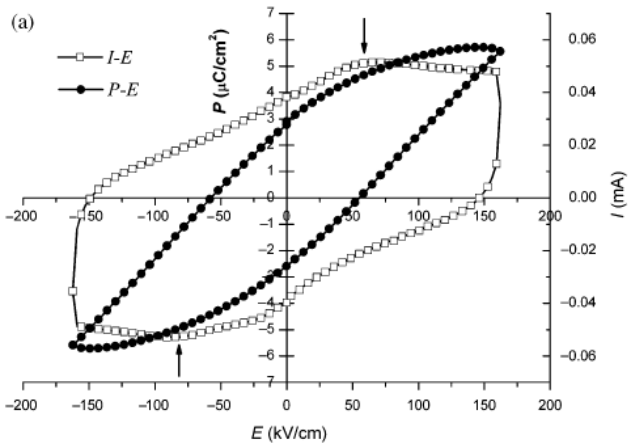

Fig.2.3.20. I-E and P-E hysteresis loops of textured $Sr_2Nb_2O_7$ ceramic along the direction perpendicular to the pressing direction at 200 ℃.[22]

$Sr_2Nb_2O_7$ is the most studied compounds in the n=4 family, and there are many reports on solid solution systems. The $(Sr_{1-x}M_x)_2Nb_2O_7$ (M=Ba, Ca, Zn, Cd, Pb) systems have been investigated.[80] When M=Ba, Ca, Zn, Cd, Pb, the solid solution limits were reported at x= 0.3, 1, 0.25, 0.3, and 0.4 respectively.[80] The system of $(Sr_{1-x}Pb_x)_2Nb_2O_7$ is shown in Fig.2.3.21.

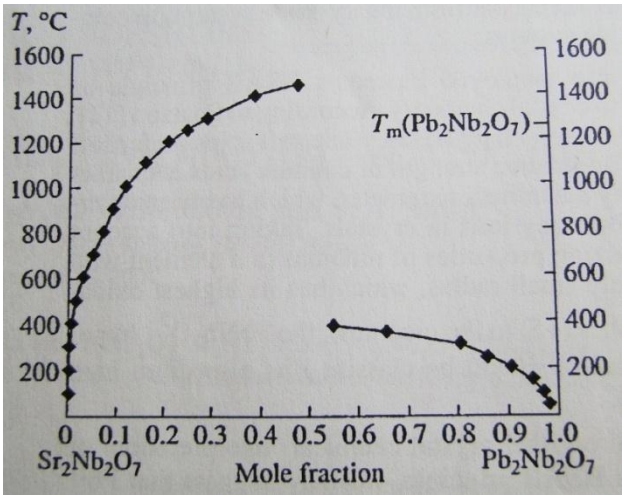

Fig.2.3.21. The demixing curve for $Sr_2Nb_2O_7$-$Pb_2Nb_2O_7$ system. The curve presents the isomorphous miscibility boundaries as functions of temperature.[81]

For $(Sr_{1-x}Ca_x)_2Nb_2O_7$,and $Sr_2(Ta_{1-x}Nb_x)_2O_7$ (Fig.2.3.22) the Curie point increases with increasing x. This reflects the fact that Tc decreases in the order Tc ($Ca_2Nb_2O_7$) > Tc ($Sr_2Nb_2O_7$) > Tc ($Sr_2Ta_2O_7$). But for $(Sr_{1-x}Ba_x)_2Nb_2O_7$ and $(Sr_{1-x}Pb_x)_2Nb_2O_7$, the Curie point both decrease with increasing x.[79] The curie points of some $Sr_2Nb_2O_7$ based solid solutions are shown in table.2.10. [79]

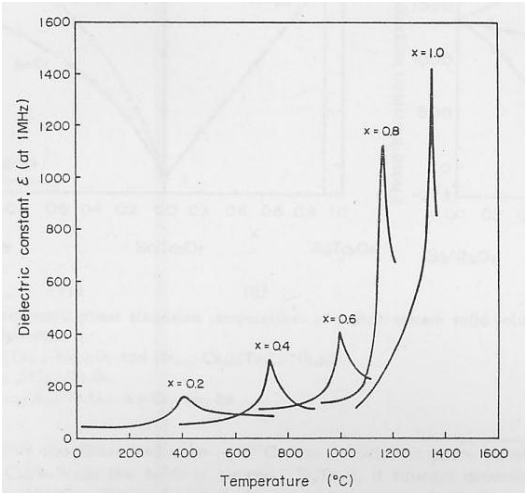

Fig.2.3.22. Dielectric constants of solid solution ceramics $Sr_2(Ta_{1-x}Nb_x)_2O_7$.[79]

Table.2.10. Ferroelectric phase transition temperature (℃) of $A_2B_2O_7$-system solid solution involving $Sr_2Ta_2O_7$ and $Sr_2Nb_2O_7$ as an end compound.[79]

Solid solutions	x						
	0	0.1	0.2	0.4	0.6	0.8	1.0
$Sr_2(Ta_{1-x}Nb_x)_2O_7$	-107		410	735	1000	1160	1342
$Sr_{2-2x}Ca_{2x}Ta_{2-2x}Nb_{2x}O_7$	-107	305	600	1160	1450		>1500
$(Sr_{1-x}Ca_x)_2Ta_2O_7$	-107		320	710	1127	>1400	
$(Sr_{1-x}Ca_x)_2Nb_2O_7$	1342		>1400				>1500
$(Sr_{1-x}Pb_x)_2Nb_2O_7$	1342		1280	1225			
$(Sr_{1-x}Ba_x)_2Nb_2O_7$	1342		1080	825	100		

In the $(Sr_{1-x}M_x)_2Nb_2O_7$ (M=Cu, Ni) series, solid solution ranges were determined to be $0<x<0.2$ and $0<x<0.1$ for Cu and Ni, respectively based on the XRD results. The resistivity was reduced by the substitution of Cu and Ni, due to the increase in electronic conductivity with increasing transition-metal content.[82]

For the $Sr_{2-x}Eu_xNb_2O_7$ system, after heating at 1200^{o}C for 20h if $x<1$ only the orthorhombic phase is produced, if $x>1$ orthorhombic and hexagonal phases coexist.[83]

The $(Ca_2Nb_2O_7)_{0.5}(La_2Ti_2O_7)_{0.5}$, ($CaLaTiNbO_7$), compound has a melting point of 1630^{o}C and a phase transition temperature point of 1430^{o}C. The $(Sr_2Nb_2O_7)_{0.5}(La_2Ti_2O_7)_{0.5}$, ($SrLaTiNbO_7$), has a phase transition temperature of 1050^{o}C.[60]

2.3.7. Strontium Tantalate ($Sr_2Ta_2O_7$) and solid solution

Single crystals of $Sr_2Ta_2O_7$ were grown by the floating zone technique using $SrCO_3$ and Ta_2O_5 as the raw materials.[84] The single crystals were transparent and colourless with measured density of 7.05 g/cm^3.[84] Compared to $Sr_2Nb_2O_7$, $Sr_2Ta_2O_7$ has a very low ferroelectric phase transition temperature (-107^{o}C). Hence it is a paraelectric phase at room temperature shown (Fig.2.3.23). It has an orthorhombic structure with space group Cmcm at room temperature and undergoes a transition to ferroelectric phase at about -107^{o}C to orthorhombic symmetry with space group $Cmc2_1$. The lattice parameters are (a, b, c, β) = (3.94Å, 27.2Å, 5.69Å, 90°).[84-86]

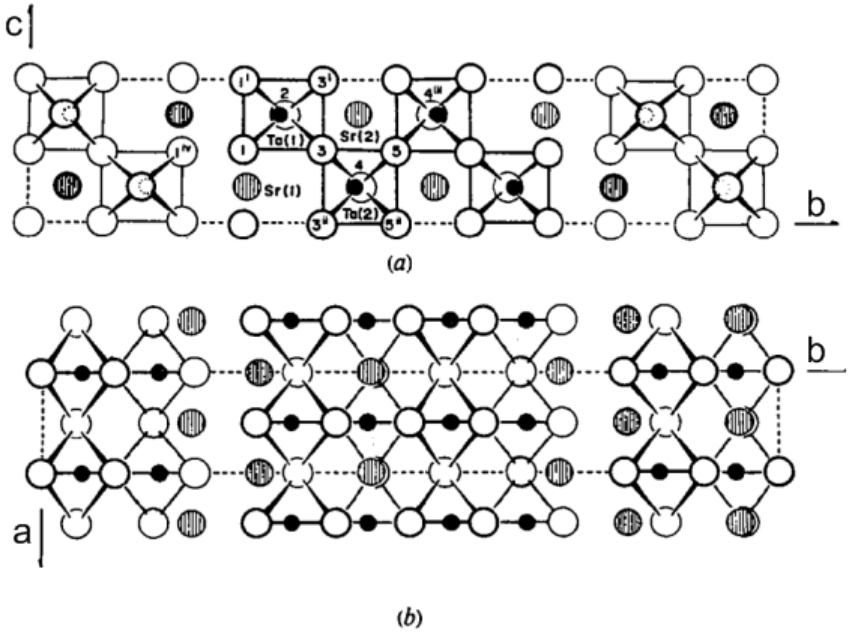

Fig.2.3.23. The crystal structure of $Sr_2Ta_2O_7$ viewed (a) along a; (b) along c direction.[84]

At room temperature, the structure is centro-symmetric, consistent with the paraelectric character of $Sr_2Ta_2O_7$.[87] The P-E hysteresis loop of $Sr_2Ta_2O_7$ crystal was measured at -190 ^{o}C (Fig.2.3.24). The remanent polarization P_r and coercive field at a maximum

applied field E_0=6.8 kV/cm were: P_r=0.69 uC/cm^2 and E_c=0.4 kV/cm, respectively.[5,79]

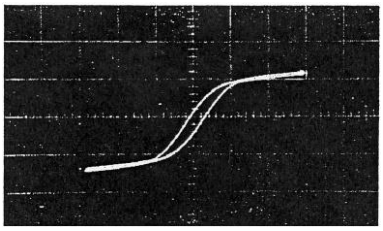

Fig.2.3.24. D-E hysteresis loop of $Sr_2Ta_2O_7$ c-plate crystal at -190 ^oC and 50Hz.[5]

The $Sr_{2-x}Eu_xTa_2O_7$ system is similar to the $Sr_{2-x}Eu_xNb_2O_7$ system. After heating at 1350 ^oC for 20h, only the orthorhombic phase was observed in products for composition with x<1, while when x>1 orthorhombic and hexagonal phases coexisted.[83]

For $Sr_2(Ta_{1-x}Nb_x)_2O_7$, $(Sr_{1-x}Ca_x)_2Ta_2O_7$, and $Sr_{2-x}Ca_xTa_{2-x}Nb_xO_7$ systems, the Curie points are presented in Table.2.10.[88] The Curie points all increase with increasing x in all the three systems.[79] Ferroelectric phase transition temperatures based on $Sr_2Ta_2O_7$-system are shown in Fig.2.3.25 and Table.2.10.[5,79]

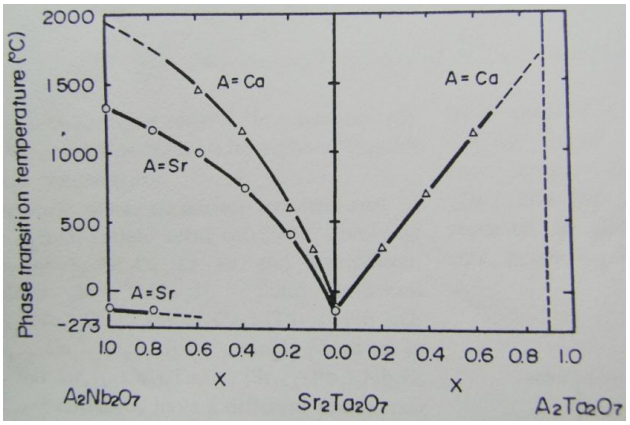

Fig.2.3.25. Ferroelectric phase transition temperatures of $A_2B_2O_7$-system solid solution as a function of solution ratio x.[79]

2.3.8. Calcium Niobate ($Ca_2Nb_2O_7$) and solid solution

$Ca_2Nb_2O_7$ was first obtained using a floating zone method on an image furnace.[89] CaO and Nb_2O_5 were used as raw materials. The crystal is colourless and transparent. At room temperature, $Ca_2Nb_2O_7$ has monoclinic structure with space group $P2_1$ and the lattice parameters are (a, b, c, β) = (7.80Å, 13.39Å, 5.50Å, 98.34°).[90] The projections of the monoclinic structure along a- and c- axes are shown in Fig.2.3.26.

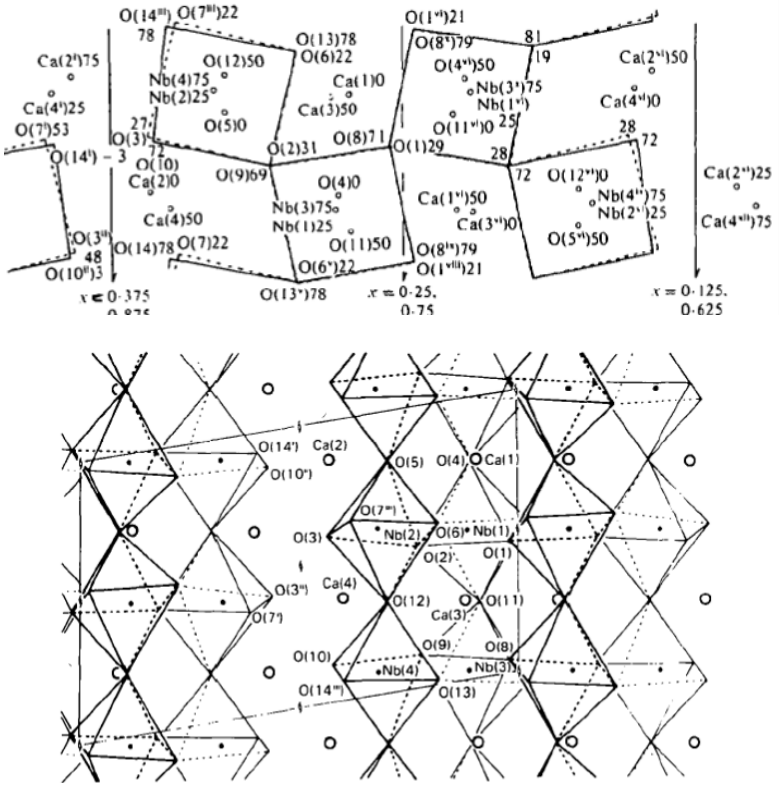

Fig.2.3.26. The structure of monoclinic $Ca_2Nb_2O_7$ projected along the a-axis and the c-axis.[90]

The $Ca_2Nb_2O_7$ ceramic was sintered by SPS and the grains showed a preferred grain orientation (Fig.2.3.27).[22] $Ca_2Nb_2O_7$ has a very high Curie point above 1580 ^oC which has been determined by the fact that no dielectric anomaly was found up to this

temperature shown in Fig.2.3.28. Most of the solid solution systems based on $Ca_2Nb_2O_7$ studied also involve other $A_2B_2O_7$ compounds, so they have already been discussed in the previous sections.

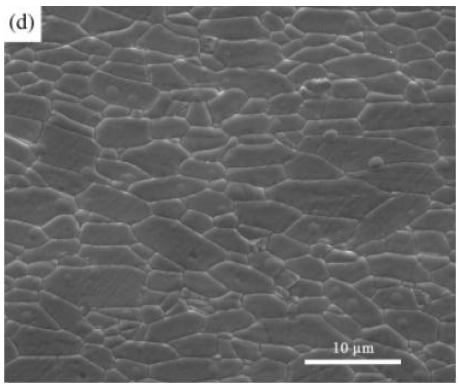

Fig.2.3.27. SEM images of $Ca_2Nb_2O_7$ ceramic.[22]

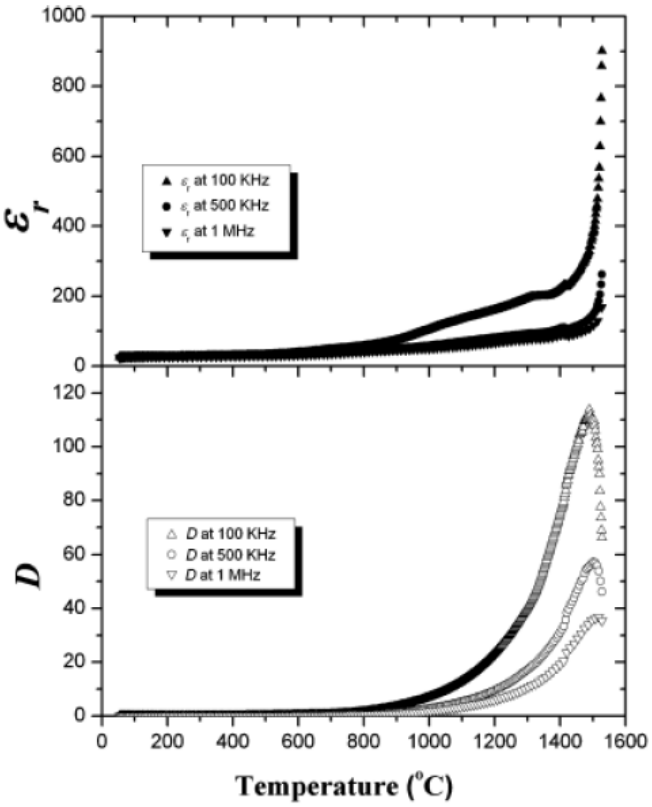

Fig.2.3.28. Temperature dependence of the permittivity and loss of $Ca_2Nb_2O_7$.[22]

2.3.9. Tungstates

The literature about phase transitions in polytungstates of monovalent elements is rather poor. The compounds are of interest due to their ferroelectric and ferroelastic properties.[91] Though they have a similar formula to PLS $A_2B_2O_7$ materials, they do not have PLS structures. So, this family here is just for comparison.

$Li_2W_2O_7$ crystals were synthesized by heating an intimate mixture of Li_2CO_3 and WO_3 in a platinum crucible at 800 ℃ for 5 hours and by cooling at a rate of 30-50 ℃/h.[91,92] They are colourless and transparent. $Li_2W_2O_7$ has a triclinic structure, which is built up of distorted WO_6 octahedra and LiO_4 tetrahedra. It has several phase transition points at 602 ℃, 674 ℃, 705 ℃ and 734 ℃. It has melting point of 738 ℃.[91,93] It is not known whether any of these phases are ferrolectric or ferroelastic.

For $Na_2W_2O_7$, there are two structures. $Na_2W_2O_7$ (LP) is obtained by a solid-state reaction under normal pressure using Na_2CO_3 and WO_3 as a precursor. $Na_2W_2O_7$ (HP) can be made by treating $Na_2W_2O_7$ (LP) at 3.2GPa and 1200 ℃.[94-96] The $Na_2W_2O_7$ (LP) has centro-symmetric structure with space group Cmca and the structure of $Na_2W_2O_7$ (HP) is noncentro-symmetric and isostructural to $Sr_2Nb_2O_7$ with orthorhombic structure ($Cmc2_1$).[95] So, $Na_2W_2O_7$ (HP) was suggested as a ferroelastric and ferroelectric material with melting point 738 ℃.[91,95] The cell parameters of $Na_2W_2O_7$ (HP) are (a, b, c, β) = (3.78Å, 26.61Å, 5.43Å, 90 °). Heating of $Na_2W_2O_7$ (HP) at ambient pressure and 1050K results in complete transformation to $Na_2W_2O_7$ (LP).[91,95]

$K_2W_2O_7$ was synthesized at high pressure 5-60 GPa and 500-1200 ℃. It is monoclinic with a space group of P21/c and lattice parameters (a, b, c, β) = (5.96Å, 13.65Å, 3.88Å, 90.42 °).[91] It has melting point of 632 ℃.[91] Compared to titanates and niobates, the tungstates have lower melting points which limit the possibility of observing a Curie point.

Table.2.11. Tungstates[91]

Compounds	Symmetry	Structure	Ferroelectric	Tc/ ℃	Space Group
$Li_2W_2O_7$	Non-centro	Triclinic	No report	No report	No report
$Na_2W_2O_7$(LP)	Centro	Orthorhombic	No	N/A	Cmca
$Na_2W_2O_7$(HP)	Non-centro	Orthorhombic	No Report	No report	$Cmc2_1$
$K_2W_2O_7$	Non-centro	Monoclinic	No report	No report	$P2_1/c$

2.4. Spark Plasma Sintering (SPS) and texturing

Spark plasma sintering (SPS) is a useful sintering technique to fabricate nanosized, high density, and textured materials. It is also known as field assisted sintering technique or pulsed electric current sintering.[97] Pulsed high direct- current (DC) current and uniaxial pressure are utilized to consolidate powders rapidly. It has become increasingly used in research to prepare structural and functional ceramics owing to the effectiveness of the process to rapidly and efficiently consolidate a wide variety of materials with novel microstructures.[98]

In the SPS technique, powders are first put in a graphite die firstly and then placed in a vacuum chamber. Then Joule heating is generated by the current passing through the die and the sample. In the meantime, a high uniaxial pressure is applied. The vacuum protects the graphite from oxidizing at high temperature (Fig.2.4.1-2.4.2).

Fig.2.4.1. Photo of a SPS machine (FCT, Germany).

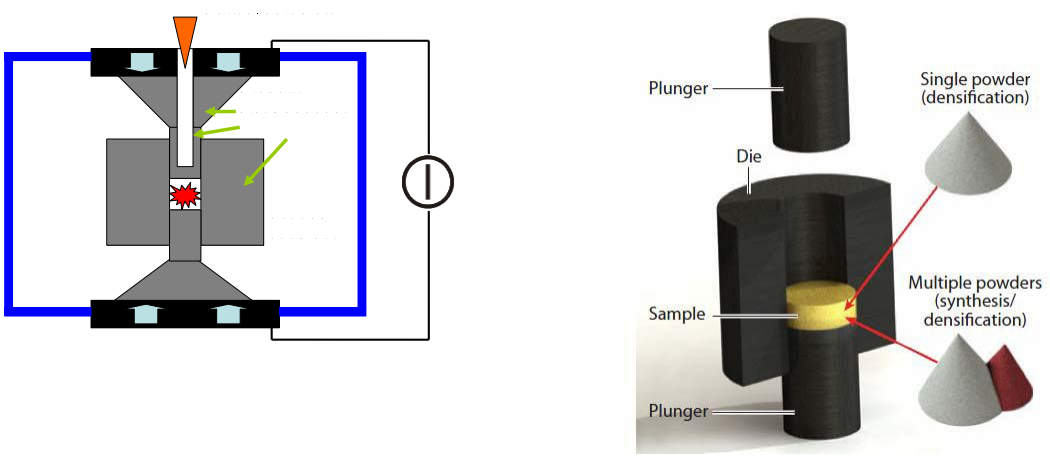

Fig.2.4.2. Schematic of a SPS furnace chamber (left) and a SPS die set (right).[99]

To some extent, SPS is similar to hot pressing (HP) which also utilizes a uniaxial pressure during the sintering process. However, the SPS process has a number of advantages compared with conventional sintering methods such as HP.[97] There are several main features attributed to the SPS sintering behavior: the high heating rate, the application of pressure and the effects of current.[100,101]

In this study, the SPS furnace (25/1 FCT, Germany) (Fig. 2.4.1) was used. It can achieve a temperature up to 2200 ℃ and a heating of rate up to 600 ℃/min. In the current study, the rapid heating rates (100 ℃/min) are used to produce highly dense and textured ferroelectric ceramics which cannot be achieved by the conventional sintering.

For piezoelectric applications, ferroelectric ceramics have to be poled under an electrical field. In ferroelectric single crystal, ferroelectric domains are polarized along one of several crystalographically allowed directions. The polarization direction can be switched under a sufficiently large electrical field. In ferroelectric ceramics, the

crystallite grains are randomly oriented and may contain one or several ferroelectric domains. The domains are constrained by the differently oriented neighboring grains when the domains in one grain attempt to switch under electrical poling. This makes the coercive field (Ec) of ceramics much higher than those of single crystals. If the grains are orientated in one direction, Ec decreases and the piezoelectric and ferroelectric properties can be improved.[102,103] Texture is the method to make preferred grain orientation in ceramics to improve the properties in certain directions.[104,105] So, the materials with anisotropic crystal structure such as PLS, Aurivillius, and tungsten bronze materials, are suitable for the texture technique. Fig.2.4.3 shows the texture process, which can help domain orientation, making ceramics with greater piezoelectric properties.

In the current study, a two-step hot-forging texturing method was utilized based on SPS sintering (Fig.2.4.3). The first step is to press the powder into a graphite die and sinter by SPS. In this step, the dense samples with minimal grain growth are obtained. Then, the sintered sample is placed into another larger die. It is then sintered at higher temperature to increase the grain size, and at the same time a high pressure is applied. During this step, the grains grow quickly, and the pressure constrains the growth direction and orientation of grains.[103,104]

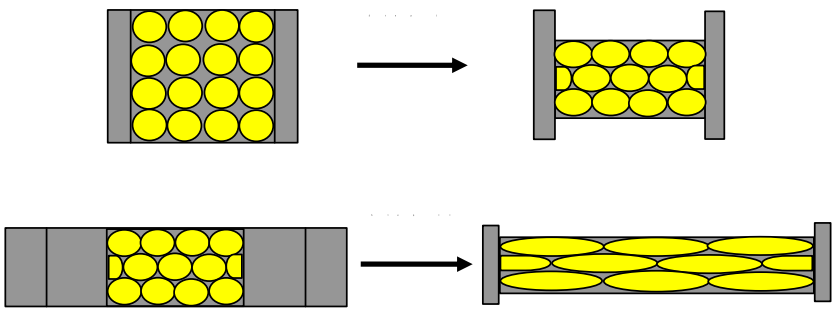

Fig.2.4.3. Texturing mechanisms by a SPS two-step method. The first step is to dense samples with minimal grain growth. In the second step, the grains grow quickly, and the pressure constrains the growth direction and orientation of grains

References

(1). Ishibashi, Y., Shiosaki, T., Yoshino, K., and Ichinose, N., *Japanese Journal of Applied Physics*, 1991. **30**: p. U2145.

(2). Lichtenberg, F., A. Herrnberger, and K. Wiedenmann, *Progress in Solid State Chemistry*, 2008. **36**(4): p. 253-387.

(3). Lichtenberg, F., Herrnberger, A., Wiedenmann, K., and Mannhart, J., *Progress in Solid State Chemistry*, 2001. **29**: p. 1-70.

(4). Subbarao, E.C., *Journal of Physics and Chemistry of Solids*, 1962. **23**(6): p. 665-676.

(5). Isupov, V.A., *Ferroelectrics*, 1999. **220**(1-2): p. 79-103.

(6). Levin, I., and Bendersky, L., *Acta Crystallographica Section B*, 1999. **55**(6): p. 853-866.

(7). Titov, Y., Sych, A., Markiv, V. , Belyavina, N., Kapshuk, A., and Yaschuk, V., *Journal of Alloys and Compounds*, 2001. **316**: p. 309-315.

(8). Titov, Y., Sych, A., and Kapshuk, A., *Inorganic Materials*, 1998. **34**: p. 496-498.

(9). Cava, R., and Roth, R., *Journal of Solid State Chemistry*, 1981. **36**: p. 139-147.

(10). Titov, Y., Sych, A., Sokolov, A., Kapshuk, A., and Yashchuk, V., *Inorganic Materials*, 2000. **36**: p. 625-628.

(11). Mariathasan, J., Finger, L., and Hazen, R., *Acta Crystallographica Section B*, 1985. **41**: p. 179-184.

(12). Cava, R., Santoro, A., Murphy, D., Zahurak, S., and Roth, R., *Solid State Ionics* 1981. **5**: p. 323-326.

(13). Atsushi, F., Hiroaki, M., and Akinori, K., *Materials science forum*, 2007. **3**: p. 534-536.

(14). Machida, M., Murakami, S., Kijima, T., Matsushima, S., and Arai, M., *Journal of Physical Chemistry B*, 2001. **105**: p. 3289-3294.

(15). Fride, V., Fabian, N., Magnus, S., and Tor, G., *Journal of Solid State Chemistry*, 2008. **108**: p. 5.

(16). Roth, R., Negas, T., Parker, H., Minor, D., and Jones, C., *Materials Research Bulletin*, 1977. **12**: p. 1173-1182.

(17). Titov, Y., Sych, A., Sokolov, A., Kapshuk, A., Markiv, V., and Belyavina, N., *Journal of Alloys and Compounds*, 2000. **311**: p. 252-255

(18). Hartenbach, I., Lissner, F., Nikelski, T., Meier, S., Muller-Bunz, H., and Schleid, T., *Zeitschrift für anorganische und allgemeine Chemie*, 2005. **631**: p. 2377-2382.

(19). Santoro, A., Marezio, M., Roth, R., and Minor, D., *Journal of Solid State Chemistry*, 1980. **35**(2): p. 167-175.

(20). Titov, Y., Sych, A., Kapschuk, A., and Yashchuk, V., *Inorganic Materials*, 2001. **37**(3): p. 294-297.

(21). Titov, Y., Sych, A., Markiv, V., Belyavina, N., Kapshuk, A., Yaschuk, V., and Slobodyanik, M., *Journal of Alloys and Compounds*, 2002. **337**: p. 89-93.

(22). Ning, H., Yan, H., and Reece, M., *Journal of the American Ceramic Society*, 2010.

93(5): p. 1409-1413.

(23). Nanamatsu, S., Kimura, M., Doi, K., and Takahashi, M., *Journal of the Physical Society of Japan*, 1971. **30**: p. 300-301.

(24). Carpy, A., Amestoy, P., and Galy, J., *Comptes Rendus de l Academie des Sciences Serie ii Fascicule C-Chimie*, 1972. **275**: p. 833.

(25). Yan, H., Ning, H., Kan, Y., Wang, P., and Reece, M., *Journal of the American Ceramic Society*, 2009. **92**(10): p. 2270-2275

(26). Kimura, M., Nanamats.S, Doi, K., Matsushi. S., Igarashi, S., and Takahash.M., *Nec Research and Development*, 1973. **17**: p. 10-14.

(27). Kimura, M., Matsushi, S., Nanamats, S., Takahash, M., and Doi, K., *Japanese Journal of Applied Physics*, 1972. **11**: p. 904-907.

(28). Kimura, M., Nanamatsu, S., Kawamura, T., and Matsushita, S., *Japanese Journal of Applied Physics*, 1974. **13**: p. 1473-1474.

(29). Drews, A., Roth, R., and Vanderah, T., *Materials Research Bulletin*, 1996. **31**: p. 153-162

(30). Levin, I., Cline, J., Roth, R., and Vanderah, T., *Journal of Solid State Chemistry*, 2000. **150**: p. 17-21.

(31). Schuckel, K., *Zeitschrift für anorganische und allgemeine Chemie*, 1985. **528**: p. 114-116

(32). Hervieu, M., Studer, F., and Raveau, B., *Journal of Solid State Chemistry*, 1977. **22**: p. 17-19.

(33). Zuniga, F.J. and J. Darriet, $NaCa_4Nb_5O_{17}$: a Layered Perovskite $A_nB_nO_{3n+2}$ Compound. *Acta Crystallographica Section C*, 2003. **59**(2): p. i18-i20.

(34). Levin, I., L.A. Bendersky, T.A. Vanderah, R.S. Roth, and O.M. Stafsudd, *Materials Research Bulletin*, 1998. **33**(3): p. 501-517.

(35). Levin, I., L.A. Bendersky, T.A. Vanderah, *Philosophical Magazine A Physics of Condensed Matter, Defects and Mechanical Properties*, 2000. **80**: p. 4.

(36). Nanot, M., F. Queyroux, J.C. Gilles, and J.J. Capponi, *Journal of Solid State Chemistry*, 1986. **61**(3): p. 315-323.

(37). Nanot, M., Queyroux, F., Gilles, J., and Portier, R., *Journal of Solid State Chemistry*, 1981. **38**: p. 74-81.

(38). Zakharov, N., Klyuev, N., and Toporov, Y., *Zhurnal Fizicheskoi Khimii*, 1999. **73**(5): p. 934-936.

(39). Shao, Z., Saitzek, S., Blach, J., Sayede, A., Roussel, P., and Desfeux, R., *European Journal of Inorganic Chemistry*, 2011. **3**: p. 7.

(40). Porotnikov, N., and Bazuev, G., *Zhurnal Neorganicheskoi Khimii*, 1989. **34**: p. 250-251.

(41). Pandit, A., and Singh, R., *Materials Letters*, 1991. **12**: p. 185-190.

(42). Sych, A.M., S.Y. Stefanovich, Y.A. Titov, T.N. Bondarenko, and V.M. Melnik, *Inorganic Materials*, 1991. **27**(12): p. 2229-2230.

(43). Yamamoto, J.K. and A.S. Bhalla, *Journal of Applied Physics*, 1991. **70**(8): p. 4469-4471.

(44). Zhang, F. X., Lian, J., Becker, U., Ewing, R. C., Wang, L. M., Hu, J., and Saxena, S. K., *Journal of Solid State Chemistry*, 2007. **180**(2): p. 571-576.

(45). Ishizawa, N., F. Marumo, S. Iwai, M. Kimura, and T. Kawamura, *Acta Crystallographica Section B-Structural Science*, 1982. **38**(FEB): p. 368-372.

(46). Nanamatsu, S., M. Kimura, and N. Yamada, *Nec Research and Development*, 1974. **34**: p. 39-42.

(47). Fuierer, P.A. and R.E. Newnham, *Journal of the American Ceramic Society*, 1991. **74**(11): p. 2876-2881.

(48). Bruyer, E. and A. Sayede, *Journal of Applied Physics*, 2010. **108**(5): p. 053705.

(49). Shao, Z., Saitzek, S., Roussel, P., Mentre, O., Gheorghiu, F. P., Mitoseriu, L., and Desfeux, R., *Journal of Solid State Chemistry*, 2010. **183**: p. 1652-1662.

(50). Fu, X. Z., Li, Z. H., Xue, H., and Wang, X. X., *Journal of Molecular Catalysis A: Chemical*, 2006. **260**: p. 56-61.

(51). Hwang, D.W., Lee, J. S., Li W., Oh, S. H., *ChemInform*, 2003. **34**(38): p. 4963-4970.

(52). Scheunemann, K., and Mullerbuschbaum, H., *Journal of Inorganic and Nuclear Chemistry*, 1975. **37**: p. 2261-2263.

(53). Winfield, G., Azough, F., and Freer, R., *Ferroelectrics*, 1992. **133**(1): p. 181 - 186.

(54). Pai, R., Mukerjee, S., and Venugopal, V., *Solid State Ionics*, 2011. **187**: p. 85-92.

(55). Harvey, E., Whittle, K., Lumpkin, G., Smith, R., and Redfern, S., *Journal of Solid State Chemistry*, 2005. **178**: p. 800-810.

(56). Tyagi, A., and Mandal, B., *Materials Science and Engineering: B*, 2007. **136**: p. 46-49.

(57). Charvin, P., Abanades, S., Beche, E., Lemont, F., and Flamant, G., *Solid State Ionics*, 2009. **180**: p. 1003-1010.

(58). Beche, E., Charvin, P., Perarnau, D., Abanades, S., and Flamant, G., *Surface and Interface Analysis*, 2008. **40**: p. 264-267.

(59). Preuss, A. and R. Gruehn, *Journal of Solid State Chemistry*, 1994. **110**(2): p. 363-369.

(60). Titov, Y.A., A.P. Leonov, A.M. Sych, S.Y. Stefanovich, V.V. Lashneva, and Y.N. Venevtsev, *Inorganic Materials*, 1985. **21**(10): p. 1515-1519.

(61). Kim, W.S., J.-K. Yang, C.-K. Lee, H.-S. Lee, and H.-H. Park, *Thin Solid Films*, 2008. **517**(2): p. 506-509.

(62). Kozmin, P. A., Zakharov, N. A., and Surazhskaya, M. D., *Journal of Inorganic Materials*, 1997. **33**: p. 850-852.

(63). Melekh, B. T., Kartenko, N. F., Pevtsov, A. B., Shadrin, E. B., Filin, Y. N., and Andreev, A. A., *Zhurnal Neorganicheskoi Khimii*, 1980. **25**: p. 3215-3218.

(64). Krishnankutty, K., and Dayas, K. R., *Bulletin of Materials Science*, 2008. **31**: p. 907-918.

(65). Wenger, C., Sorge, R., Schroeder, T., Mane, A. U., Knoll, D., Dabrowski, J., and Mussig, H. J., *International Microwave Symposium*, 2006. **1**: p. 15-17.

(66). Henderson, N. L., Baek, J., Halasyamani, P. S., and Schaak, R. E., *Chemistry of*

Materials, 2007. **19**(8): p. 1883-1885.

(67). Bondarenko, T. N., Uvarov, V. N., Borisenko, S. V., Teterin, Y. A., Dzeganovski, V. P., Sych, A. M., and Titiv, Y. A., *Journal of the Korean Physical Society*, 1998. **32**: p. S65-S67.

(68). Pandit, A. K., Ansari, T. H., Singh, R. S., Singh, R. A., and Wanklyn, B. M., *Journal of Materials Science*, 1992. **27**: p. 4080-4084.

(69). Zhang, F. X., Manoun, B., Saxena, S. K., and Zha, C. S., *Applied Physics Letters*, 2005. **86**: p. 1453.

(70). Igarashi, K., Koumoto, K., and Yanagida, H., *Journal of Materials Science*, 1987. **22**: p. 2828-2832.

(71). Havelia, S., Wang, S., Balasubramaniam, K. R., and Salvador, P. A., *Journal of Solid State Chemistry*, 2009. **182**: p.1603-1610.

(72). Sych, A. M., Stefanovich, S. Yu., Titov, Y. A., Bondarenko, T. N., and Melnik, V. M., *Inorganic Materials*, 1991. **27**: p. 2229-2230.

(73). Ishizawa, N., Marumo, F., Kawamura, T., and Kimura, M., *Acta Crystallographica Section B-Structural Science*, 1975. **31**: p.1912-1915.

(74). Osman, M. A., Zeinally, A. K., Lebedeva, N. N., Efendiev, S. M., Grandolfo, M., and Vecchia, P., *Ferroelectrics*, 1981. **38**: p. 861-863.

(75). Grey, I. E., Mumme, W. G., Ness, T. J., Roth, R. S., and Smith, K. L., *Journal of Solid State Chemistry*, 2003. **174**: p. 285-295.

(76). Hushur, A., and Kojima, S., *Materials Science and Engineering A - Structural*

Materials Properties Microstructure and Processing, 2006. **442**: p. 35-38.

(77). Daniels, P., Tamazyan, R., Kuntscher, C. A., Dressel, M., Lichtenberg, F., van Smaalen, S., *Acta Crystallographica Section B - Structural Science*, 2002. **58**: 970-976.

(78). Takahash.M, Nanamats.S, and Kimura, M., *Journal of Crystal Growth*, 1971. **13**: p. 681.

(79). Nanamatsu, S., Kimura, M., and Kawamura, T., *Journal of the Physical Society of Japan*, 1975. **38**: p. 817-824.

(80). Podkrytov, A. L., Animitsa, I. E., Shindelman, N. K., Zhukovskii, V. M., Lozhkina, E. B., and Perelyaeva, L. A., *Inorganic Materials*, 1988. **24**: p. 1742-1745.

(81). Kudakaeva, S. R., Podkorytov, A. L., Sokolova, E. V., Shtin, S. A., *Russian Journal of Inorganic Chemistry*, 2005. **50**: p. 866-868.

(82). Podkorytov, A., Pantyukhina, M., Shtin, S., and Zhukovskii, V., *Inorganic Materials*, 2000. **36**: p. 3.

(83). Sato, K., Adachi, G. Y., and Shiokawa, J., *Journal of Solid State Chemistry*, 1978. **24**: p.169-174.

(84). Ishizawa, N., Marumo, F., Kawamura, T., and Kimura, M., *Acta Crystallographica Section B-Structural Science*, 1976. **32**: p. 2564-2566.

(85). Yamamoto, N., Yagi, K., Honjo, G., Kimura, M., and Kawamura, T., *Journal of the Physical Society of Japan*, 1980. **48**: p.185-191.

(86). Ismailzade, I. H., and Ismailov, R. M., *Izvestiya Akademii Nauk Azerbaidzhanskoi Ssr Seriya Fiziko-Tekhnicheskikh I Matematicheskikh Nauk*, 1980. p.67-70.

(87). Ishizawa, N., Marumo, F., Kawamura, T., and Kimura, M., *Acta Crystallographica Section B*, 1976. **32**: p. 2564-2566.

(88). Yoshino, M., and Kakihana, M., *Chemistry of Materials*, 2002. **14**: p. 3369-3376.

(89). Nanamats.S, and Kimura, M., *Journal of the Physical Society of Japan*, 1974. **36**: p. 1495-1495.

(90). Ishizawa, N., Marumo, F., Iwai, S., Kimura, M., and Kawamura, T., *Acta Crystallographica Section B - Structural Science*, 1980. **36**: p. 763-766.

(91). Isupov, V. A., *Ferroelectrics*, 2005. **322**: p. 83-114.

(92). Okada, K., Morikawa, H., Marumo, F., and Iwai, S., *Acta Crystallographica Section B-Structural Science*, 1975. **31**: p. 1451-1454.

(93). Magarill, S. A., Klevtsov. R., Bakakin, V. V., *Kristallografiya*, 1973. **18**: p. 269-276.

(94). Miyake, M., Okada, K., Iwai, S., Ohno, H., and Furukawa, K., *Journal of the Chemical Society, Faraday Transactions 1: Physical Chemistry in Condensed Phases*, 1978. **74**: p. 1880-1884.

(95). Range, K. J., and Haase, H., *Acta Crystallographica Section C-Crystal Structure Communications*, 1990. **46**: p. 317-318.

(96). Sandeep, P., Mahapatra, R., Choudhary, A., *Physica Status Solidi (a)*, 2004. **201**: p. 8.

(97). Omori, M., *Materials Science and Engineering a-Structural Materials Properties Microstructure and Processing*, 2000. **287**: p. 183-188.

(98). Tokita, M., *Functionally Graded Materials*, 2001. **114**: p. 283-290.

(99). Garay, J.E., *Annual Review of Materials Research*, 2010. **40**(1): p. 445-468.

(100). Suarez, D.Y., I.M. Reaney, and W.E. Lee, *Journal of Materials Research*, 2001. **16**(11): p. 3139-3149.

(101). Li, W., Gao, L., Hong, J. S., and Miyamoto, H., *Journal of Inorganic Materials*, 2000. **15**: p. 269-274.

(102). Jaffe, B., W.R. Cook, and H. Jaffe, Piezoelectric ceramics. 1971. London and New York: Academic Press.

(103). Jones, J.L., B.J. Iverson, and K.J. Bowman, *Journal of the American Ceramic Society*, 2007. **90**(8): p. 2297-2314.

(104). Kimura, T., *Journal of the Ceramic Society of Japan*, 2006. **114**(1): p. 15-25.

(105). Messing, G., Trolier-McKinstry, S., Sabolsky, E., Duran, C., Kwon, S., Brahmaroutu, B., Park, P., Yilmaz, H., Rehrig, P., Eitel, K., Suvaci, E., Seabaugh, M., and Oh, K., *Critical Reviews in Solid State & Materials Science*, 2004. **29**(2): p. 45-96.

Chapter III. Experiment Procedures

3.1. Powder preparation

Fine and homogeneous powder is required to make dense and single phase ceramics. The starting materials were La_2O_3 (99.99% purity, Alfa Aesar), CeO_2 (99.9% purity, Segma-Adrich), Pr_6O_{11} (99.9% purity, Segma-Adrich) Nd_2O_3 (99% purity, Alfa Aesar), TiO_2 (99.95% purity, Alfa Aesar), $SrCO_3$ (99% purity, Alfa Aesar), $BaCO_3$ (99.8% purity, Alfa Aesar) and Nb_2O_5 (99.9% purity, Segma-Adrich). Starting materials were weighed out according to the stoichiometric formula of the desired composition. Then, wet ball milling was employed to mix the powders and reduce the particle size. The raw powder was placed in a cylindrical nylon pot containing ZrO_2 milling balls and ground by ball milling (QM-3SP4, Nanjing University Instrument Plant, China) with ethanol (Fig.3.1.1(a)). For a high milling efficiency, the ratio of the volume of powders, ethanol and milling balls was about 1:2:3.[1] The milling balls were a mixture of 5 mm and 10 mm in diameter. After the wet ball milling, the mixture was dried in a drying oven (Elite) at 80 ℃ for 8 hours to evaporate the liquid. Then the dried material was sieved using a stainless steel sieve (aperture diameter 250 μm) to control the particle size.

In this study, solid state reaction was used to produce all of the compounds studied. The mixed raw powders were put in alumina crucibles heated and calcined to a high temperature in a conventional chamber furnace (Elite, BRF 15/5) (Fig.3.1.1(b)). The ideal calcination temperature was chosen to be high enough to obtain single phase

materials, but low enough to permit easy re-milling. After calcination, the powders were re-milled and sieved to reduce particle size.

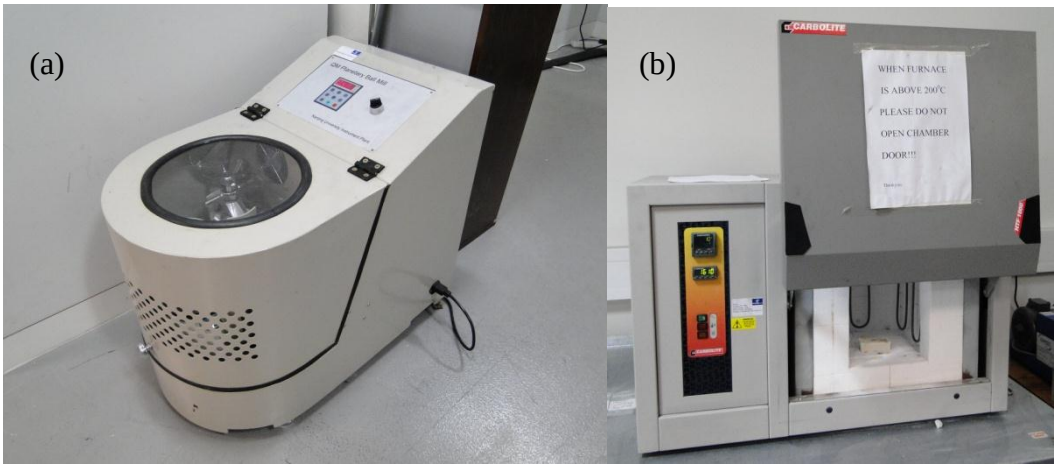

Fig.3.1.1 Photos of (a) the QM-3SP4 planetary ball milling machine and (b) high temperature furnace. (Lenton, BRF 15/5)

3.2. Sintering by SPS

The $A_2B_2O_7$ powders were sintered in graphite dies by a Spark Plasma Sintering furnace (HPD 25/1 FCT, Germany) (Fig.2.4.1). Graphite dies and punches were used to sinter $A_2B_2O_7$ powders due to its good electrical conductivity and mechanical strength at high temperature. Graphite foils were utilized to enclose the samples to stop contact between the dies and samples and maintain a good thermal and electrical contact between dies and punches.

For untextured samples, which were sintered by a one-step method, $A_2B_2O_7$ powders were put in graphite dies with 20 mm diameter and sintered by SPS. Textured $A_2B_2O_7$ ceramics were obtained using a two-step method. In the first step, the powders were sintered in a 20mm-diameter graphite die. The sintering temperature corresponded to the temperature range during which the shrinkage speed is high. After this stage, the densities of the ceramics were high (>95%), but the grains were only slightly larger than the starting powder.

In the second step, the densified compacts were placed in larger graphite dies (30 mm diameter) to sinter at a higher temperature. After sintering, the sintered samples were annealed in air for 15-20 hours in a chamber furnace (Lenton, BRF 15/5) to remove any carbon contamination. This increased the resistivity of the samples for electrical measurement.

Finally, the sample were cut into plates whose normal lines were parallel or

perpendicular to the pressing direction and are referred to as SPS [//] and SPS [⊥] (Fig.3.2.1), respectively (Cutting machine: Accutom-5, Struers). Then the sample were ground and machine polished (Forcipol 1V, Metkon).

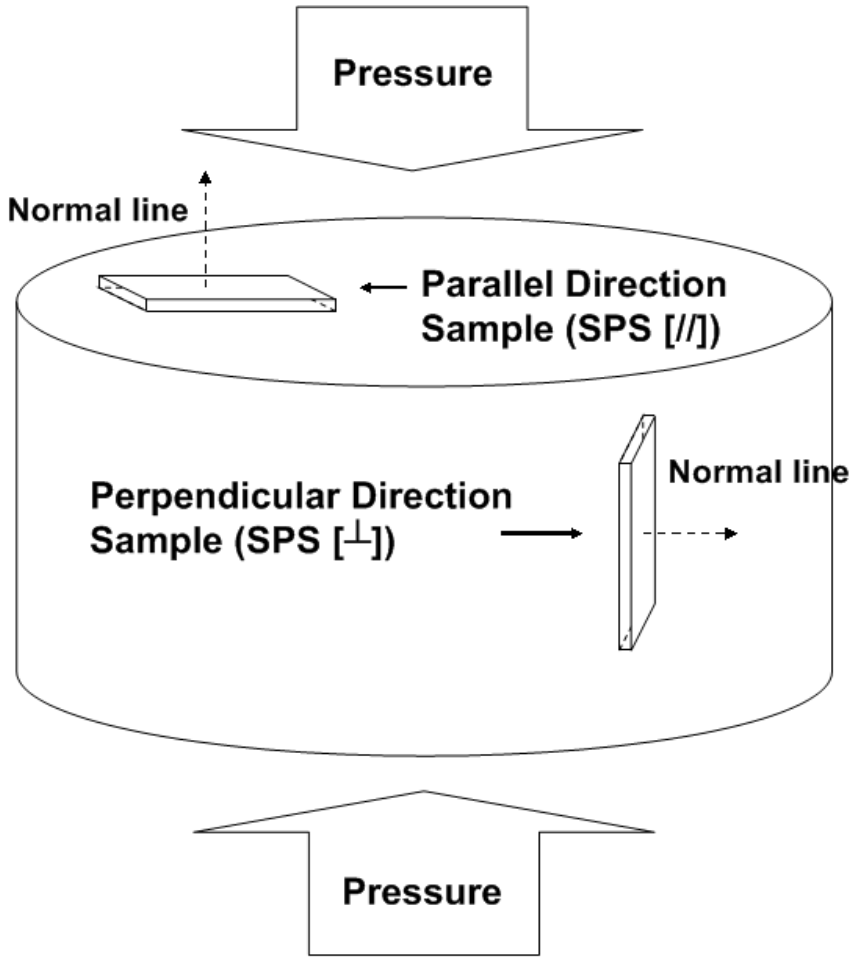

Fig.3.2.1. Diagrammatic sketch of SPS (//) and SPS (⊥) from a bulk ceramic.

3.3. Characterization

3.3.1. Density measurement

The Archimedes principle was used to measure the densities of the bulk ceramics. The density was calculated from the following relationship:[2]

$$\rho = \frac{m_1 \rho_0}{m_2 - m_3} \tag{3.1}$$

Where m_1 is the mass of the dry sample; m_2 is the mass of the sample after soaking in water; m_3 is the mass weighed while the sample is immersed in water. ρ_0 is the density of water, For a sample which is nearly fully dense or only contains closed porosity, so $m_1=m_2$. The relationship becomes:

$$\rho = \frac{m_1 \rho_0}{m_1 - m_3} \tag{3.2}$$

3.3.2. X-ray diffraction, Scanning electron microscopy and X-ray Photoelectron Spectra

X-ray diffraction (XRD) is a non-destructive analytical technique based on Bragg's Law, which provides information about the chemical composition and crystallographic structure of materials. In this work, X-ray diffraction (XRD) patterns for the powders and polished ceramics were obtained with an X-ray diffractometer (Siemens D5000) using Cu Kα radiation.

The X-ray diffraction pattern collection was done by experimental officer Dr. Rory Wilson. Samples were mounted on zero background silicon single crystal substrates. The powder samples were mounted either as a thin slurry in acetone or just sprinkled on as a fine powder. The solid samples were ground to have a smooth flat surface for diffraction to be taken from. Phase identification was accomplished by comparing the peaks (positions and relative intensities) from the samples with the data from a standard database provided by the International Center for Diffraction Data (ICDD). The comparison was done with the help of software package X'Pert HighScore version 2.0.

The degree of grain orientation of the textured ceramics was estimated using the Lotgering orientation factor, f, from the XRD peak intensities I using the equation[3]:

$$f = \frac{P - P_0}{1 - P_0} \tag{3.3}$$

where

$$P = \frac{\sum I(h00)}{\sum I(hkl)} \quad \text{and} \quad P_0 = \frac{\sum I_0(h00)}{\sum I_0(hkl)} \tag{3.4}$$

$\sum I(h00)$ and $\sum I(hkl)$ are the sum of the XRD peak intensities of all the (h00) and (hkl) peaks, respectively for ceramic. I_0(h00) and I_0(hkl) are the sum of the XRD intensities of all the (h00) and (hkl) peaks, respectively for powder.

The microstructures of the ceramic samples were observed using a scanning electron microscope (SEM) (FEI, Inspect F). The samples for SEM characterisation were

polished using silicon carbide paper (up to grade 4000) and then thermally etched for 15 min to reveal their grain structures. ESCALAB 250 X-ray Photoelectron Spectrometer (Thermo Corp.) with monochromatized Al Kα (1486.5 eV) X-ray source was employed to analyse the surface bonding states of the samples with a pass energy of 20 eV.

3.3.3. Electrical measurements

Electrodes were made by coating the samples with platinum paste (Gwent Electronic Materials Ltd, C2011004D5) and fired above 1000 ℃ for electrical properties measurements. The electrode layer was prepared so that it was thin, uniform and adhered strongly to the ceramic substrate.

The frequency dependence of the dielectric constants and losses were obtained using a Precision Impedance Analyzer (Agilent, 4294A). The capacitances C measured directly by the equipment were converted into the relative dielectric constants by the following equation:

$$\varepsilon = \frac{Ct}{\varepsilon_0 A} \tag{3.5}$$

Where t and A are the thickness and the electrode area of the sample, respectively; ε_0 is the dielectric constant in vacuum ($\varepsilon_0 = 8.854*10^{-12}$ F/m).

The temperature dependence of the dielectric constants and losses at different frequencies was obtained using a Precision LCR Meter (Agilent, 4284A). The meter was connected to a high temperature (T_{max}=1600 ℃) tube furnace (Lenton, LTF

16/--/180). An alumina sample substrate was coated with Pt to be conductive. The heating rate was 3 ℃/min. The two Pt probes connect the substrate and the sample. The spot temperature of the sample was measured using a type R thermocouple according to the Seebeck effect. The voltage difference was measured by a multimeter (HP, 34401A) (Fig.3.3.1).

All the data (frequency, capacitance, and dielectric loss) were recorded by a computer using a lab view software. The relative dielectric constants were derived from the capacitance. The accuracy of the temperature was evaluated by using materials with known Curie points (reference material: $LiNbO_3$, 1140 ℃).

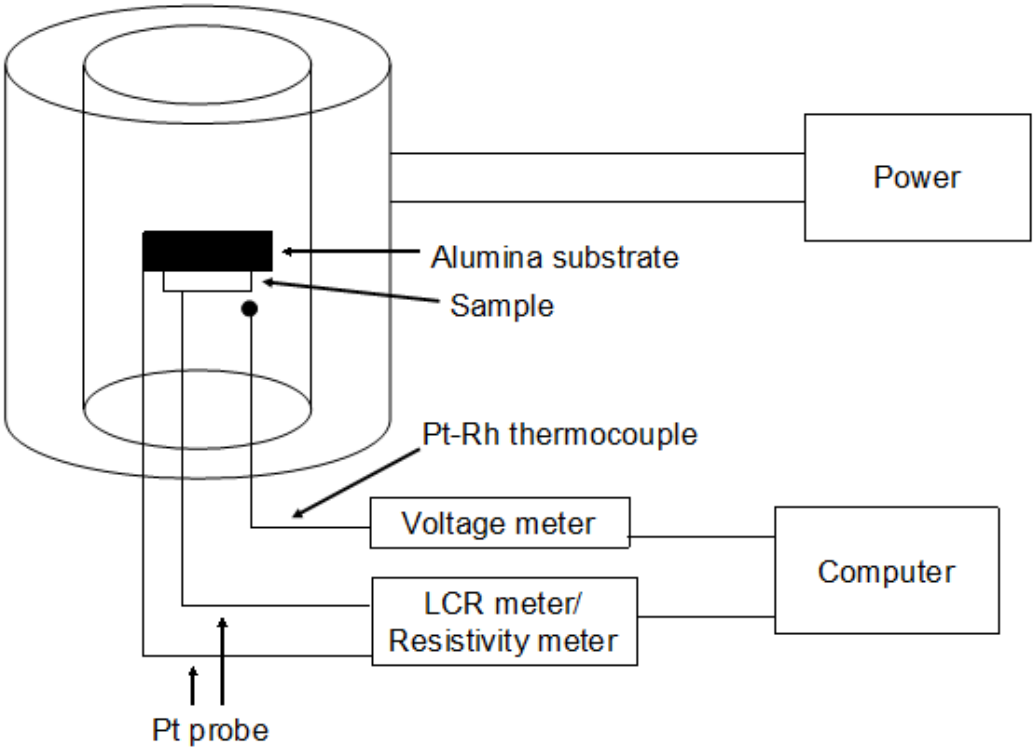

Fig.3.3.1. Schematic illustration of the setup for high temperature dielectric and resistivity measurement.

The DC resistivity was measured using a high resistance meter (KEITHLEY, 6517A) . The samples for resistivity measurement were about 1 mm in thickness. The resistance data was recorded at 10 V after holding at different temperatures for 15 min. The electrical stability measurements were carried out by holding the samples at certain different temperatures and measuring the resistance as a function of time.

The resistivity was derived from the resistance, R, according to the following equation:

$$\rho = \frac{RA}{l} \tag{3.6}$$

Where l and A is the thickness and electrode area of the sample, respectively.

The ferroelectric P-E and I-E hysteresis loops were measured by a ferroelectric hysteresis measurement tester (NPL, UK) in silicone oil (SIL 300) at about 200℃ and 10 Hz. Samples for piezoelectric measurements were poled under various DC electric fields (150-200 kV/cm) in silicone oil (SIL 300) (Fig. 3.9). Then their piezoelectric constant d_{33} was measured by a quasi-static d_{33} meter (CAS, ZJ- 3B). The accuracy of the d_{33} meter for measuring small coefficients was calibrated by X-cut quartz (d_{33}=2.3±0.1) pC/N. The thermal depoling or thermal stability of d_{33} measurements were tested by holding the samples at a certain range of temperatures (from room temperature to just above the Curie point) in the furnaces. Then d_{33} was measured at room temperature.

References

(1). David Kingery, W., Bowen, H., Uhlman, D., *Introduction to Ceramics*, 2nd Edition ed., 1976.

(2). German, R.M., Sintering Theory and Practice. 1996. New York: John Wiley & Sons, Inc.

(3). Lotgering, F.K., Topotactical Reactions with Ferrimagnetic Oxides Having Hexagonal Crystal Structures--I. *Journal of Inorganic and Nuclear Chemistry*, 1959. **9**(2): p. 113-123.

Chapter IV. Results - Praseodymium Titanate ($Pr_2Ti_2O_7$)

4.1. Introduction

The materials with the PLS structure have been confirmed as ferroelectric materials with super high Curie point, such as $Sr_2Nb_2O_7$ (1327 ℃, SNO)[1-3]; $La_2Ti_2O_7$ (1461 ℃, LTO)[4,5] and $Nd_2Ti_2O_7$ (1482 ℃, NTO).[5,6] $Pr_2Ti_2O_7$ (PTO) also belongs to the $A_2B_2O_7$ family. The structure has been investigated by P.A.Koz'min et al.[7] This confirmed it has a non-centrosymmetric structure and a high temperature phase transition (1750 ℃).[8,9] However, this did not provide direct evidence that this phase transition corresponds to the ferroelectric Curie point because there was no report to confirm if PTO is ferroelectric.

In this chapter, dense, textured PTO ceramic was prepared by spark plasma sintering using a two-step method for the first time and PTO was shown for the first time to be ferroelectric because it showed piezoelectric activity after poling ($d_{33} = 0.5 \pm 0.1$pC/N).

4.2. Experiment Details

The PTO powder was obtained by the mixed oxide route. Pr_6O_{11} (99.9%) and TiO_2(99.9%) were used as the starting materials. The powders were ball milled and then calcinated for 4h at 1300 ℃. The powders were then re-milled for 4 h to break any agglomerates and reduce the particle size.

The synthesized powders were sintered by SPS. A heating rate of 100 ℃/min was used in all cases. The ceramic samples were sintered in a 20-mm-diameter graphite die under 50MPa at 1200 ℃, 1250 ℃, 1300 ℃ and 1350 ℃ for 5mins. All the above samples were oxidized at a temperature 200 ℃ below their sintering temperature for 15h to remove any carbon contamination and reverse any reduction produced during SPS.

A textured ceramic sample was obtained using a two-step sintering method. First, the PTO powder was pressed in a 20-mm-diameter graphite die and sintered at 1150 ℃ under 50 MPa for 3 min. In the second stage of texturing, the sample was placed in a larger die of 30 mm diameter and sintered at 1350 ℃ under 80MPa for 5min. The sintered PTO disk was then annealed at 1200 ℃ for 15h.

4.3. Results and Discussion

Fig.4.3.1 shows the XRD patterns of the PTO powder and a polished surface of the untextured and textured ceramic sample. The diffraction peaks match the indexed peaks for the PTO (XRD PDF card: 04-005-7187) structure parameters, which means the materials are single phase within the sensitivity of the technique.

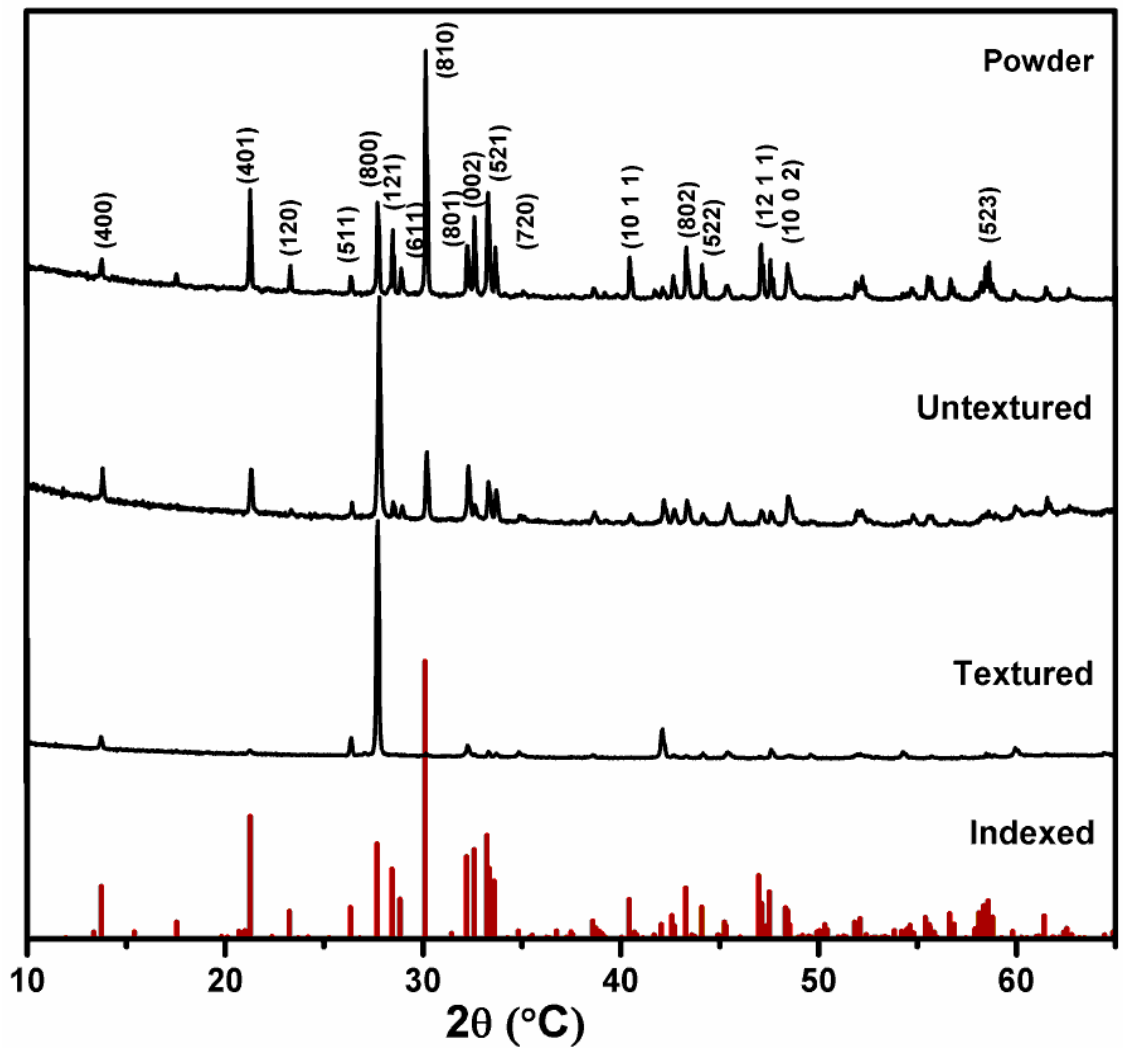

Fig.4.3.1. The XRD patterns of the PTO powder and a polished surface of the untextured and textured ceramics.

Fig.4.3.2 shows the scanning electron microscope (SEM) images of calcined PTO powder before and after ball milling. After calcination, the powder has some agglomeration and the particle size was about 2 um. The ball milling process can break the agglomeration and reduce particle size. After ball milling, the average particle size was about 0.7 um and the particles became more homogeneous.

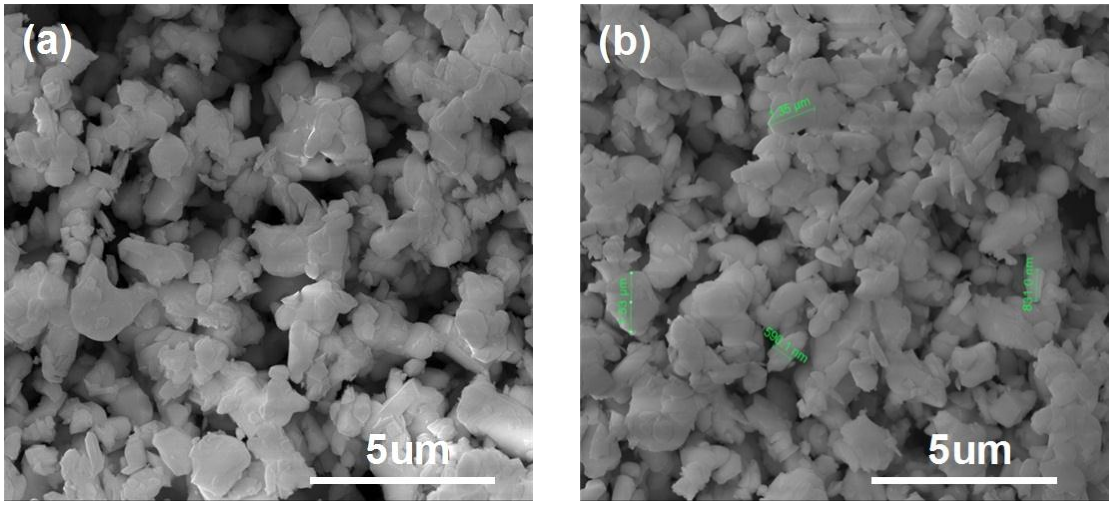

Fig.4.3.2 SEM of PTO powder after calcinations at 1300 ℃: (a) before ball milling; (b) after ball milling.

Fig 4.3.3 shows the relative density of PTO ceramic samples sintered at several temperatures. The theoretical density of PTO is 5.95 g/cm^3.[9] The density increases with increasing sintering temperature, when the temperature was below 1350 ℃. When the sintering temperature increased further, the density decreased. At higher temperatures, the grains elongate, which facilitates the formation of pores at the grain boundaries, so the density decreased. After texturing, the density was 96.3%.

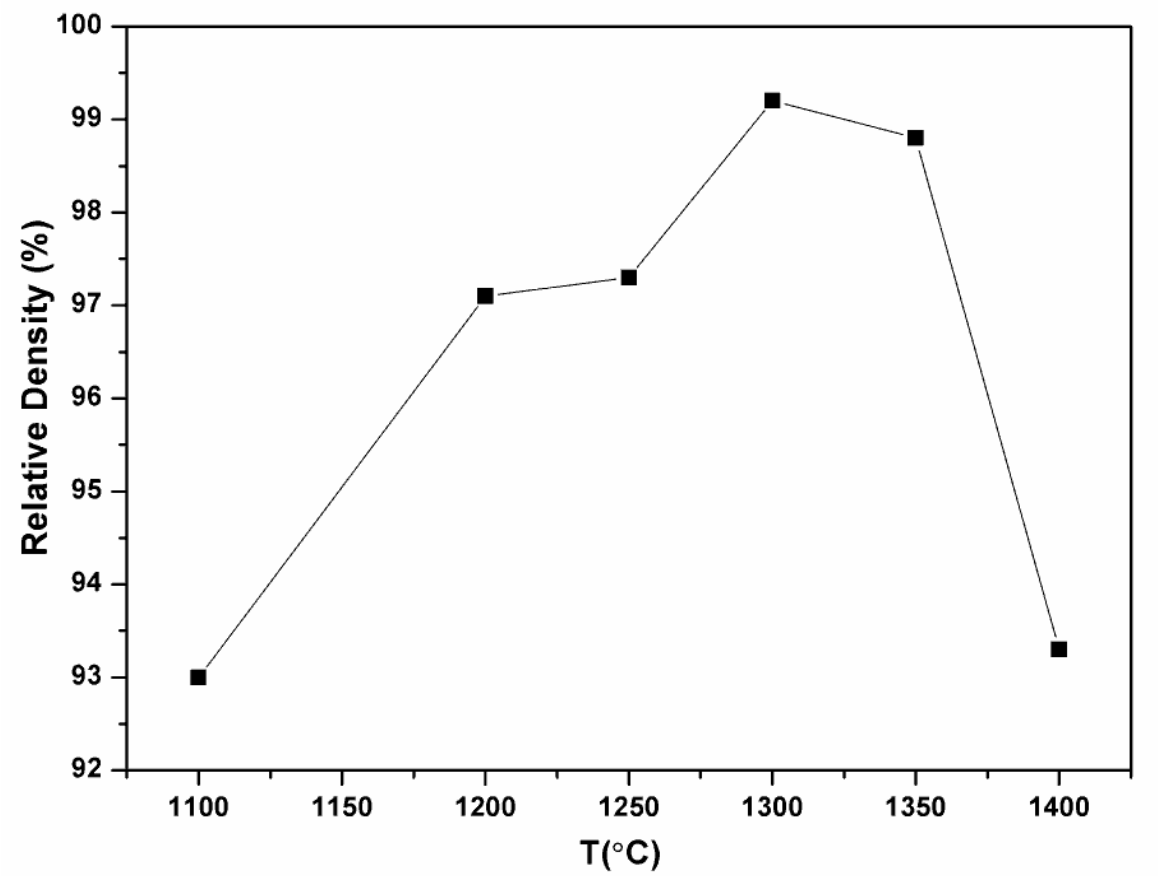

Fig. 4.3.3. Relative density plot of PTO ceramics sintered by SPS at different temperatures under a pressure of 50 MPa for 5mins.

SEM images of polished PTO ceramics sintered at 1100 ℃, 1200 ℃, 1250 ℃, 1300 ℃ and 1350 ℃ are shown in Fig.4.3.4. Obviously, the sample sintered at 1100 ℃ is not fully sintered and very porous which is consistent with the density result. The grain shape and size is still like the original powder. At 1200 ℃ and 1250 ℃, the ceramics are well sintered and dense. The grain size is smaller than 2um and the shape of some of the grains is not plate-like. The grain size increased significantly from 1250 ℃ to 1300 ℃, and at the same time the grains became plate like.

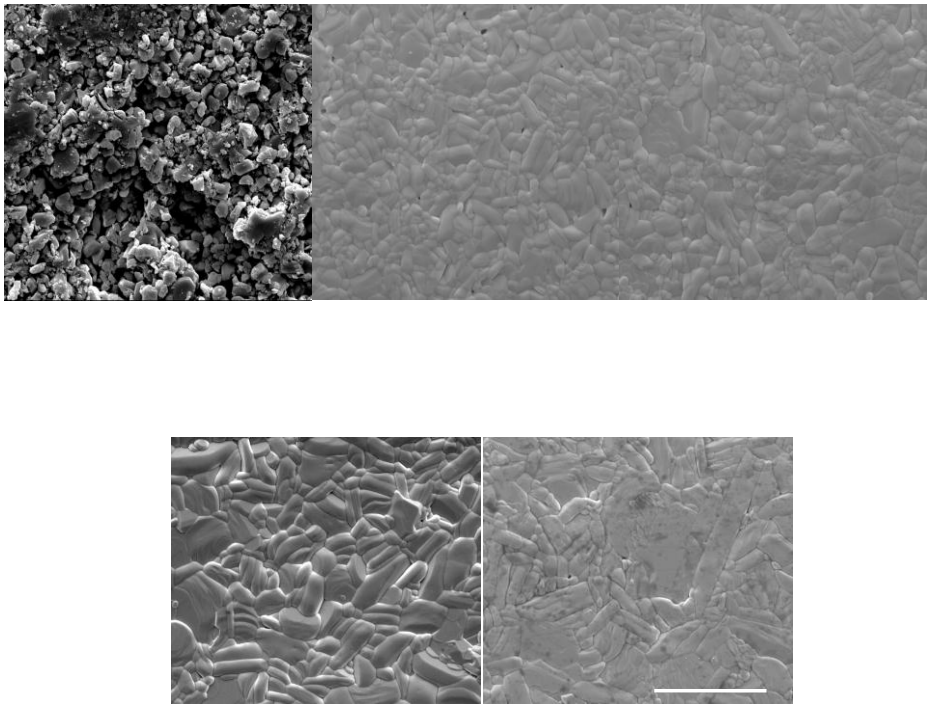

Fig.4.3.4. SEM images of PTO untextured ceramics sintered at 1100 ℃, 1200 ℃, 1250 ℃, 1300 ℃ and 1350 ℃.

Fig.4.3.5 shows the SEM pictures of the polished surfaces of the textured PTO viewed perpendicular (⊥) and parallel (//) to the SPS pressing direction. The grains prefer to grow along the direction perpendicular to the pressing direction during the texturing process which is consistent with the XRD results. Compared to untextured ceramic, the XRD patterns of the textured sample from a parallel (//) surface exhibit intense (h00) reflection (Fig.4.3.1). This indicates that the sintered ceramic samples were highly textured. The degree of grain orientation was measured by the Lotgering orientation factor f from the XRD peak intensities I (Section 3.3.2). The Lotgering factor f for textured PTO sample was 0.87 for planes parallel (//) to the SPS pressing direction, much higher than that of the untextured one-step sintered sample (0.53).

Generally, the plate-like grains are about 1 um in thickness and 2-5 um in the other two dimensions. Spontaneous polarization (Ps) is along the c-axis, which is perpendicular to the SPS pressing direction. So, the ferroelectric properties are expected to be better in the perpendicular direction.

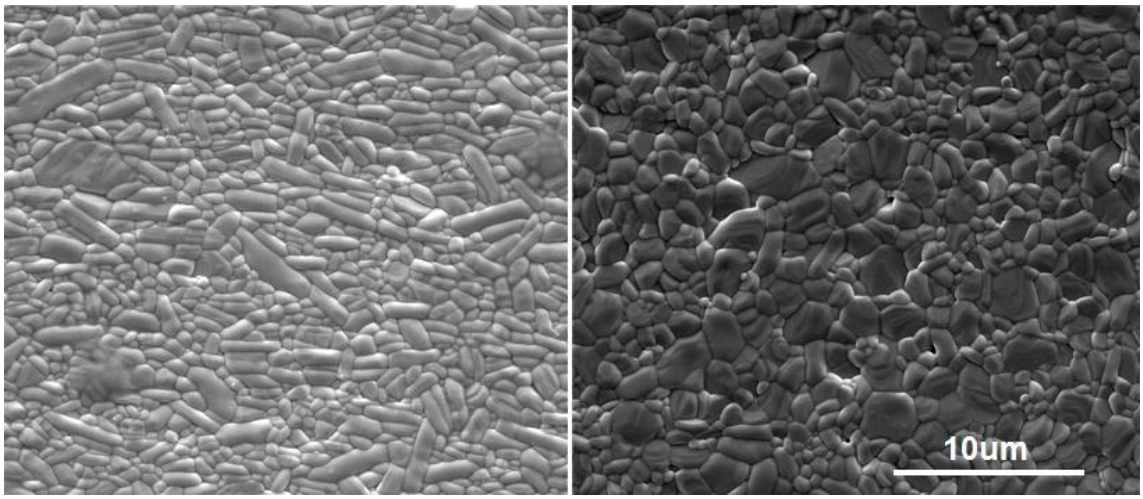

Fig.4.3.5. Textured PTO ceramic surfaces of (a) perpendicular direction (⊥) and (b) parallel direction (//).

The piezoelectric constant d_{33} was measured by poling the samples in silicone oil at 200 ℃ under various DC electric fields (15-35 kV/mm). The thickness of the samples used for poling was between 0.1mm and 0.3mm. For textured PTO ceramics, the piezoelectric constant d_{33} was 0.5 ± 0.1pC/N for SPS (⊥) and 0 ± 0.1pC/N for SPS (//), respectively. For untextured ceramics the d_{33} was zero. Fig.4.3.6 shows the thermal depoling data of two poled samples of textured PTO. The value is very stable until sample softening (~1580 ℃). The stability of the d_{33} proves the Curie point of PTO is higher than 1580 ℃. The Curie point is reported in the literature as 1750 ℃.[9]

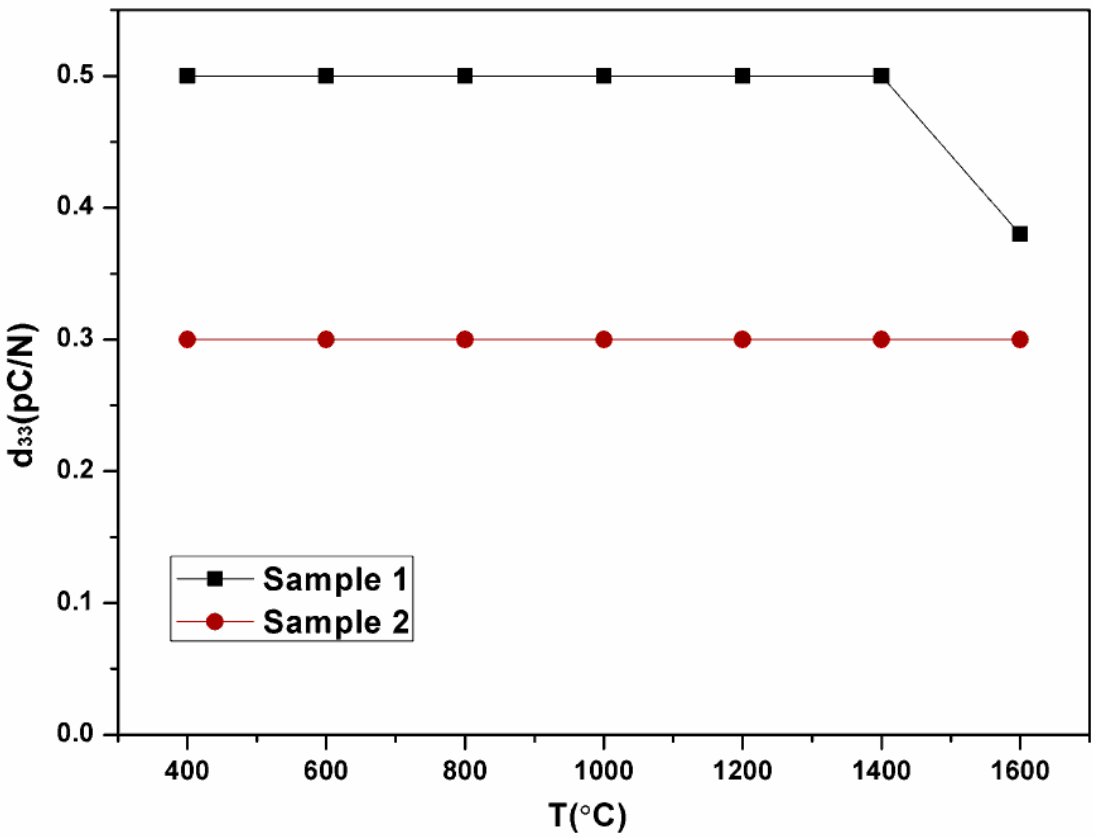

Fig.4.3.6. Thermal depoling of textured poled PTO ceramics.

Fig.4.3.7 shows the frequency dependence of dielectric constant and loss of the samples sintered at different temperatures. The dielectric constants increase with grain size, which increases with the sintering temperatures. This can be explained by the decreasing effect of the grain boundaries, which are non-ferroelectric layers ("dead" layer) with a low dielectric permittivity.[10]

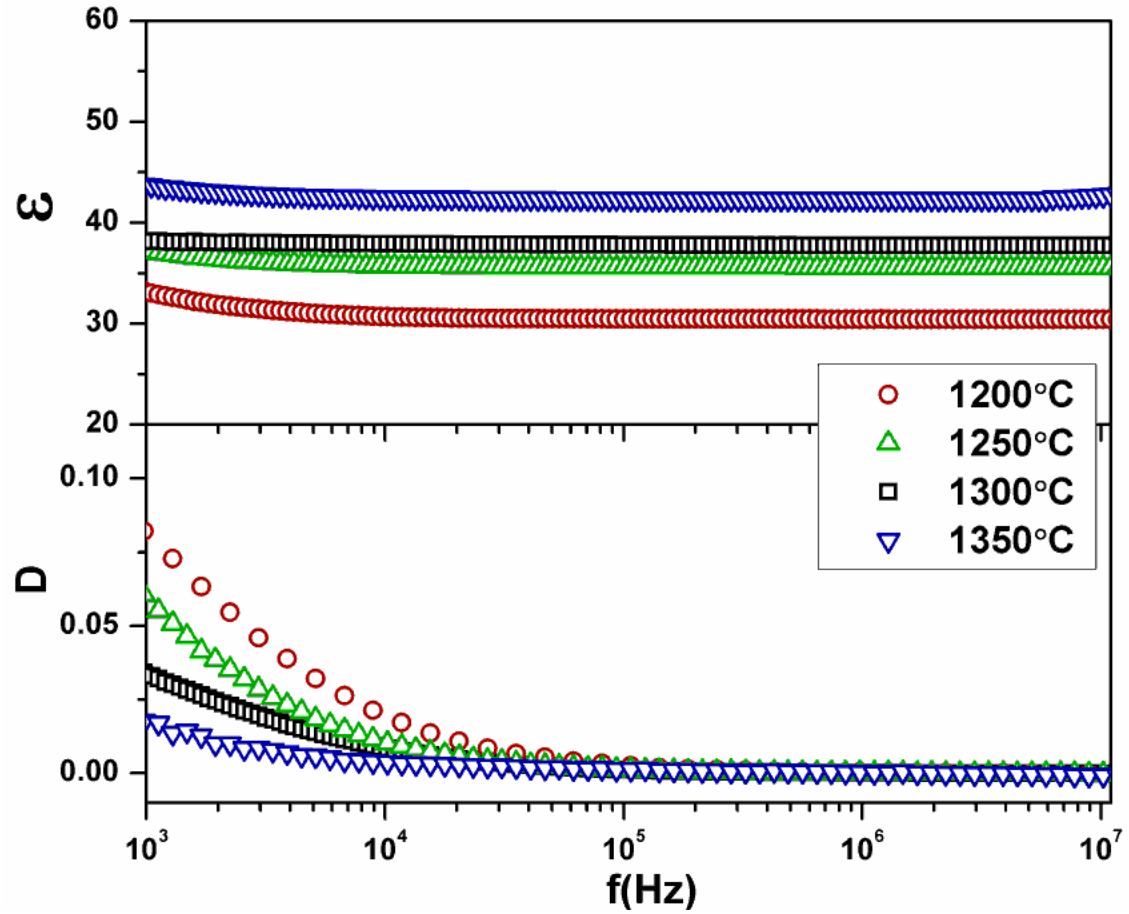

Fig.4.3.7. The frequency dependence of dielectric constant and loss of the untextured PTO samples sintered at different temperatures.

Fig.4.3.8 shows the frequency dependence of dielectric constant and loss of textured PTO measured at room temperature. The loss decreases with increasing frequency from 10^4Hz to 10^7Hz. The dielectric constant and loss of SPS (//) samples are lower than those of SPS ($\perp$) samples as expected. The dielectric constant is almost frequency independent. Though there is no report of the dielectric constant of single crystal PTO, the results are consistent with the data for single crystal LTO [4,5,11], with the same structure, ie, the dielectric constant along the Ps direction is higher than the other directions.

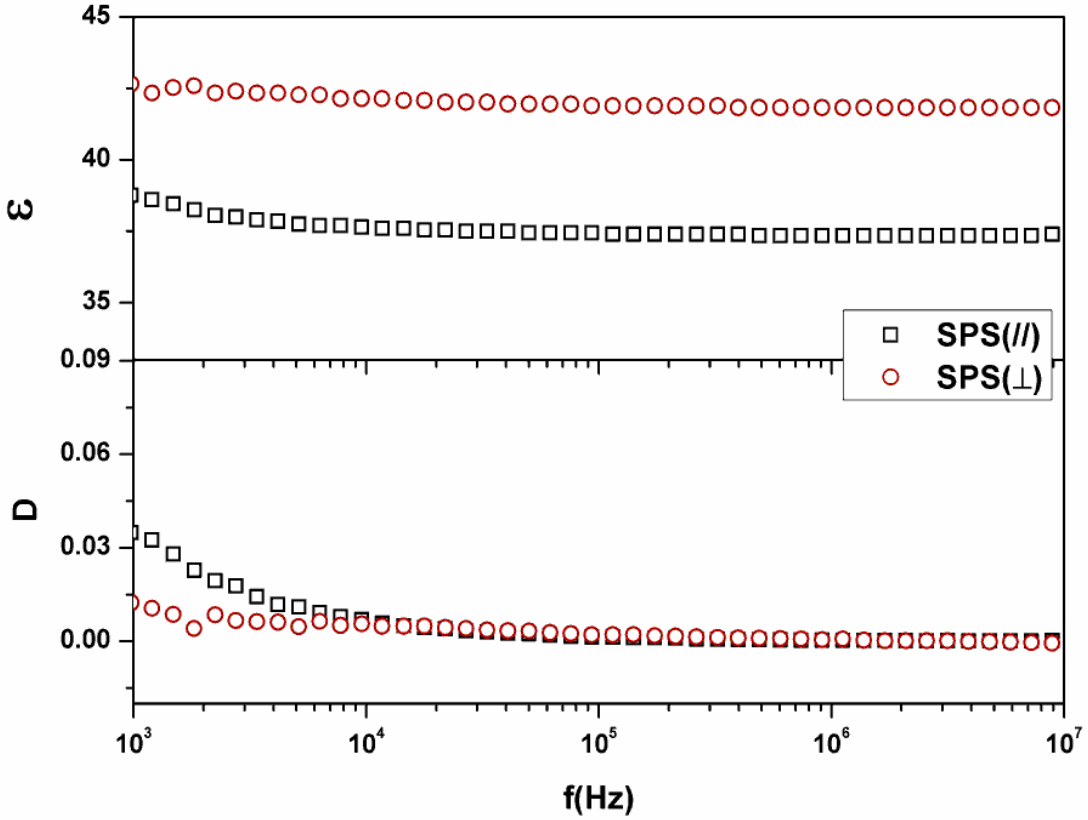

Fig.4.3.8. The frequency dependence of dielectric constant and loss of textured PTO measured at room temperature.

Fig.4.3.9 show the temperature dependence of dielectric constant and loss of textured PTO measured at three different frequencies of 100, 500 and 1000kHz. The dielectric constants and loss of PTO textured ceramic are greater along a direction perpendicular, (⊥), rather than parallel, (//), to the pressing direction. As discussed above, the parallel direction (//) is perpendicular to the c-axis, Ps, direction. This is consistent with the frequency dependent dielectric constant data.

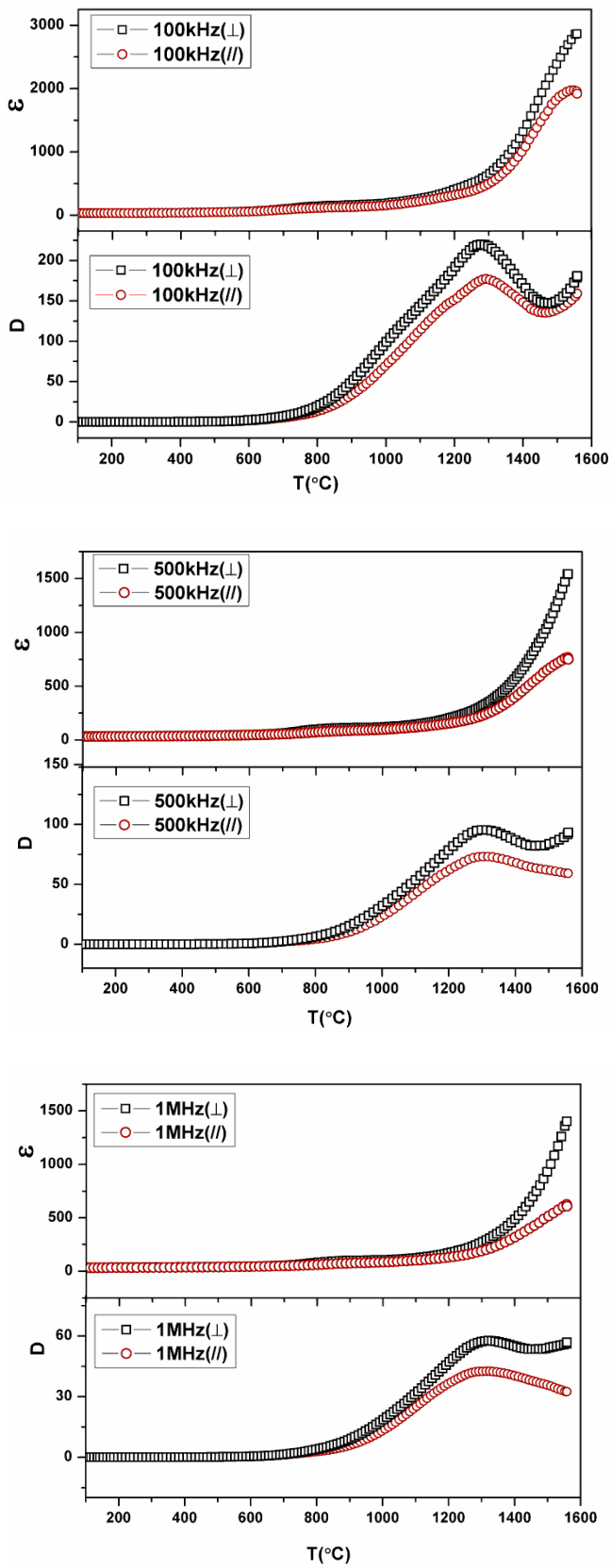

Fig.4.3.9. The temperature dependence of dielectric constant and loss of textured PTO measured at three different frequencies of 100kHz, 500kHz and 1000kHz.

Fig.4.3.10 shows the temperature dependence of dielectric constant and loss from 400 ℃ to 1200 ℃. There is a peak about 750 ℃, which shifts to a higher temperature with increasing frequency. This indicates the peak is due to point defects rather Curie point which would not shift with frequency. At even higher temperatures, the dielectric constant increases sharply on approaching the Curie point. The dielectric constant peak associated with the Curie point was not observed due to the temperature limitation of the furnace (1560 ℃) (Fig.4.9).

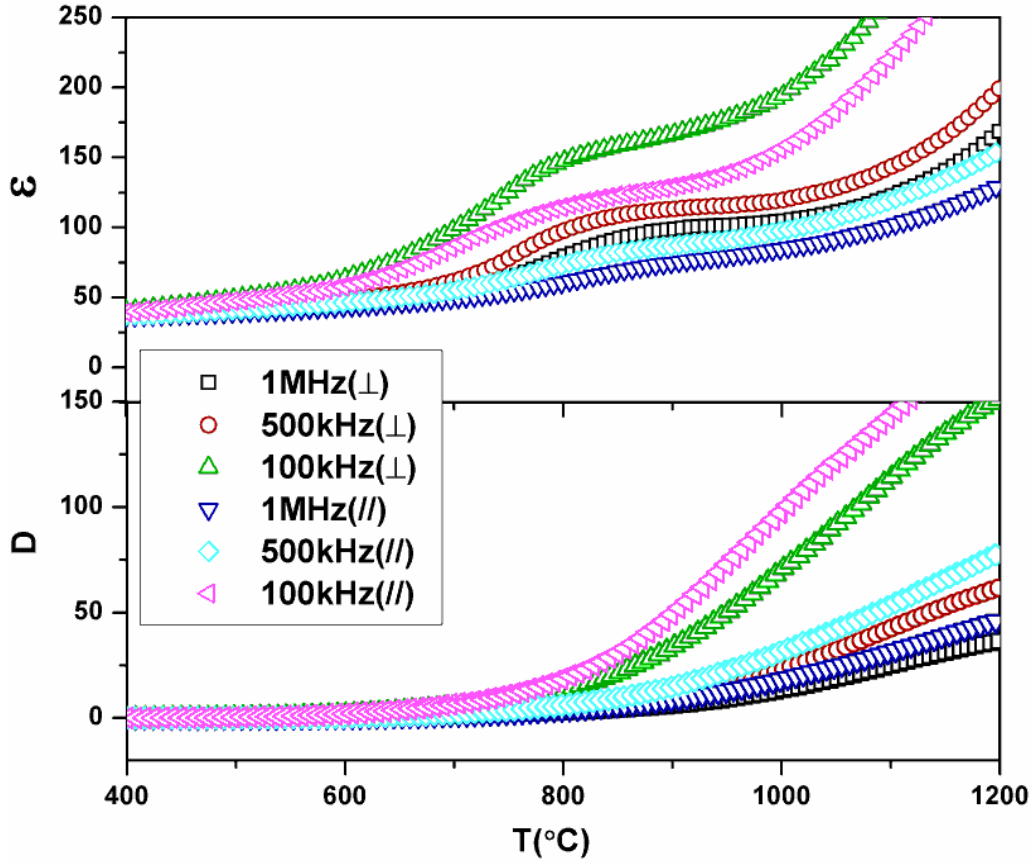

Fig.4.3.10. Dielectric constant and loss from 400 ℃ to 1200 ℃ at different frequencies.

Fig.4.3.11 shows the the DC resistivity of the textured PTO samples. The resistivity of PTO in both directions is about $10^6\Omega\cdot$cm at 600°C, which makes it a potential material

for high-temperature applications. The insert shows the Arrhenius relation between resisitivity and temperature which is $\rho = A\exp(\frac{-Ea}{kT})$ where Ea is the activation energy of the current carrier, A is a constant, ρ is resisitivity and k is Boltzmann constant. For SPS (⊥) and SPS (//) samples, the activation energies are 0.93 ± 0.01eV and 0.96 ± 0.01eV respectively. However, the band gap of PTO is about 2.99eV based on the calculation.[12] The intrinsic activation energy should be the half of band gap. The experimental value of the activation energy of PTO is much smaller than this. This suggests that the electrical conductivity is also due to the point defects.

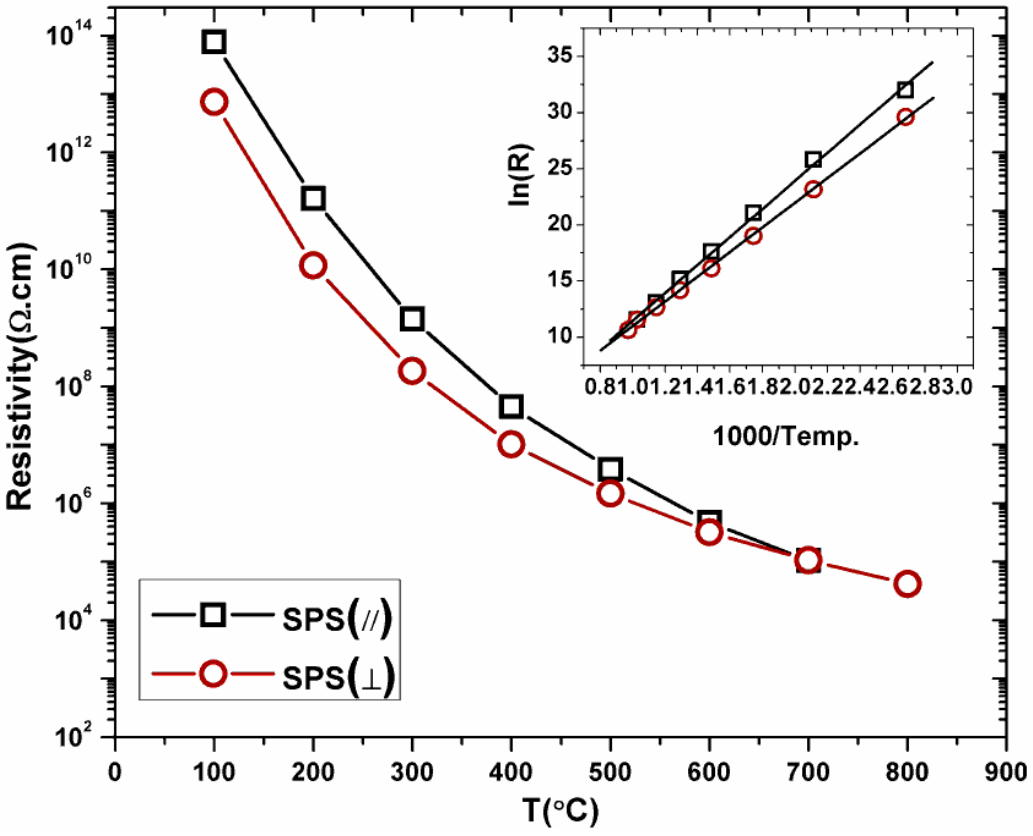

Fig.4.3.11. The DC resistivity of the textured PTO samples.

4.4. Conclusion

Single phase, dense and textured PTO ceramics were prepared. The lotgering orientation factor for a textured ceramic was 0.87. The Curie point is greater than 1560 ℃. PTO was shown for the first time to be ferroelectric because it showed piezoelectric activity after poling. The piezoelectric constant d_{33} was measured as 0.5 ± 0.1pC/N.

References

(1). Nanamatsu, S., Kimura, M., Doi, K., and Takahashi, M., *Journal of the Physical Society of Japan*, 1971. **30**: p. 300-301.

(2). Takahash.M, Nanamats.S, and Kimura, M., *Journal of Crystal Growth*, 1971. **13**: p. 681.

(3). Ning, H., Yan, H., and Reece, M., *Journal of the American Ceramic Society*, 2010. **93**(5): p. 1409-1413.

(4). Kimura, M., Matsushi, S., Nanamats, S., Takahash, M., and Doi, K., *Japanese Journal of Applied Physics,* 1972. **11**: p. 904-907.

(5). Yan, H., Ning, H., Kan, Y., Wang, P., and Reece, M., *Journal of the American Ceramic Society*, 2009. **92**(10): p. 2270-2275

(6). Kimura, M., Nanamatsu, S., Kawamura, T., and Matsushita, S., *Japanese Journal of Applied Physics*, 1974. **13**: p. 1473-1474.

(7). Kozmin, P. A., Zakharov, N. A., and Surazhskaya, M. D., *Journal of Inorganic Materials*, 1997. **33**: p. 850-852.

(8). Titov, Y.A., A.P. Leonov, A.M. Sych, S.Y. Stefanovich, V.V. Lashneva, and Y.N. Venevtsev, *Inorganic Materials*, 1985. **21**(10): p. 1515-1519.

(9). Sych, A., Titov, Y., and Nedilko, S., *Zhurnal Neorganicheskoi Khimii,* 1980. **25**: p. 2056-2061.

(10). Frey, M. H., Xu, Z., Han, P., and Payne, D., *Ferroelectrics*, 1998. **206**: p. 337-353.

(11). Nanamatsu, S., M. Kimura, and N. Yamada, *Nec Research and Development*, 1974. **34**: p. 39-42.

(12). Bruyer, E. and A. Sayede, *Journal of Applied Physics*, 2010. **108**(5): p. 053705.

Chapter V. Results - $La_{2-x}Ce_xTi_2O_7$ solid solution system

5.1. Introduction

Of the PLS ceramics, $La_2Ti_2O_7$ (LTO) is the most promising for high temperature piezoelectric applications because of its high Curie point (1461 ℃) and useful piezoelectric activity.[1] Cerium has similar properties to lanthanum. In Aurivillius phase $CaBi_4Ti_4O_{15}$, Ce doping has been reported to increase the high temperature electrical resistivity and piezoelectric constant d_{33}.[2] In some other Aurivillius materials, such as $Na_{0.25}K_{0.25}Bi_{2.5}Nb_2O_9$, cerium doping can increase the Curie point.[3] Also, for $Na_{0.5}Bi_{0.5}TiO_3$-$BaTiO_3$, Ce doping increased the dielectric constant at room temperature and the depolarization temperature (Td).[4] However, there is no reported research on Ce substituted PLS ferroelectric materials. In the current work, single phase, dense and textured $La_{2-x}Ce_xTi_2O_7$ (x=0.15, 0.25, 0.35) ceramics were prepared and their properties were characterized.

5.2. Experimental Details

The $La_{2-x}Ce_xTi_2O_7$ (x=0.15, 0.25, 0.35, 0.5) compositions (LCTO15, LCTO25, LCTO35, LCTO50) were obtained by the mixed oxide route. La_2O_3 (99.99%), CeO_2 (99.9%) and TiO_2 (99.9%) were used as the starting materials. The powders were milled and then the powders were calcinated in air for 4h at 1300 ℃. The powders were re-milled for 4 h to break any agglomerates and reduce the particle size. The ball milling speed was always 350 rpm.

The synthesized powders were sintered in a SPS. A heating rate of 100 ℃/min was used in all cases. The untextured ceramics used for dielectric tests and Tc measurement were sintered at 1400 ℃ under a pressure 80 MPa for 5min.

The textured ceramic samples used for piezoelectric constant measurement (d_{33}) were textured using a two-step sintering method. First, the LCTO15, LCTO25, LCTO35 powders were pressed in a 20-mm-diameter graphite die and sintered at 1200 ℃ under a pressure of 80 MPa for 3 min. After this stage, all these samples had relatively high density (>95%), but the grain size was only slightly larger than that of the starting powder. In the second step, the samples were placed in a larger die of 30 mm diameter and sintered at 1400 ℃ under a pressure of 80MPa for 5min. The sintered disks were then heat treated in air at 1400 ℃ for 20h to anneal and increase grain growth.

5.3. Results and Discussion

Fig.5.3.1 shows the XRD patterns of the LCTO15, LCTO25, LCTO35 and LCTO50 powders. The diffraction peaks of LCTO15, LCTO25 and LCTO35 match the indexed peaks for the LTO (XRD PDF card: 028-0517) structure parameters, which means the materials are single phase within the sensitivity of the technique. For LCTO50 there are several XRD peaks that do not match the indexed peaks for LTO, which indicates the solid solution limit for Ce in $La_{2-x}Ce_xTi_2O_7$ is less than x=0.5. The impurity is a mixture of Ce_2O_3 and La_2TiO_5.

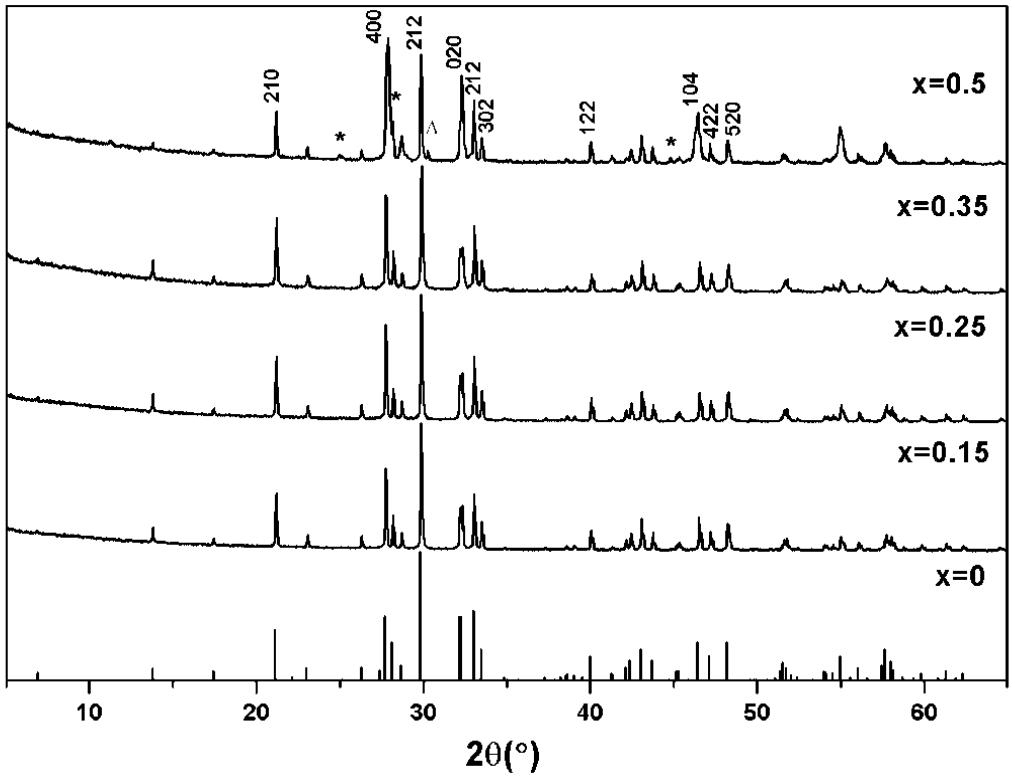

Fig.5.3.1. X-ray diffraction patterns of LCTO15, LCTO25, LCTO35 and LCTO50 powders matching indexed peaks for LTO (XRD PDF card: 00-028-0517). The peaks of Ce_2O_3 and La_2TiO_5 are marked by a "*".

Fig.5.3.2 shows the change of lattice parameters with increasing Ce substitution determined using the XRD data. The a-, b- and c- dimensions decrease with increasing Ce. This indicates the substituted Ce entered in the lattice. All of the compounds have the same structure as LTO, which is monoclinic with space group $P2_1$ at room temperature, and the structure changes into a paraelectric, centro-symmetric structure (Cmcm) at the Curie point.[5,6] The spontaneous polarization is along the c-axis.

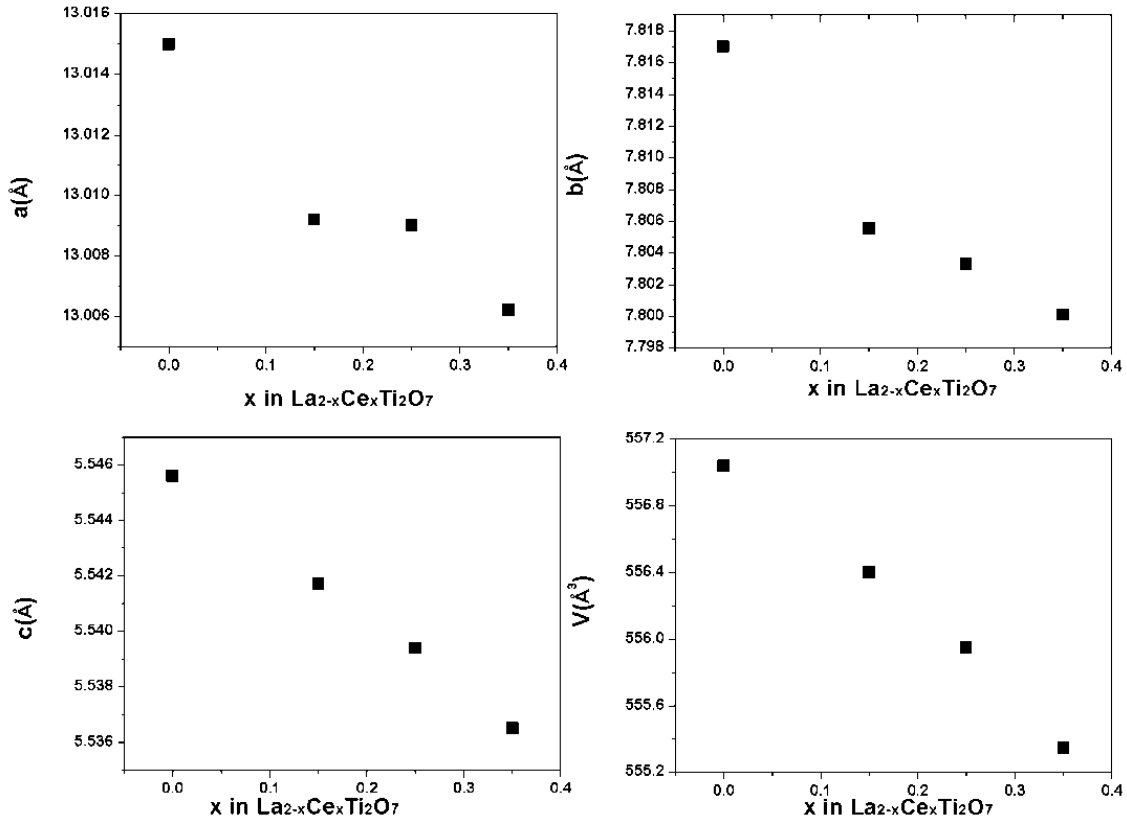

Fig.5.3.2. The lattice parameters of $La_{2-x}Ce_xTi_2O_7$ as a function of Ce content. The data for LTO (x=0) is from the literatures.[6,7]

Fig.5.3.3(a-d) show the XPS peaks for the La 3d, Ce 3d, Ti 2p, and O 1s electron binding energies (BE) of the powder samples. Fig.5.3.3(a) shows the La 3d states. The La $3d_{5/2}$ and La $3d_{3/2}$ components show a clear doublet structure for the LCTO15, LCTO25

and LCTO35 samples. The BE splitting between the components of both La $3d_{5/2}$ and La $3d_{3/2}$ lines is about 4.1 eV. This effect might be due to the interaction between bonding and antibonding states.[8] Comparing these peak positions with the literature data, the La^{3+} state is stable in these materials.[8] The peaks of Ce 3d were compared to reference data for Ce^{3+} and Ce^{4+} compounds (Fig.5.3.3b). The $3d_{5/2}$ and $3d_{3/2}$ of Ce^{3+} are split which is also due to the interaction between bonding and antibonding states. Some Ce^{4+} exists in these materials indicated by the peak at 916.5 eV (*).[9,10] For LCTO15, Ce^{4+} is hardly observed, however, with increasing Ce content, Ce^{4+} increases for LCTO25 and LCTO35. The Ti 2p peaks are shown in Fig.5.3.3(c). Compared with the literatures, the Ti^{4+} state is stable and does not change with increasing Ce content.[8] Fig.5.3.3(d) shows the peaks for the O 1s state. Two components, A and B, could be identified from the O1s spectra deconvolution. Component A is at 529.7 eV and component B is at 531.7 eV. Compared to the literature, component A is the O^{2-} in the PLS structure and B with higher BE corresponds to the oxygen connecting Ce^{3+} or point defects.[8,11-13]

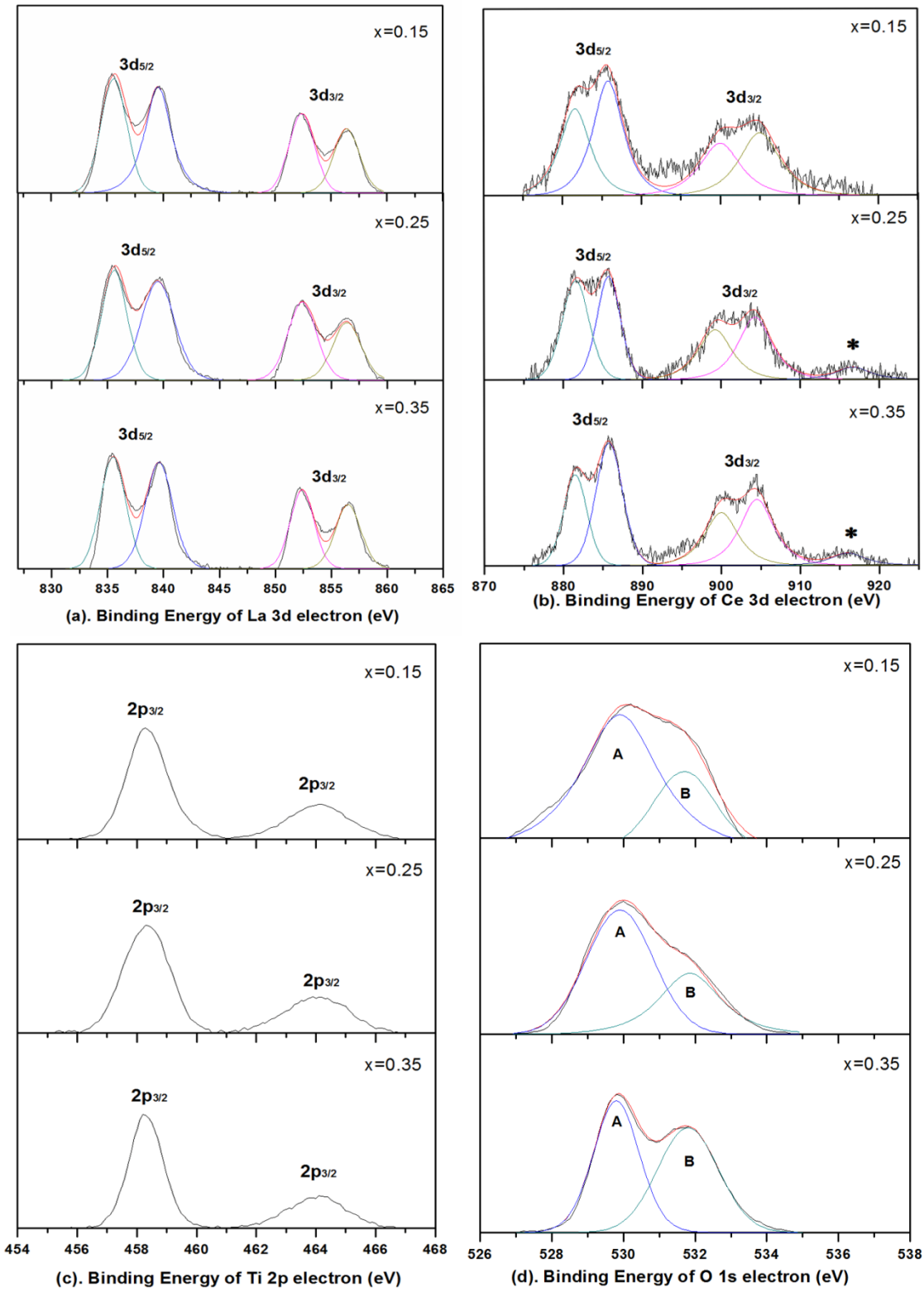

Fig.5.3.3 The X-ray photoelectrons spectroscopy (XPS) peaks of LCTO powder samples for: (a) La 3d; (b) Ce 3d; (c) Ti 2p; and (d) O 1s.

Fig.5.3.4 shows the XRD patterns of textured LCTO15, LCTO25, LCTO35 ceramics. The XRD patterns from a plane with its normal direction parallel to the SPS pressing direction exhibit intense (h00) reflections, which indicates that the ceramics are textured. The Lotgering orientation factor, f, was used to estimate the degree of grain orientation. The Lotgering factor f of LCTO15, LCTO25, LCTO35 were calculated as 0.71, 0.71, 0.74 respectively for the parallel direction (//).

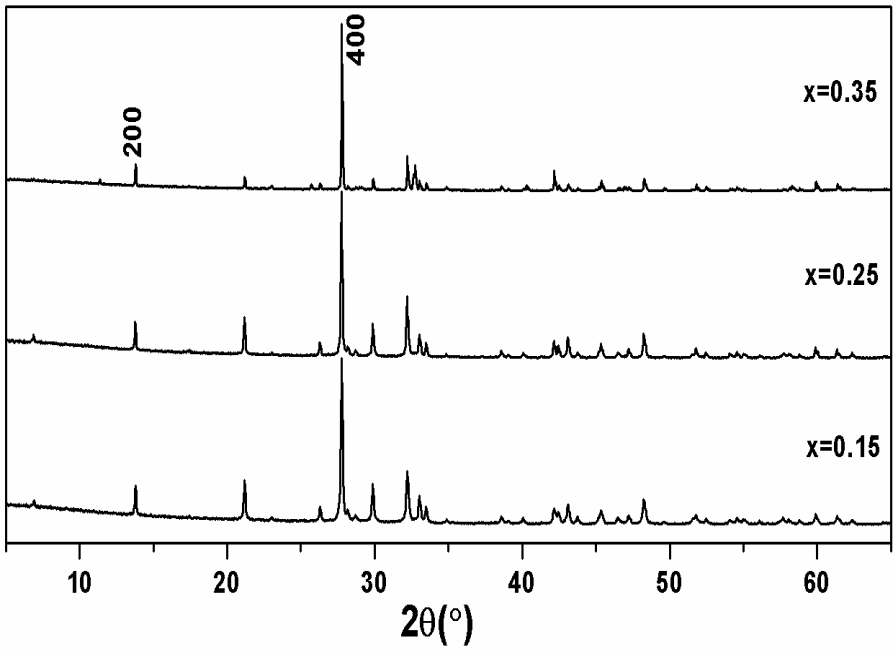

Fig.5.3.4. XRD patterns of textured LCTO ceramics on parallel direction (//).

Fig.5.3.5 shows the SEM micrographs of the polished surfaces of the textured LCTO15, LCTO25 and LCTO35 ceramics viewed perpendicular (⊥) to the SPS pressing direction. The grains prefer to grow along directions perpendicular to the pressing direction. Compared to pure LTO ceramic,[1] the grains become less plate-like due to Ce substitution which explains their lower lotgering orientation factor compared to LTO (0.80). On average, the plate-like grains are about 1.5um in thickness and 5um in the

other two dimensions for all of the ceramics.

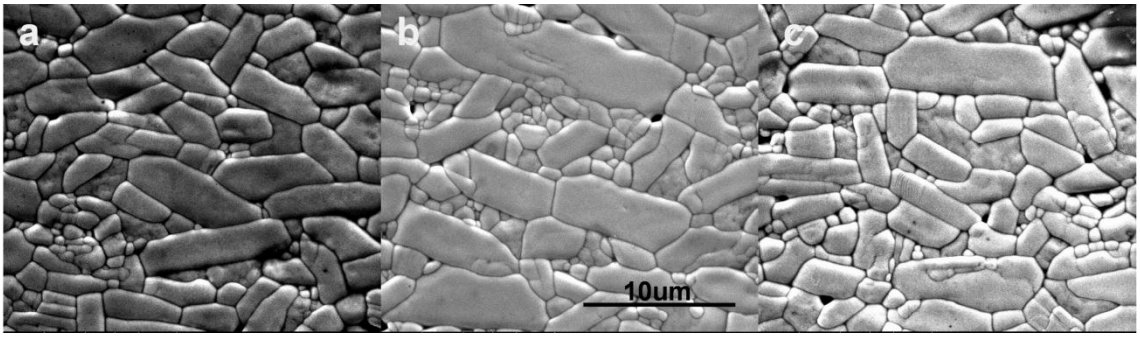

Fig.5.3.5. SEM images of the polished surface viewed perpendicular to the pressing direction (⊥) of the (a) LCTO15; (b) LCTO25 and (c) LCTO35 ceramics.

Fig.5.3.6(a-c) show the temperature dependence of the dielectric permittivity (ε) and loss (D) of LCTO15, LCTO25, LCTO35 untextured samples, respectively, measured at two different frequencies, 500 kHz and 1000 kHz. From these figures, the Tc of LCTO15, LCTO25 and LCTO35, are 1440±5 ℃, 1435±5 ℃, and 1387±5 ℃, respectively. The Tc of LTO has previously been reported as 1461±5 ℃.[1] With increasing Ce substitution, the Tc decreases gradually. This might be explained by the substituted Ce, which has a smaller ionic size and higher electronegativity compared to La. The insert figs show the temperature dependent loss measured at 100 kHz, 10 kHz and 1 kHz. Frequency dependence broad peaks could be observed at the temperature range 400 – 800 ℃ suggesting there is a high concentration of point defect in the materials. There are loss peaks just below the Curie point, which are attributed to domain wall movement.

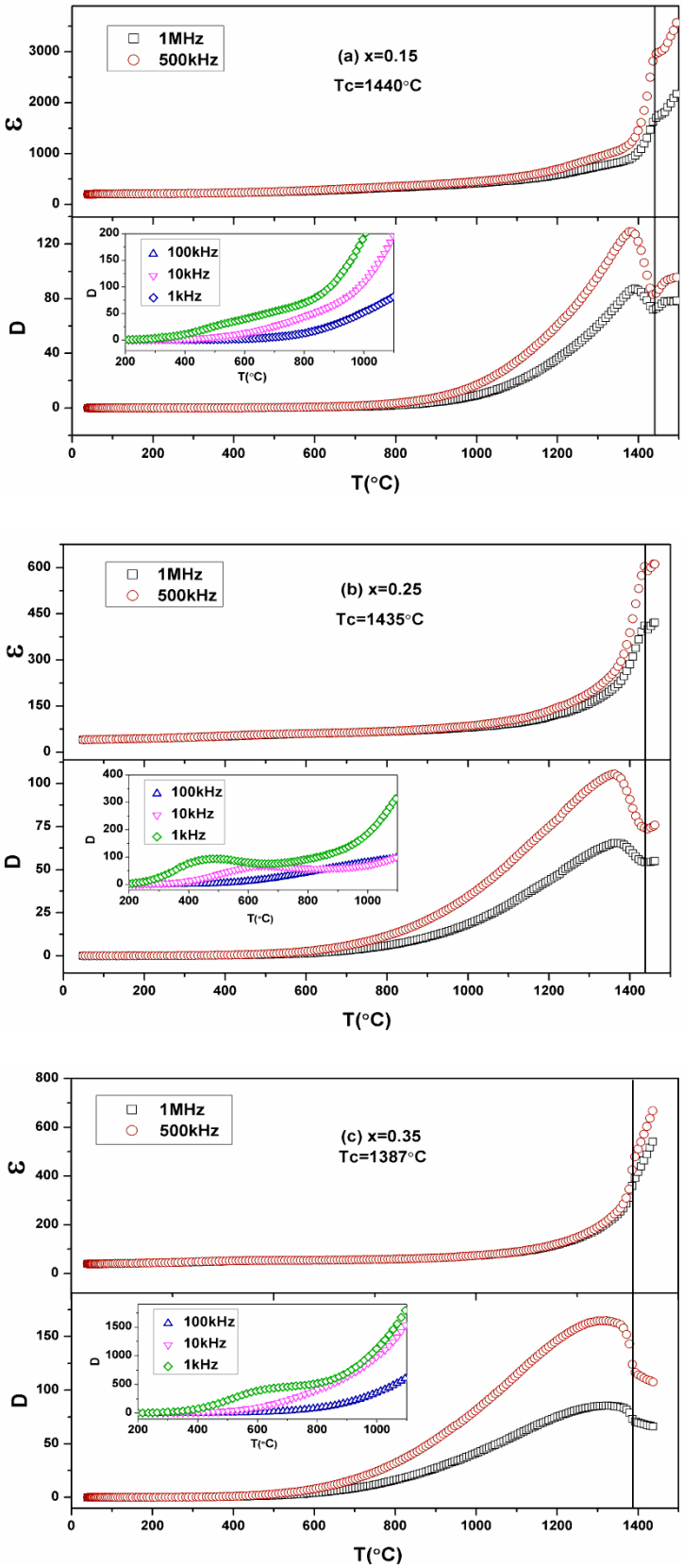

Fig.5.3.6. Temperature dependence of the dielectric constant and loss of LCTO untextured ceramics at different frequencies of 1MHz and 500 kHz. The insert figs are the data for temperature dependence loss measured at 100 kHz, 10 kHz and 1 kHz.

Fig.5.3.7 shows the frequency dependence of relative dielectric permittivity and loss of LCTO15, LCTO25 and LCTO35 untextured ceramics measured at room temperature compared with the data for LTO.[1] The loss decreases with increasing frequency. In the lower frequency range (10^3Hz to 10^5Hz), the loss increases with increasing Ce substitution, from LTO to LCTO35. In the higher frequency range (10^5Hz to 10^7Hz) they are similar and low. This behavior may have been produced by the presence of the defect dipoles.[14] This result is consistent with the temperature dependent loss result. The defect dipoles can switch, contributing to the loss value in the low frequency range. However, at high frequency the defect dipole cannot follow the electric field change, so the loss decreases to a small value. This behavior is also apparent in the permittivity change, which shows increasing apparent permittivity with decreasing frequency. In comparison, the permittivity of LTO is constant in the whole frequency range. Permittivity increases with increasing amount of Ce substitution. This might be explained by the Ce in the lattice, which changed the intrinsic dielectric property.

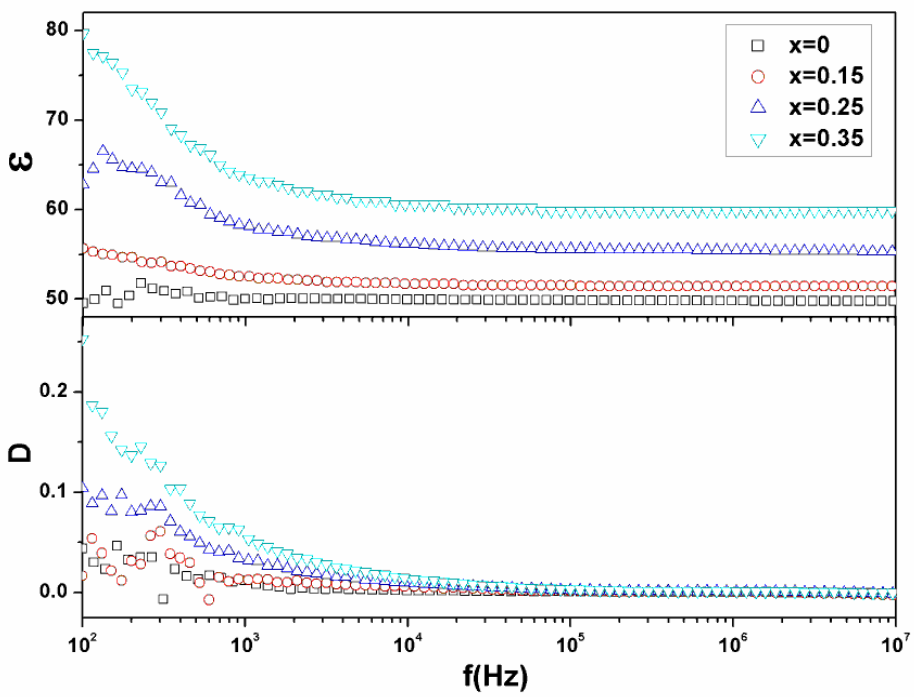

Fig.5.3.7. Frequency dependence of dielectric constant and loss of untextured ceramics of LTO,[1] LCTO15, LCTO25, and LCTO35.

The DC resistivity of the LTO,[1] LTCO15, LTCO25, LTCO35 untextured ceramics are shown in Fig.5.3.8. Compared to the LTO ceramic, the resistivity of these compounds decreases with increasing Ce substitution. The insert in Fig.8 shows the Arrhenius relation between resistivity and temperature. For LTO, LCTO15, LTCO25 and LTCO35 ceramics, the activation energies are 1.34, 0.56, 0.53 and 0.52eV. The band gap of $La_2Ti_2O_7$ is reported as 2.8-3.2eV.[15] The activation energy for LTO is about half of the band gap which indicates the DC conductivity is dominated by intrinsic charge carriers. Compared to this, the activation energies of LCTO15, LCTO25 and LCTO35 are much lower. This suggests that the DC conductivities of LCTO15, LCTO25 and LCTO35 are dominated by extrinsic charge carriers produced by the donor dopant and leads to semiconductive behavior (n-type).[16,17] This is consistent with the results of XPS.

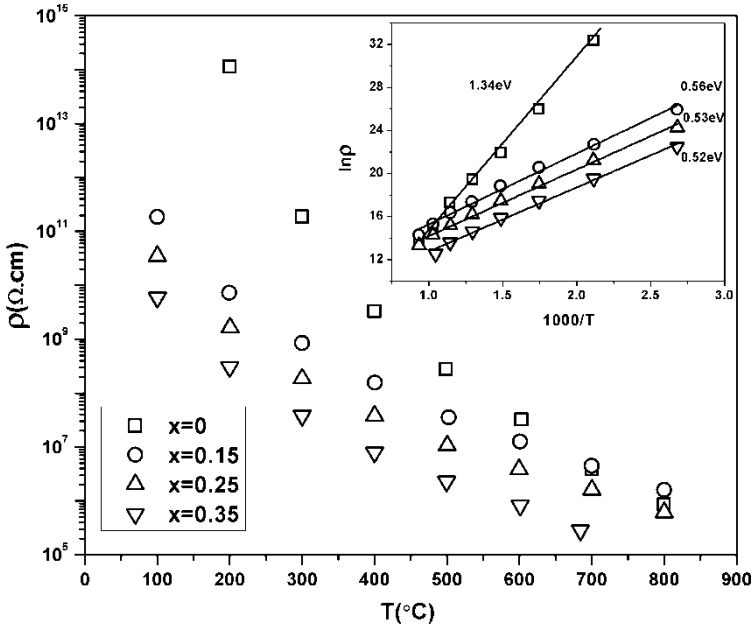

Fig.5.3.8. Direct-current electric resistivity of LTO,[8] LCTO15, LCTO25 and LCTO35 ceramics. The insert is the Arrhenius relation between resistivity and temperature.

The piezoelectric constant d_{33} was measured in the direction perpendicular to pressing direction (Fig.5.3.9). The textured samples were poled in silicone oil at 120 ℃ under various DC electric fields. The highest electric fields that could be achieved during poling were 19kV/mm, 19kV/mm and 16kV/mm for LCTO15, LCTO25 and LCTO35 respectively. The x=0.15 composition showed an increased d_{33} (LCTO15, 3.9 ± 0.1pC/N) compared to LTO (2.6 ± 0.1pC/N) poled at 20kV, 220 ℃, which has even higher density (>98%) and Lotgering orientation factor (f=0.80). With further increasing Ce substitution, the d_{33} decreased from LCTO15 to LCTO35. This is because the defect concentration increases and resistivity decreases with increasing Ce substitution, leading to a reduction in the maximum poling field that could be applied.

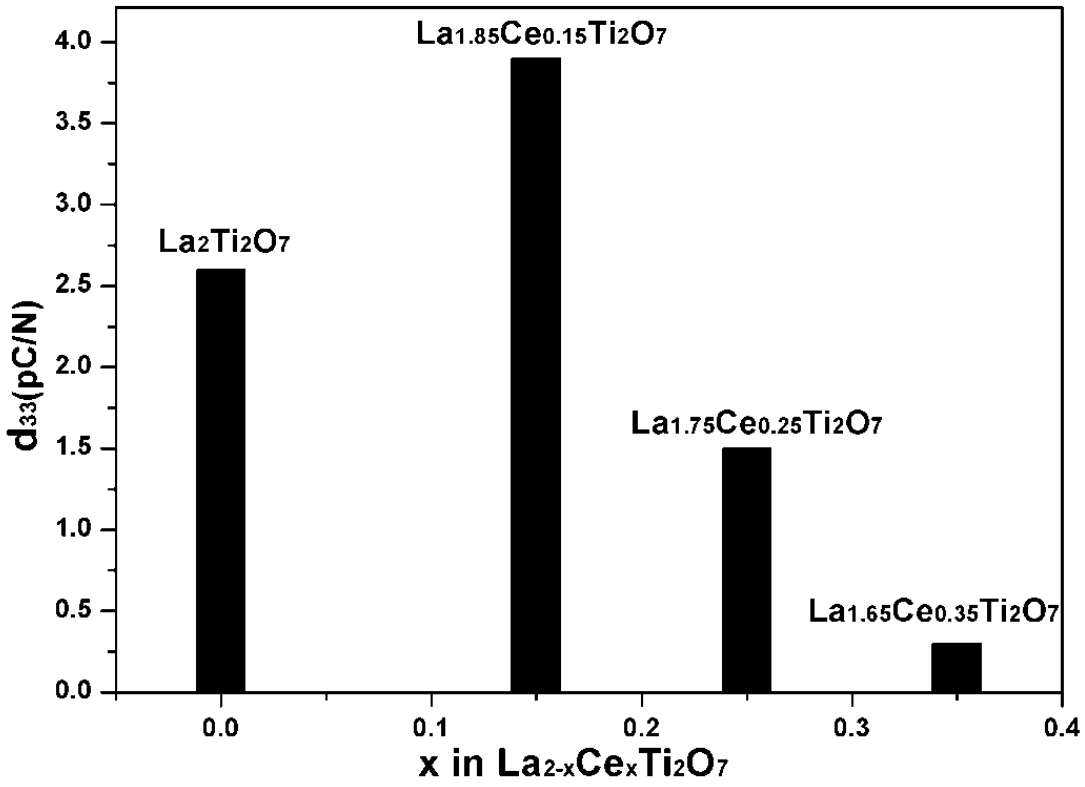

Fig.5.3.9. Piezoelectric constant (d_{33}) of the textured ceramics measured perpendicular to the pressing direction ($\perp$). The data for LTO is from ref.[1].

5.4. Conclusion

Single phase, dense $La_{2-x}Ce_xTi_2O_7$(x=0, 0.15, 0.25, 0.35) ceramics were prepared by spark plasma sintering. The limit of Ce substitution in $La_{2-x}Ce_xTi_2O_7$ was found to be between 0.35 to 0.50. The a-, b- and c-axes of the unit cell decrease with increasing Ce substitution, which indicates that Ce enters the lattice. The Curie point (Tc) of $La_{2-x}Ce_xTi_2O_7$ (x=0, 0.15, 0.25, 0.35) decrease and dielectric constant and loss increase with increasing amount of Ce substitution. Electrical resistivity decreases due to the extrinsic charge carriers produced by Ce substitution. The highest d_{33} was 3.9 ± 0.1pC/N for $La_{1.85}Ce_{0.15}Ti_2O_7$.

References

(1). Yan, H., Ning, H., Kan, Y., Wang, P., and Reece, M., *Journal of the American Ceramic Society*, 2009. **92**(10): p. 2270-2275

(2). Yan, H., Zhang, Z., Zhu, W., He, L., Yu, Y., Li, C., and Zhou, J., *Materials Research Bulletin*, 2004. **39**: p. 1237-1246.

(3). Gai, Z. G., Wang, J. F., and Wang, C. M., *Applied Physics Letters*, 2007. **90**: p. 052911 - 052911-3.

(4). Babu, J. B., He, M., Zhang, D. F., Chen, X. L., and Dhanasekaran, R., *Applied Physics Letters*, 2007. **90**: p. 102901.

(5). Nanamatsu, S., M. Kimura, and N. Yamada, *Nec Research and Development*, 1974. **34**: p. 39-42.

(6). Ishizawa, N., F. Marumo, S. Iwai, M. Kimura, and T. Kawamura, *Acta Crystallographica Section B-Structural Science*, 1982. **38**(FEB): p. 368-372.

(7). Nanamatsu, S., Kimura M., Doi, K., Matsushita, S., and Yamada, N. , A new Ferroelectric: $La_2Ti_2O_7$. *Ferroelectrics*, 1974. **8**: p. 511-513.

(8). Atuchin, V., Gavrilova, T., Grivel, J., and Kesler, V., *Journal of Physics D: Applied Physics*, 2009. **42**: p. 035305.

(9). Charvin, P., Abanades, S., Beche, E., Lemont, F., and Flamant, G., *Solid State Ionics*, 2009. **180**: p. 1003-1010.

(10). Beche, E., Charvin, P., Perarnau, D., Abanades, S., and Flamant, G., *Surface and Interface Analysis*, 2008. **40**: p. 264-267.

(11). Shah, L., Ali, B., Zhu, H., Wang, W., Song, Y., Zhang, H., Shah, S., and Xiao, J., *Journal of Physics: Condensed Matter*, 2009. **21**: p. 486004.

(12). Chu, M. W., Ganne, M., Caldes, M. T. and Brohan, L., *Journal of Applied Physics*, 2002. **91**: p. 3178-3187.

(13). Reddy, B. M., Chowdhury, B., and Smirniotis, P. G., *Applied Catalysis A: General*, 2001. **219**: p. 53-60.

(14). Park, S., and Han, Y., *Journal of the Korean Physical Society*, 2010. **57**: p. 458-463.

(15). Bruyer, E. and A. Sayede, *Journal of Applied Physics*, 2010. **108**(5): p. 053705.

(16). Jaiswal, N., Singh, N. K., Kumar, D., and Parkash, O., *Journal of Power Sources*, 2012. **202**: p. 78-84.

(17). Kudo, T., and Obayashi, H., *Journal of The Electrochemical Society*, 1976. **123**: p. 415-419.

Chapter VI. Results - $Nd_{2-x}Ce_xTi_2O_7$ solid solution system

6.1. Introduction

The ferroelectric activity of single crystal of $Nd_2Ti_2O_7$ (NTO) was confirmed for the first time in the 1970s.[1,2] $Nd_2Ti_2O_7$ has a PLS structure that is similar to $La_2Ti_2O_7$ (LTO).[1-4] At room temperature, it has a monoclinic structure with space group $P2_1$.[2,5] The ferroelectric phase changes into the paraelectric phase at 1481 ℃, which is higher than LTO (1461 ℃).[4,6] For single crystal NTO, the d_{33} was measured as 6.5 pC/N.[1] $Nd_2Ti_2O_7$ powder can be prepared by solid state calcination of the mixed oxide (Nd_2O_3 and TiO_2) and textured NTO ceramic was prepared using SPS.[6] The highest d_{33} was measured as 0.5 pC/N for textured ceramics.[6] As discussed in the last chapter, Ce can improve the piezoelectric constant in PLS ferroelectric materials. The $Nd_{2-x}Ce_xTi_2O_7$ solid solution system was prepared and the textured ceramics were densified for the first time. The ferroelectric properties were characterized and described in this chapter.

6.2. Experiment Details

The $Nd_{2-x}Ce_xTi_2O_7$ (x=0.05, 0.25, 0.5, 0.75) compositions (NCTO5, NCTO25, NCTO50, NCTO75) were obtained by the mixed oxide route. The powders were ball milled at 350rpm for 4 hours with ethanol as the milling medium and then calcinated for 4.5h at 1250 ℃. The powders were then re-milled at 350rpm for 4h to break any agglomerates and reduce the particle size.

The textured ceramics were obtained using a two-step sintering method. Heating rate of 100 ℃/min was used in all cases. First, the NCTO5, NCTO25, NCTO50, NCTO75 powder was pressed in a 20-mm-diameter graphite die and sintered at 1200 ℃ under a pressure of 80 MPa for 3 min. In the second step, the sample was placed in a larger die of 30 mm diameter and sintered at 1350 ℃ under a pressure of 80MPa for 5min. The sintered disks were then annealed in air at 1300 ℃ for 20h.

6.3. Results and Discussion

Fig.6.3.1 shows the XRD patterns of the NCTO5, NCTO25, NCTO50 and NCTO75 powders. The diffraction peaks of NCTO5, NCTO25 and NCTO50 match the indexed peaks for the NTO (PDF NO. : 00-033-942) well. For NCTO75 there are several XRD peaks that do not match the indexed peaks for NTO, which indicates that the solubility limit for Ce is less than x=0.75. The main second phase is $Nd_4Ti_9O_{24}$.

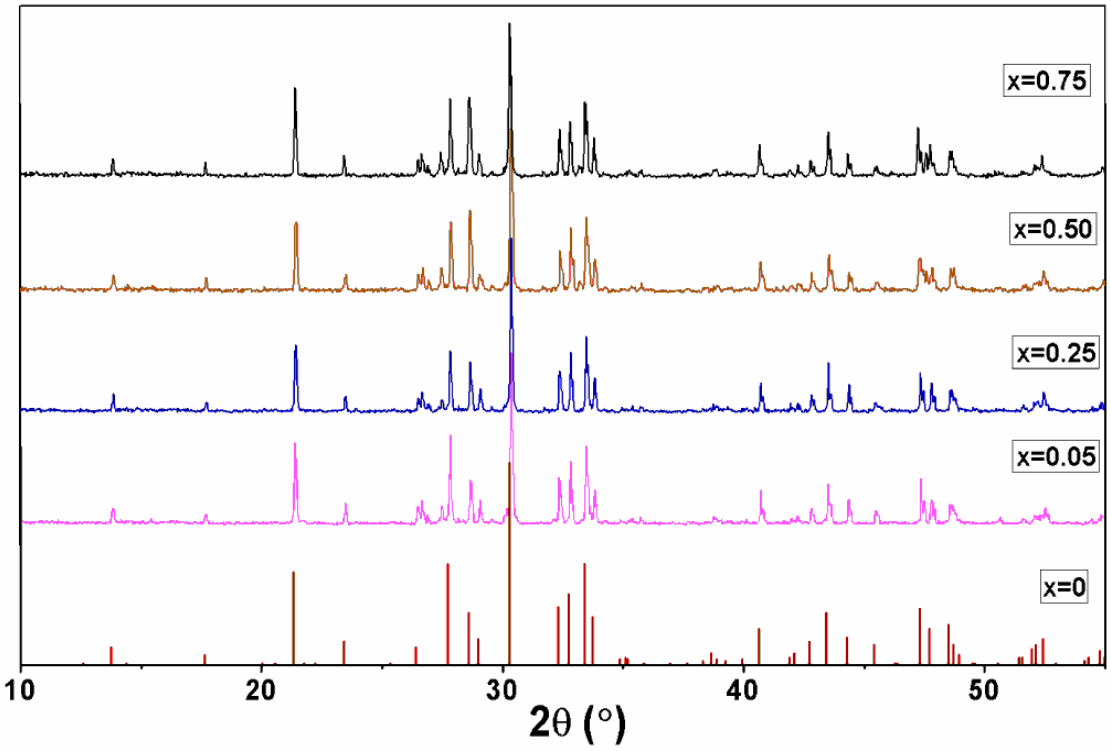

Fig.6.3.1. The XRD patterns of the NCTO5, NCTO25, NCTO50 and NCTO75 powders.

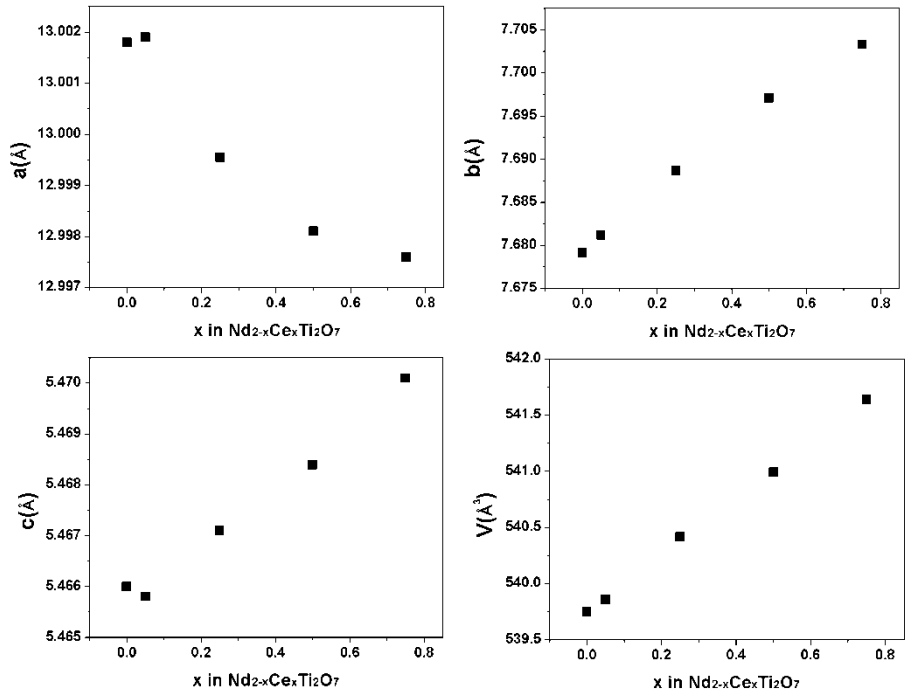

Fig.6.3.2. The variation of $Nd_{2-x}Ce_xTi_2O_7$ unit cell parameters. The data for NTO is from ref.[6].

The solid solution materials adopt the monoclinic structure with $P2_1$ space group. Fig.6.3.2 shows the lattice parameters change with the increasing Ce substitution based on the XRD data. The a- axis decreases slightly and the b- and c- axes increase with increasing x. The unit cell volume increases with increasing x. This is due to that Ce ionic size (134 Å) is bigger than Nd ionic size (127 Å). These results are in agreement with the existence of the Nd/Ce solid solutions. According to the literature, the spontaneous polarization is along c-axis direction.[1,6,7]

Fig.6.3.3 shows SEM images of the NCTO5, NCTO25, NCTO50 and NCTO75 powders. The particle shape does not change with increasing Ce substitution. The powder size is about 0.5um on average.

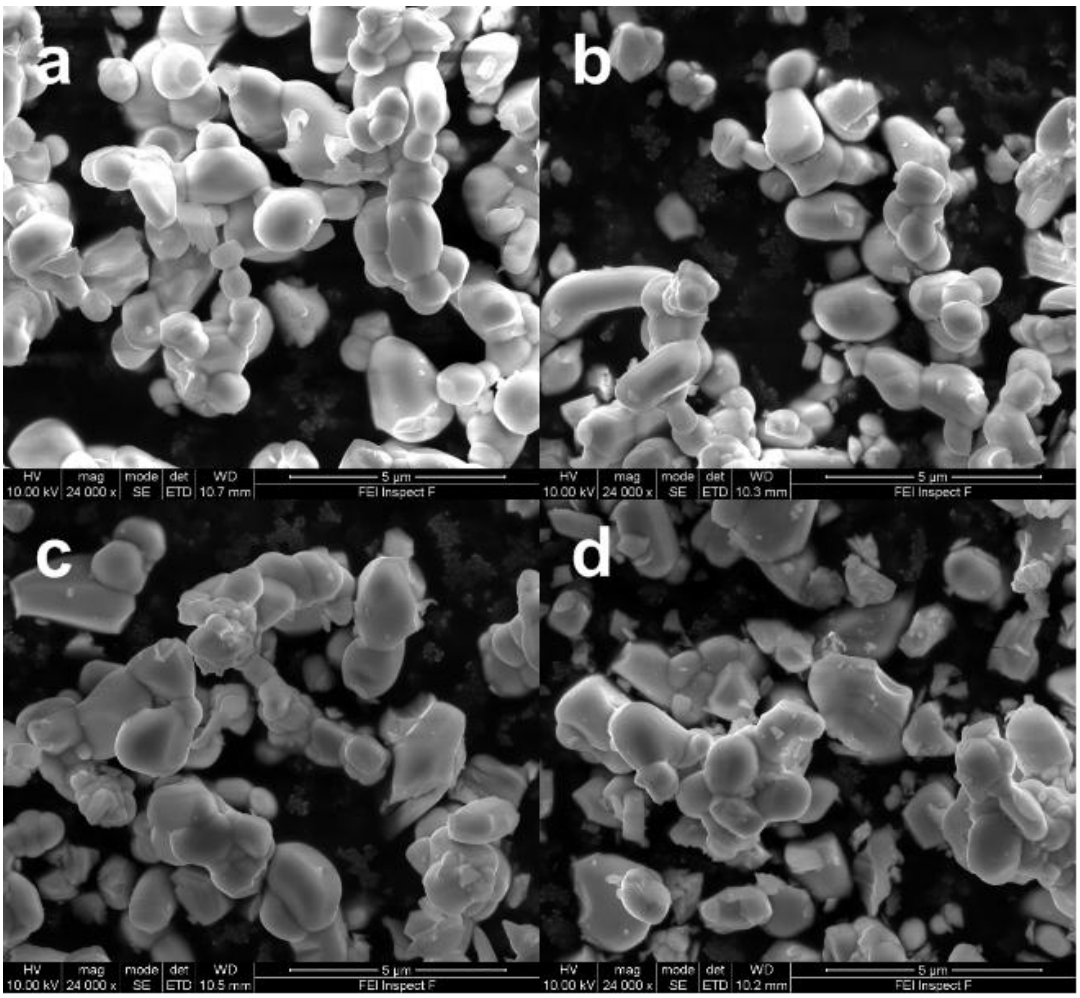

Fig.6.3.3. SEM of the powders after ball milling: (a) NCTO5; (b) NCTO25; (c) NCTO5 and (d) NCTO75.

Fig.6.3.4 shows the XRD patterns of textured NCTO5, NCTO25, NCTO50 and NCTO75 ceramics. The XRD patterns from a plane parallel to the SPS pressing direction exhibit intense (h00) reflections, which indicates that the sintered ceramics samples are textured. The Lotgering factor f of NCTO5, NCTO25, NCTO50 and NCTO75 were calculated as 0.68, 0.66, 0.66 and 0.65 respectively for planes parallel to the SPS pressing direction.

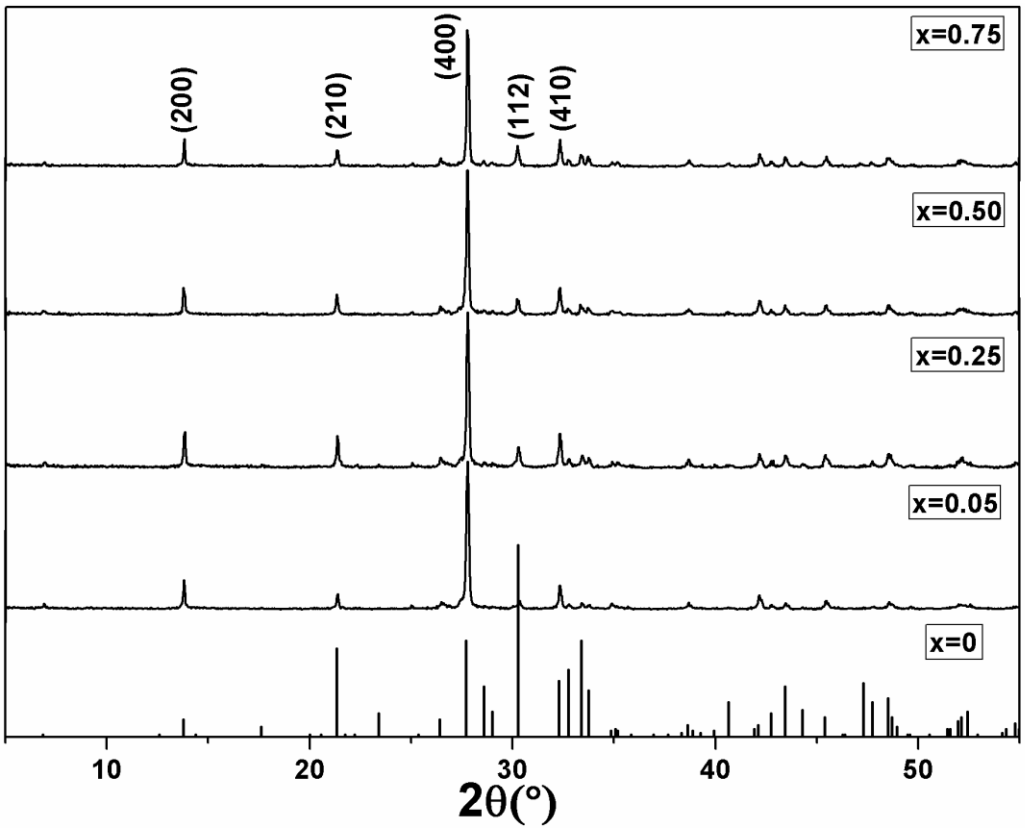

Fig.6.3.4. The XRD patterns for the parallel direction of textured NCTO5, NCTO25, NCTO50 and NCTO75 ceramics.

The densities of the sintered ceramics are presented in Fig.6.3.5, and the insert shows the theoretical densities. With increasing Ce, the theoretical density decreases due to the cell volume increasing (Fig.6.3.2). The ceramics have similar densities from 94% to 91% after same sintering process.

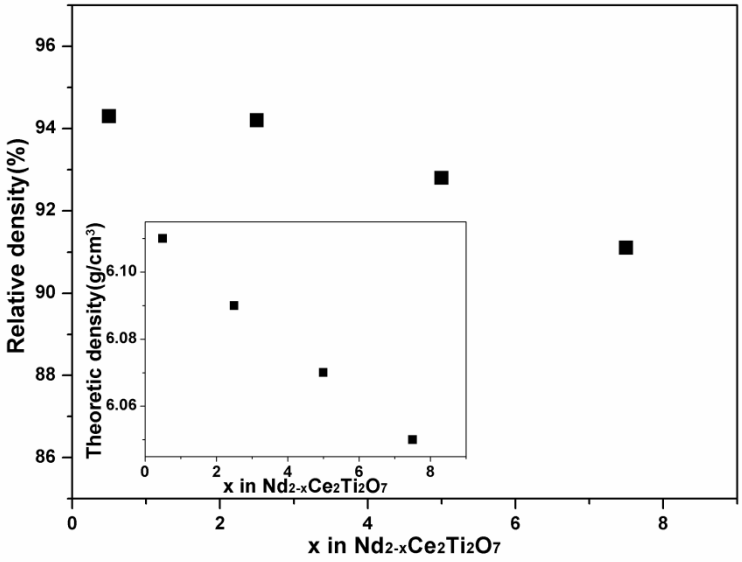

Fig.6.3.5. The densities of the textured NCTO5, NCTO25, NCTO50 and NCTO75 ceramics.

Fig.6.3.6 and Fig.6.3.7 show the SEM pictures of the polished surfaces of the textured NCTO5, NCTO25, NCTO50 and NCTO75 ceramics viewed perpendicular (//) and parallel ($\perp$) to the SPS pressing direction. The grains of NCTO5, NCTO25, NCTO50 and NCTO75 ceramics are similar and plate-like. On average, the grains are about 1-2 μm in thickness and 4-5 μm in the other two dimensions. The ferroelectric spontaneous polarization, Ps is along the c-axis, which is along the grain orientation direction and perpendicular to the SPS pressing direction. The grains are oriented perpendicular to the SPS pressing direction, which is consistent with the XRD results. For NCTO5, NCTO25, NCTO50 and NCTO75 ceramics, there are some pores at the grain boundary which reduced the density.

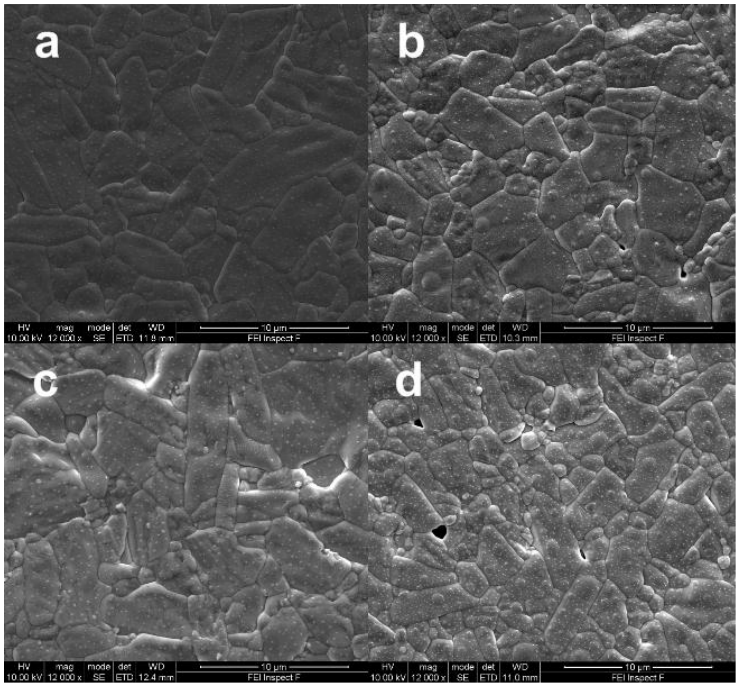

Fig.6.3.6. SEM micrographs of etched surface viewed parallel (//) to the pressing direction of the textured ceramics: (a) NCTO5; (b) NCTO25; (c) NCTO5; and (d) NCTO75.

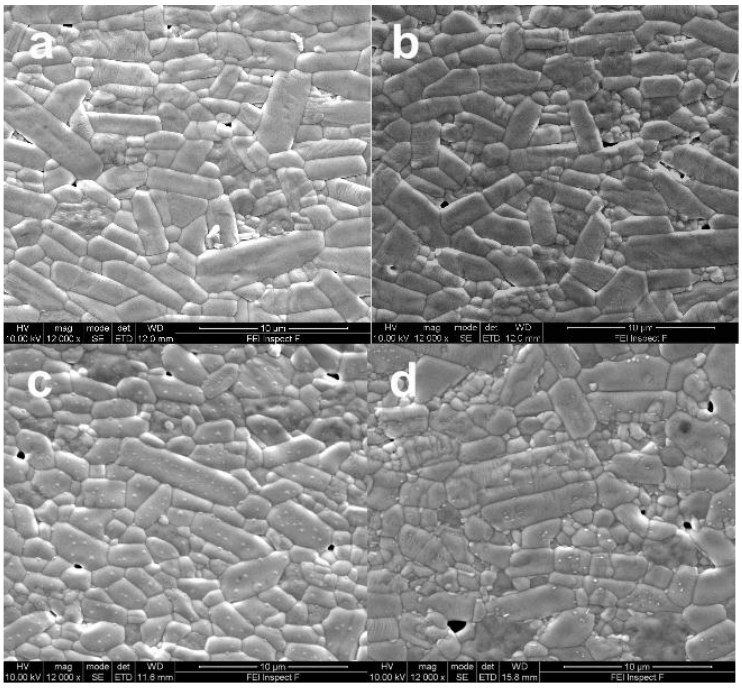

Fig.6.3.7. SEM micrographs of etched surface viewed perpendicular ($\perp$) to the pressing direction of the textured ceramics: (a) NCTO5; (b) NCTO25; (c) NCTO5; and (d) NCTO75.

Fig.6.3.8 (a-d) shows the temperature dependence of dielectric constant and loss of NCTO5, NCTO25, NCTO50 and NCTO75, respectively, measured at two different frequencies of 500 kHz and 1000 kHz. From these figures, the Tc of NCTO5, NCTO25, NCTO50 and NCTO75, are 1475±5 ℃, 1465±5 ℃, 1455±5 ℃ and 1445±5 ℃ respectively. The Tc of $Nd_2Ti_2O_7$ (NTO) has previously been reported as 1482±5 ℃.[6] The dielectric loss increases with increasing Ce substitution. The peaks of loss just below Tc is produced by domain wall movement. For NCTO75, there is a broad peak highlighted by an arrow below the Curie point. This is produced by second phase in material, which is also confirmed by the XRD result.

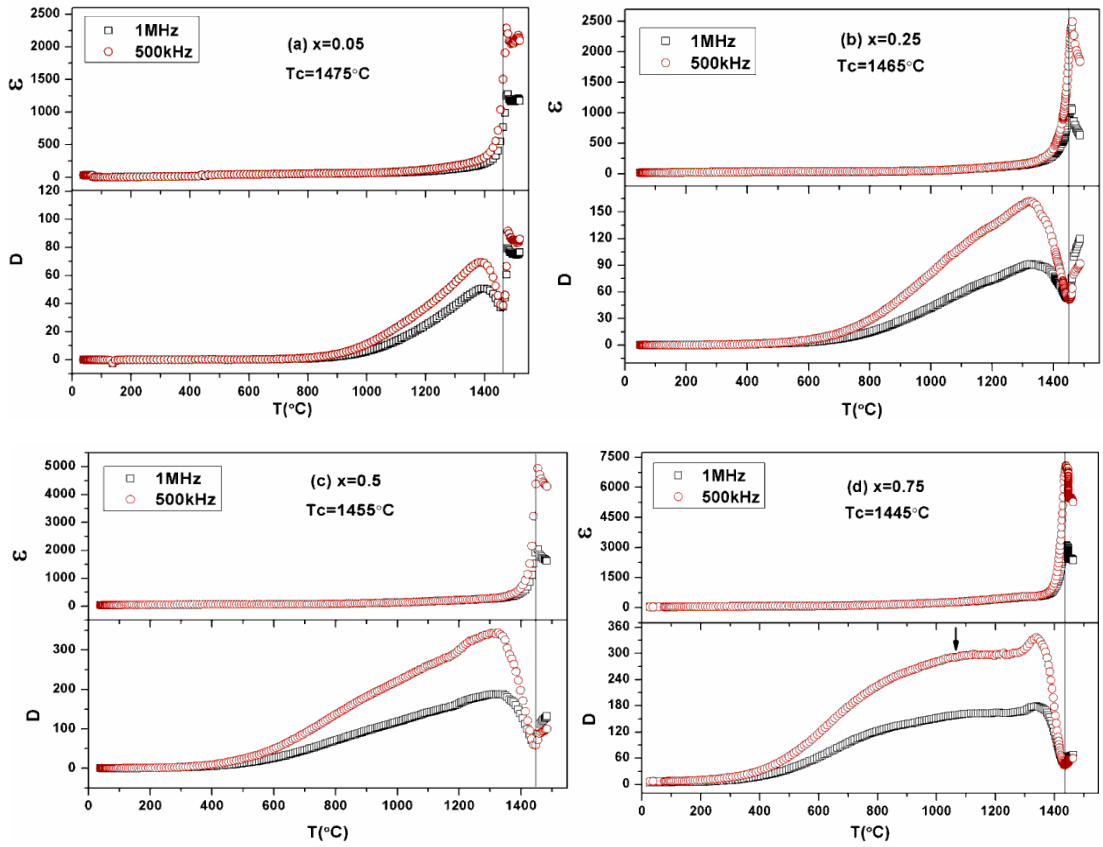

Fig.6.3.8. The temperature dependence of dielectric constant and loss of (a) NCTO5, (b) NCTO25, (c) NCTO50 and (d) NCTO75.

The DC resistivity of the ceramics are shown in Fig.6.3.9. With increasing Ce substitution, the resistivity decreases. The insert in Fig.6.3.9 shows the Arrhenius relation between resisitivity and temperature. Based on the fitting, the energies are 1.52, 0.47, 0.41 and 0.44 eV for NTO, NCTO25, NTO50 and NCTO75 samples. The activation energy of NCTO5 can be fitted into two parts according to different slopes. From 100 ℃ to 400 ℃, the activation energy is 0.40eV (Ea_1) which is similar to the values for NCTO25, NCTO50 and NCTO75. The activation energy of NCTO5 from 500 ℃ to 950 ℃ is calculated as 1.55eV (Ea_2). This indicates the conductivity mechanism of NCTO5 is different from high temperature (500 ℃-950 ℃) to low temperature (100 ℃-400 ℃). The band gap of NTO is reported as 2.8-3.6 eV. The activation energy for intrinsic charge carriers should be the half of band gap. Compared to this, the activation energies of NCTO25, NCTO50 and NCTO75 are much lower. It suggests that the DC conductivities of them is produced by an extrinsic charge carriers produced by Ce. The conductivity mechanism of NCTO5 is dominant by extrinsic charge carriers at low temperature (100 ℃-400 ℃) and is intrinsic conductivity at high temperature (500 ℃-950 ℃).

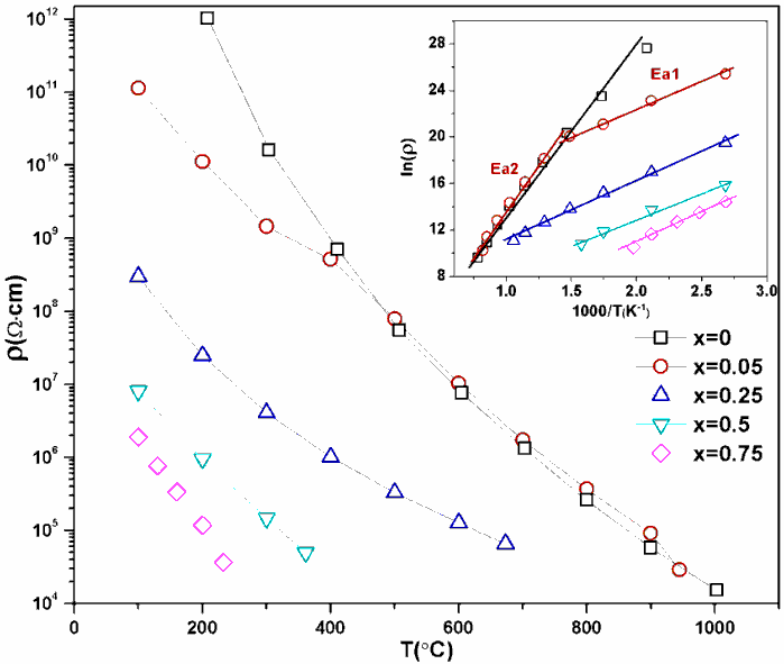

Fig.6.3.9. Direct-current resistivity of NTO,[6] NCTO5, NCTO25, NCTO50 and NCTO75 textured ceramics. The insert is the ln-ln plots of resistivity versus 1/T.

Fig.6.3.10 shows the frequency dependence of the dielectric constant and loss of NCTO5, NCTO25, NCTO50 and NCTO75 measured at room temperature. The loss of NTO and NCTO5 are similar in the whole frequency range. The loss value of the NTO and NCTO5 are small and stable, that means the Ce substituted Nd in the lattice well for NCTO5 compound and any loss contributed by the dipole defects is small. From NCTO25 to NCTO75 the loss increases with increasing Ce. The loss decreases with increasing frequency, which is almost the same when the frequency is close to 10^7 Hz. The permittivity in the perpendicular direction is higher than the parallel direction, this is due to the layered structure which is consistent with the data for NTO single crystal, where the dielectric constant along the Ps direction, c-axis, is higher than the average value along the a- and b- axes.

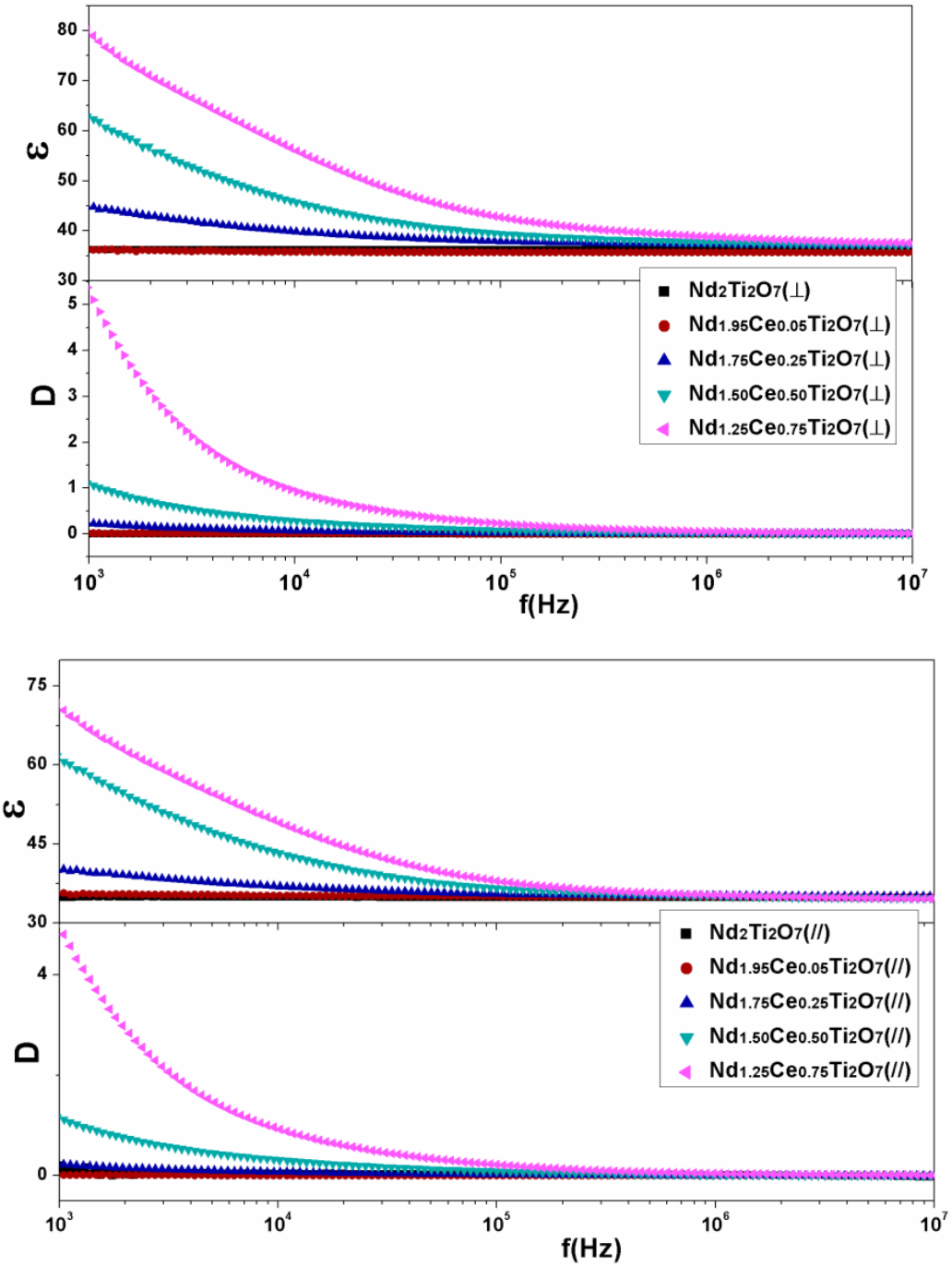

Fig.6.3.10. Frequency dependence of dielectric constant and loss of NTO,[6] NCTO5, NCTO25, NCTO50 and NCTO75 ceramics perpendicular (⊥) and parallel (//) directions.

6.4. Conclusion

The $Nd_{2-x}Ce_xTi_2O_7$(x=0.05, 0.25, 0.5, 0.75) textured ceramics were prepared by spark plasma sintering. The limit of Ce substitution in $Nd_{2-x}Ce_xTi_2O_7$ was found to be x<0.75. the a- axis decreases slightly and the b- and c- axes increase with increasing Ce substitution. The cell volume increases from $Nd_2Ti_2O_7$ to $Nd_{1.25}Ce_{0.75}Ti_2O_7$. The Curie point (Tc) of $Nd_{2-x}Ce_xTi_2O_7$(x=0, 0.05, 0.25, 0.5, 0.75) decreases with increase Ce doping. The electrical resistivity decreases with increasing Ce due to the extrinsic charge carriers produced by Ce substitution.

Reference

(1). Kimura, M., Nanamatsu, S, Kawamura, T., and Matsushita, S., *Japanese Journal of Applied Physics*, 1974. **13**: p. 1473-1474.

(2). Scheunemann, K., and Mullerbuschbaum, H., *Journal of Inorganic and Nuclear Chemistry*, 1975. **37**: p. 2261-2263.

(3). Kimura, M., Matsushi, S., Nanamats, S., Takahash, M., and Doi, K., *Japanese Journal of Applied Physics*, 1972. **11**: p. 904-907.

(4). Kimura, M., Nanamats.S, Doi, K., Matsushi. S., Igarashi, S., and Takahash.M., *Nec Research and Development*, 1973. **17**: p. 10-14.

(5). Ishizawa, N., F. Marumo, S. Iwai, M. Kimura, and T. Kawamura, *Acta Crystallographica Section B-Structural Science*, 1982. **38**(FEB): p. 368-372.

(6). Yan, H., Ning, H., Kan, Y., Wang, P., and Reece, M., *Journal of the American Ceramic Society*, 2009. **92**(10): p. 2270-2275

(7). Lichtenberg, F., A. Herrnberger, K. Wiedenmann, and J. Mannhart, *Progress in Solid State Chemistry*, 2001. **29**: p. 1-70.

Chapter VII. Results - $Sr_{2-x}Ba_xNb_2O_7$ solid solution system

7.1. Introduction

$Sr_2Nb_2O_7$ (SNO) was confirmed as a ferroelectric material and it has a high Curie point (Ceramic ~1327 ℃).[1-3] The substitution of Ba into $Sr_2Ta_2O_7$, which has similar structure to $Sr_2Nb_2O_7$, produced relaxor properties in $Sr_{1.6}Ba_{0.4}Ta_2O_7$.[4,5] Although the solid solution limit of $Sr_{2-x}Ba_xNb_2O_7$ ceramics has been reported as x=0.6 and the phase transition temperature decreases with increasing Ba,[3,5] there are no experiment results reported on the ferroelectric properties and relaxor behavior of $Sr_{2-x}Ba_xNb_2O_7$ compounds and the mechanism of spontaneous polarization and Curie point change are not clear. In the current work, single phase, dense and textured $Sr_{2-x}Ba_xNb_2O_7$ (x=0.1, 0.2, 0.3, 0.4, 0.5) ceramics were prepared for the first time and their ferroelectric and dielectric properties were characterized.

7.2. Experiment Details

The $Sr_{2-x}Ba_xTi_2O_7$ (x=0.1, 0.2, 0.3, 0.4) compositions (SBNO1, SBNO2, SBNO3, SBNO4) were obtained by the mixed oxide route. The powders were ball milled at 350rpm for 4 hours and then calcinated at 1250 ℃ for 5h. The $Sr_{2-x}Ba_xTi_2O_7$ (x=0.5, 0.6, 1.0) compositions (SBNO5, SBNO6, SBNO10) were prepared in the same way as x=0.1 to 0.4 compounds except that they were re-milled and calcined at 1250 ℃ for another 5h.

Spark plasma sintering (SPS) with two-step method was used to densify and texture ceramics.[6] The heating rate was 100 ℃/min in all cases. In the first step, the SBNO1, SBNO2, SBNO3, SBNO4 and SBNO5 powders were pressed in a 20-mm-diameter graphite die and sintered at 1200 ℃ under a pressure of 80 MPa for 3 min. In the second step, the samples were placed in a larger die of 30 mm diameter and sintered at 1350 ℃ under a pressure of 80MPa for 5min. The sintered disks were then annealed in air at 1350 ℃ for 20h.

7.3. Results and Discussion

Fig.7.3.1 shows the XRD patterns of the powders. The diffraction peaks of SBNO1, SBNO2, SBNO3, SBNO4 and SBNO5 match the indexed peaks for the structure parameters of SNO (XRD PDF card: 028-1246) structure parameters, which means the materials are single phase within the sensitivity of the technique. SBNO6 and SBNO10 have several XRD peaks that do not match the indexed peaks for SNO, which indicates that the solid solution limit of Ba in $Sr_{2-x}Ba_xNb_2O_7$ is less than 0.6. This is consistent with the literature.[5] The second phase is $Ba_5Nb_4O_{15}$.[7]

Fig.7.3.2 shows SEM images of the SBNO1, SBNO2, SBNO3, SBNO4 and SBNO5 powders after ball milling. There is no apparent difference between the powder particle, and the particle size is 0.7 um. The shape of particle is typical plate-like.

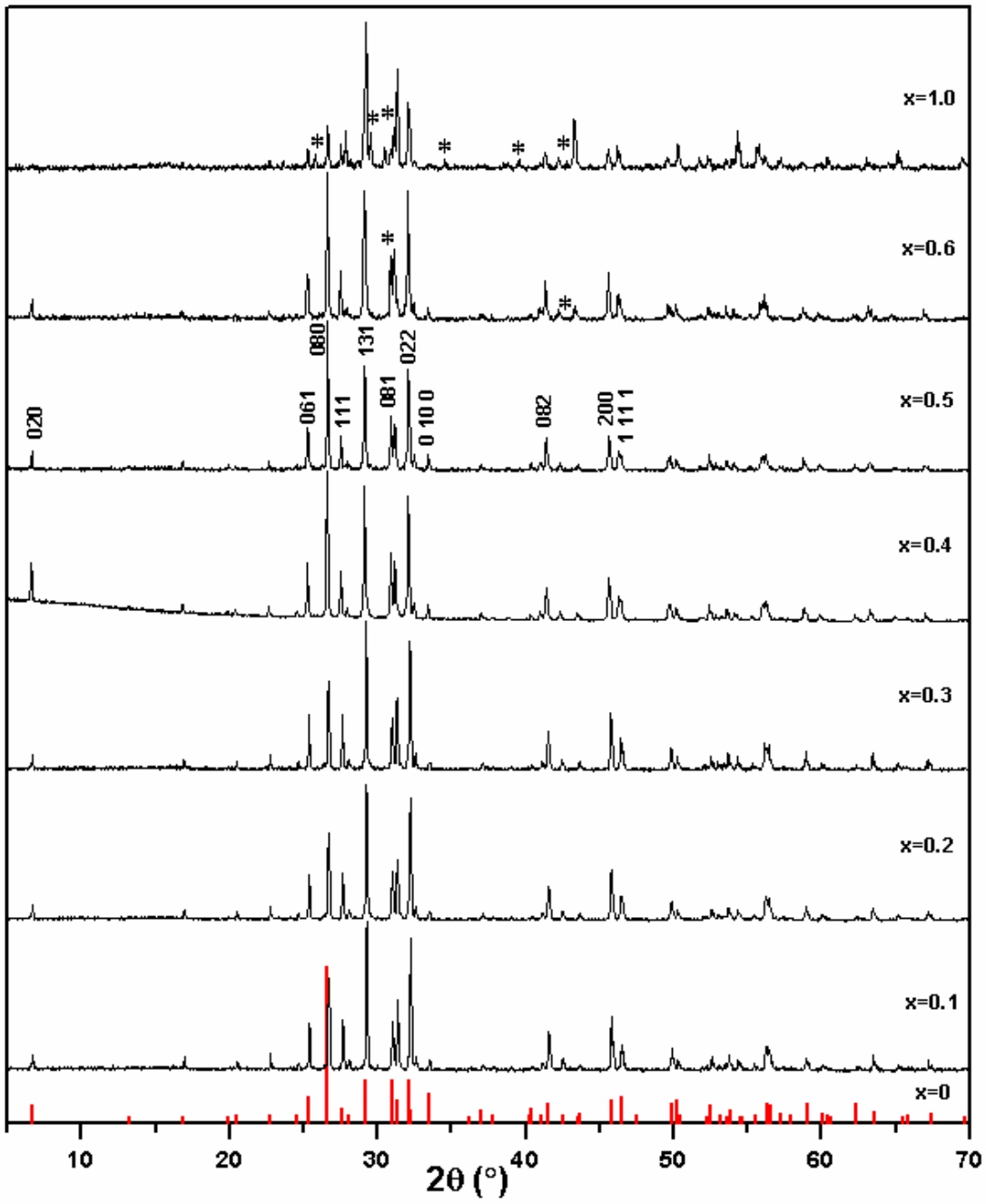

Fig.7.3.1. The XRD patterns of the SBNO6 and SBNO10. The peaks of $Ba_5Nb_4O_{15}$ have been marked by "*".

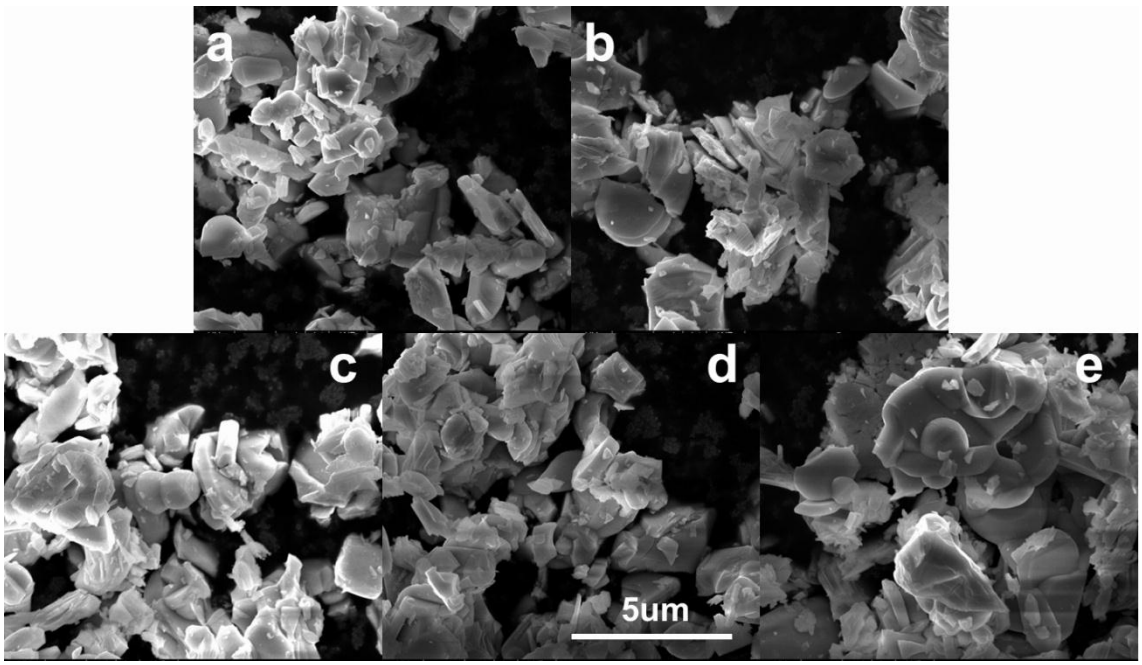

Fig.7.3.2. SEM images of a) SBNO1; b) SBNO2; c) SBNO3; d) SBNO4; and e) SBNO5 powder after ball milling.

Fig.7.3.3 (a-c) show the lattice parameters change with Ba increasing from SNO to SBNO5. SNO has lattice parameters (a, b, c, β) = (3.96Å, 26.78Å, 5.70Å, 90°)[6] with orthorhombic structure, which is consistent with the single crystal data.[3] The Ps direction is along c-axis.[3] From these lattice parameters, all of SBNO1-5 compounds have the same structure as SNO, but with the a-, b- and c-axes increasing with increasing Ba from SBNO1 to SBNO5. The theoretical densities (TD) also increase, which is shown in the insert of fig.7.3.3(d). This is because the mass of the Ba atom is greater than Sr atom.

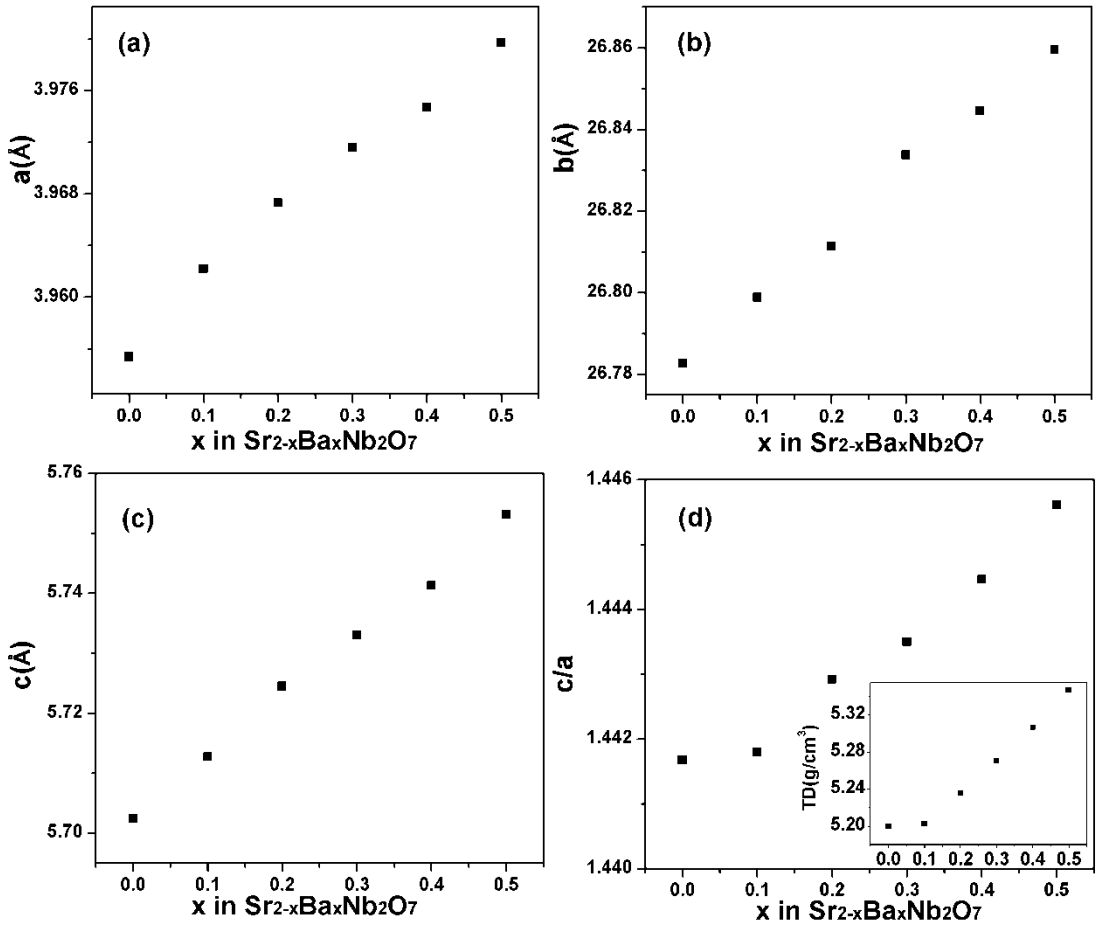

Fig.7.3.3. The lattice parameters of $Sr_{2-x}Ba_xNb_2O_7$ powders as a function of Ba content. The insert shows the theoretical densities.

SNO have a centro-symmetric structure with space group Cmcm above Tc (Fig.7.3.4a), and noncentro-symmetric structure with space group $Cmc2_1$ below Curie point (Fig.7.3.4b).[8] The spontaneous strain, which is induced by the noncentro-symmetric structure, can be used to estimate the spontaneous polarization. Here, the noncentro-symmetric structure is due to the tilting of the oxygen octahedral along a-axis. The structure is further from centro-symmetric when the oxygen octahedral is more tilted, which means the spontaneous strain is greater and the c-axis is shorter. In the present case, the a-, b- and c-axes all increase with Ba increasing. So, the ratio, c/a, was

used to estimate the spontaneous strain (Fig.7.3.3d). According to the structure, the spontaneous polarization of $Sr_{2-x}Ba_xNb_2O_7$ decreases with increasing c/a ratio. Therefore the highest spontaneous polarization is expected for $x \leqq 0.1$.

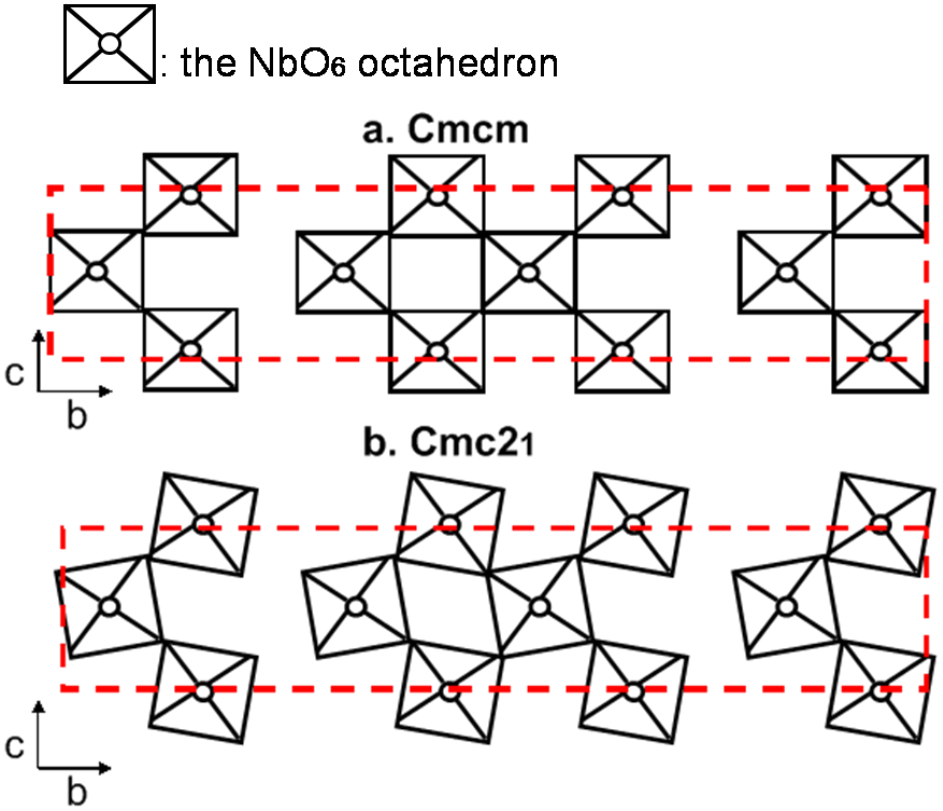

Fig.7.3.4. The structure of: (a) paraelectric phase; and (b) ferroelectric phase of $Sr_2Nb_2O_7$.

Fig.7.3.5 shows the XRD patterns of SBNO1, SBNO2, SBNO3, SBNO4 and SBNO5 textured ceramics. The XRD patterns from the planes with their normal direction parallel to the SPS pressing direction exhibit intense (0k0) reflections, which indicates that the sintered ceramics samples are highly textured. The Lotgering factor f of SBNO1, SBNO2, SBNO3, SBNO4 and SBNO5 were calculated as 0.80, 0.81, 0.81, 0.82 and 0.81, respectively, for the planes with their normal direction parallel to the SPS pressing direction. This means all these samples were well textured and to a similar extent. After

sintering, SBNO1, SBNO2, SBNO3, SBNO4 and SBNO5 ceramics had relative densities of 96.3%, 95,4%, 96.0%, 95.9% and 94.8%.

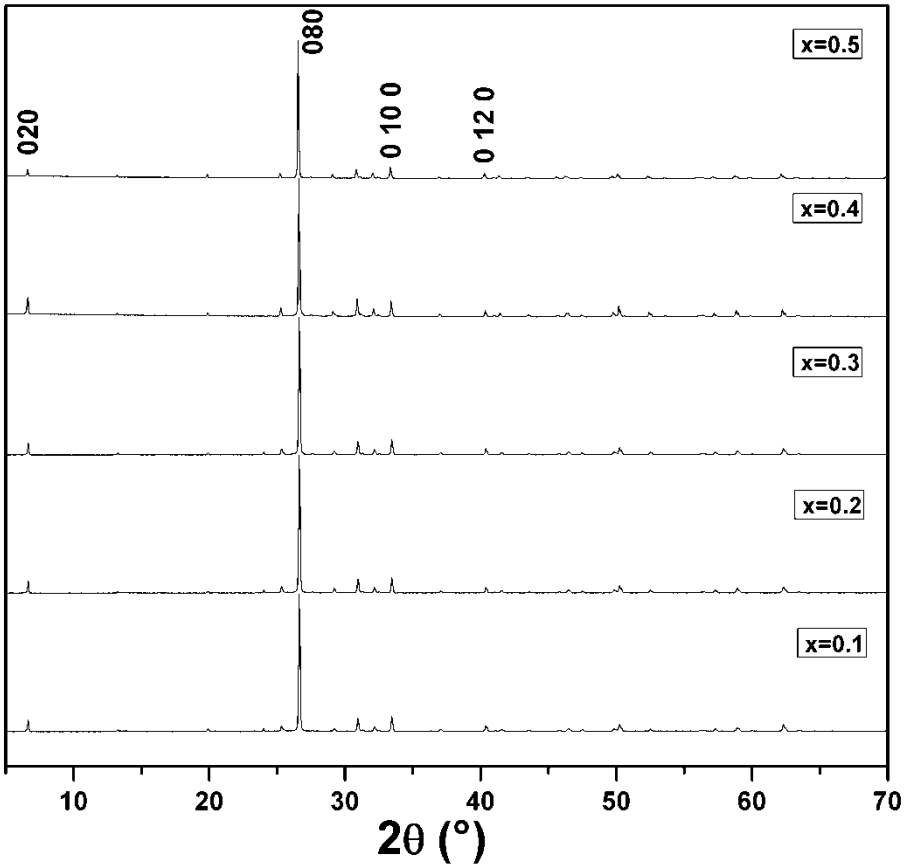

Fig.7.3.5. The XRD patterns of textured SBNO1, SBNO2, SBNO3, SBNO4 and SBNO5 ceramics on parallel direction (//).

Fig.7.3.6-7.3.7 show the SEM pictures of the polished surfaces of the textured SBNO1, SBNO2, SBNO3, SBNO4 and SBNO5 ceramics viewed perpendicular (//) and ($\perp$) to the SPS pressing direction respectively. The grains are plate-like and prefer to grow along the direction perpendicular to the pressing direction. The structure is well textured, which is consistent with the XRD results. On average, the plate-like grains are about 1.5 μm in thickness and 6 μm in the other two dimensions. According to the SEM images, Ba substitution does not change the appearance of the grains in these PLS ceramics.

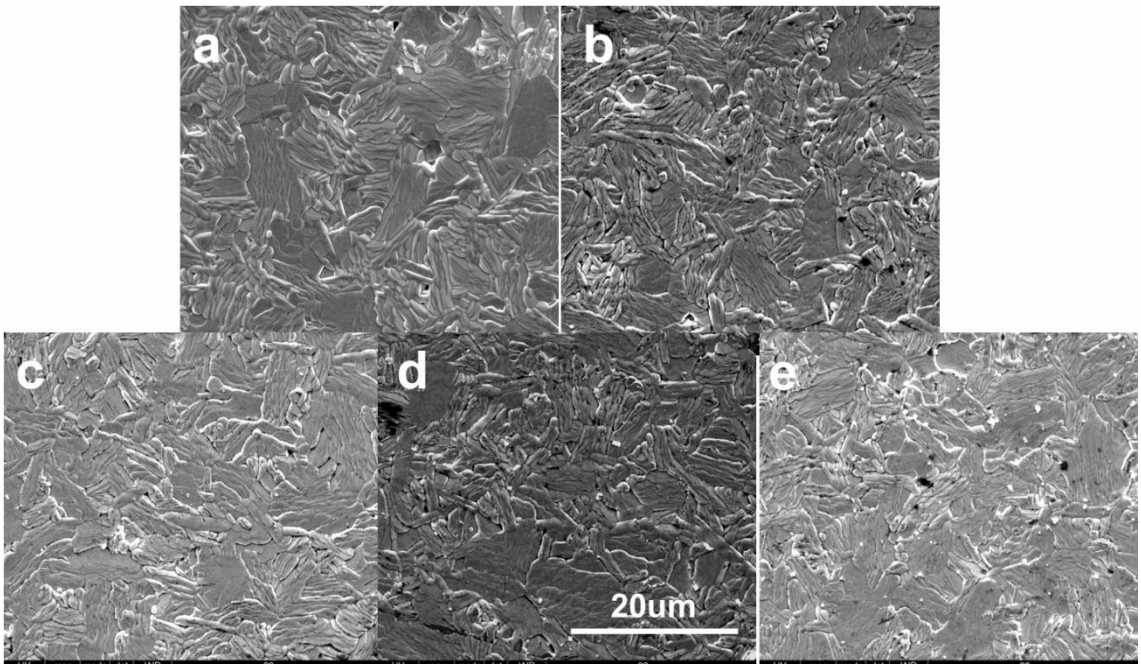

Fig.7.3.6. SEM images of the polished surface of ceramics in parallel direction (//): a) SBNO1; b) SBNO2; c) SBNO3; d) SBNO4; and e) SBNO5.

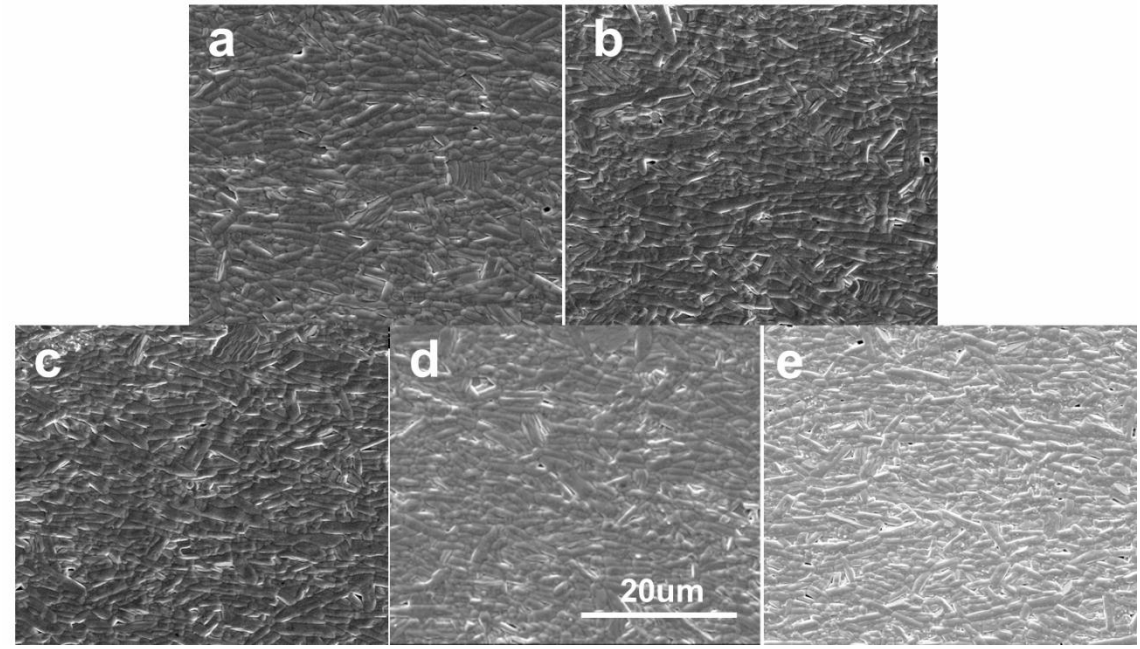

Fig.7.3.7. SEM images of the polished surface of ceramics in perpendicular direction ($\perp$): a) SBNO1; b) SBNO2; c) SBNO3; d) SBNO4; and e) SBNO5.

Fig.7.3.8(a-e) show the current-electric field (I-E) and polarization-electric field (P-E) hysteresis loops for SBNO1, SBNO2, SBNO3, SBNO4 and SBNO5 respectively, measured at 120℃ at 10Hz. The highest voltage that could be applied on the samples decreased with increasing Ba substitution from SBNO1 to SBNO5. When the voltage was increased further, breakdown occurred. For SBNO1, SBNO2, SBNO3 samples, ferroelectric switching is indicated by the current peak at about 8.0, 7.1 and 6.5 kV/mm, respectively, which means that ferroelectric switching is easier with increasing Ba content. In contrast, there is no apparent ferroelectric switching current peak for the SBNO4 and SBNO5 samples, but there is an extra broad small current peak in the I-E loop between -5 to 0 kV/mm marked by the (*) (Fig.6(d-e)), which produces a pinching on the P-E loops. This might be explained by the switching of defect dipoles induced by Ba substitution.[9]

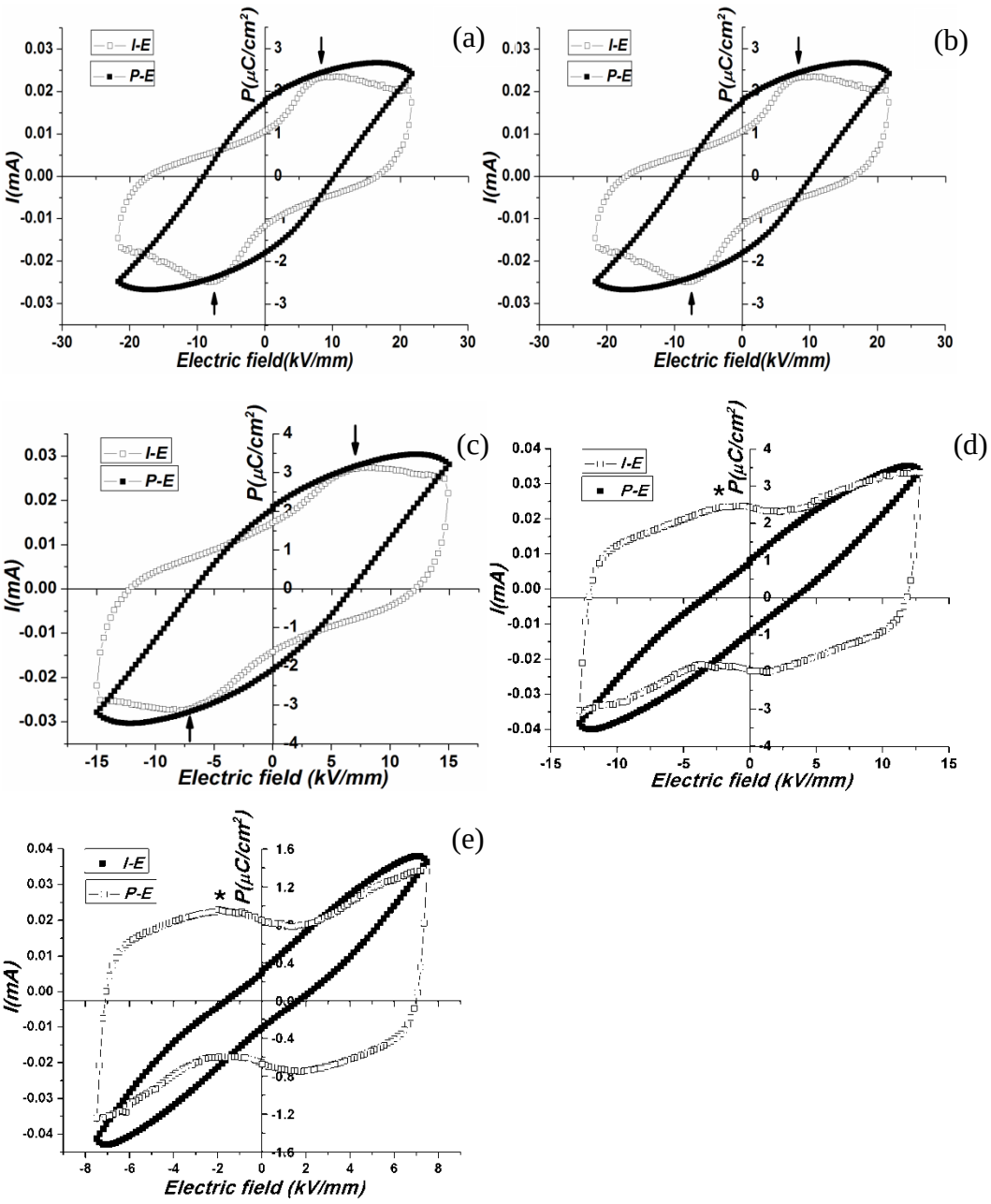

Fig.7.3.8. the current-electric field (I-E) and polarization-electric field (P-E) hysteresis loops for textured ceramics at perpendicular direction (⊥): (a) SBNO1; (b) SBNO2; (c) SBNO3; (d) SBNO4; and (e) SBNO5.

Fig.7.3.9(a-d) show the XPS peaks of Sr 3d, Ba 3d, Nb 3d and O 1s electrons. The binding energy (BE) of the Sr $3d_{5/2}$ and $3d_{3/2}$ states are 133.1 and 134.8±0.2 eV for all the compounds (SBNO1-5). This is in a good agreement of the values for SNO in the literature.[10,11] For Ba $3d_{5/2}$ and $3d_{3/2}$, the values are 794.5 and 779.5±0.2 eV, which is

consistent with the BE values for Ba in the perovskite structure.[10] The Nb 3d state have BEs of 206.9 and 209.6±0.2 eV, for $3d_{5/2}$ and $3d_{3/2}$ respectively, and the values are similar to the value of Nb in SNO.[11] So, in the SBNO solid solution system, Sr, Ba and Nb are stable and the valence does not change with increasing Ba substitution. Conversely, in the O 1s spectrum for SBNO1-5 two peaks (A and B) were observed. The A peak for all the compounds has a BE of about 529.6±0.2 eV. Compared with literature, this value indicates the main O 1s state which is reported as 529.4 eV in SNO.[11] The BE value and intensity of the B peak increase with the Ba substitution. This indicates the O- Ba bonds increase with increasing Ba substitution.[12]

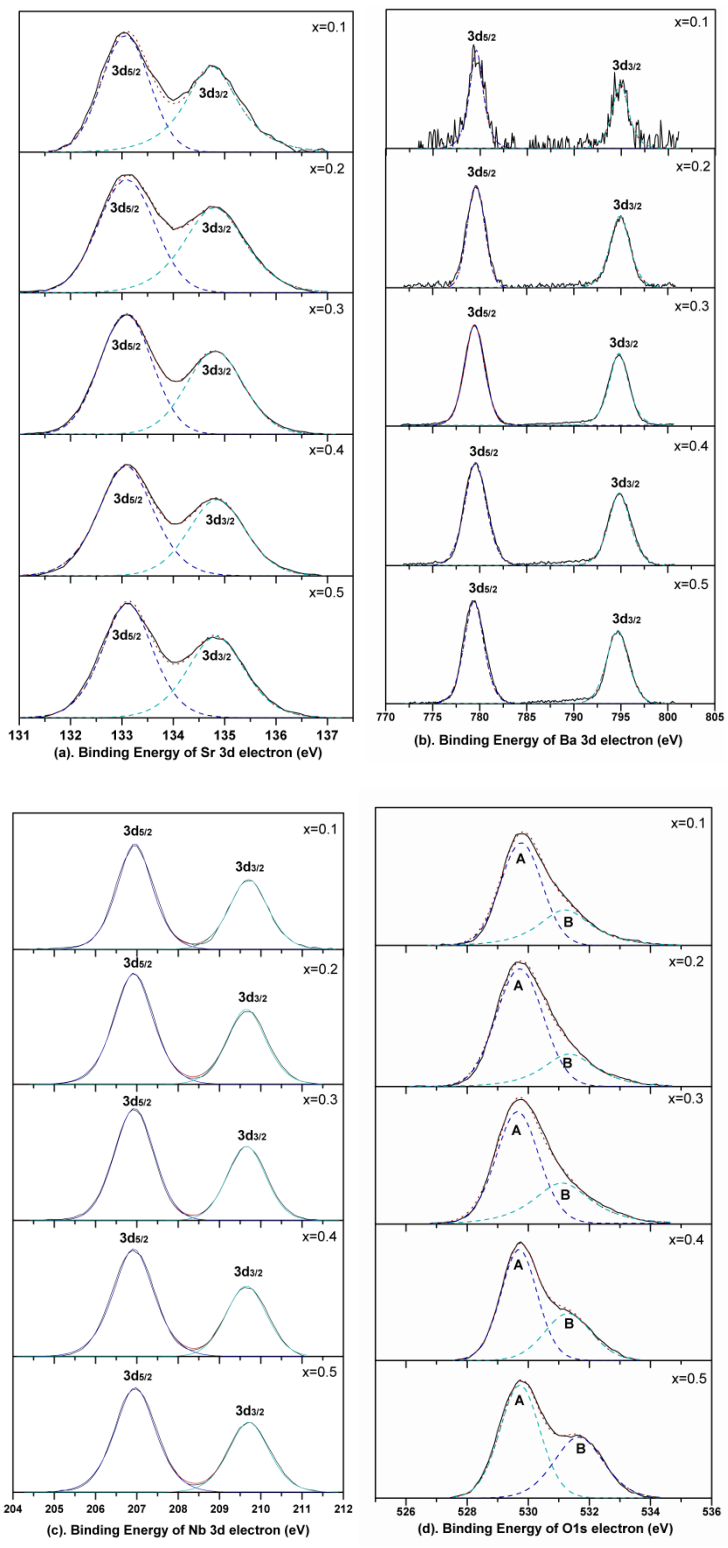

Fig.7.3.9. The XPS peaks for $Sr_{2-x}Ba_xNb_2O_7$ textured ceramics (⊥): (a) Sr 3d; (b) Ba 3d; (c) Nb 3d and (d) O 1s electron.

Fig.7.3.10(a-e) show the temperature dependence of dielectric constant and loss of SBNO1-5 ceramics respectively, measured at three different frequencies of 100kHz, 500kHz and 1000kHz. From these figures, the Tc of SBNO1-5 are 1253±5 ℃, 1175±5 ℃, 1110±5 ℃, 1075±5 ℃ and 940±5 ℃ respectively. The Tc of SNO has previously been reported as 1327±5 ℃ for ceramic.[6] Nanamatsu also reported the Tc decreasing with increasing Ba substitution.[3] The Tc decrease could be explained by the spontaneous strain decreasing with increasing Ba substitution.[13] The insert figs in fig.8(a-d) show the amplification of temperature dependence loss from 200 – 1000 ℃. There are frequency dependent broad loss peaks could be observed for SBNO1-5. With increasing Ba content, the position of the peaks move to higher temperatures and their intensity increases. These peaks suggest that there are point defects in the materials and their concentration increases with increasing Ba substitution, which is consistent with the hysteresis loops results. The loss peaks just below Tc for all these compounds can be attributed to ferroelectric domain wall movement.[14]

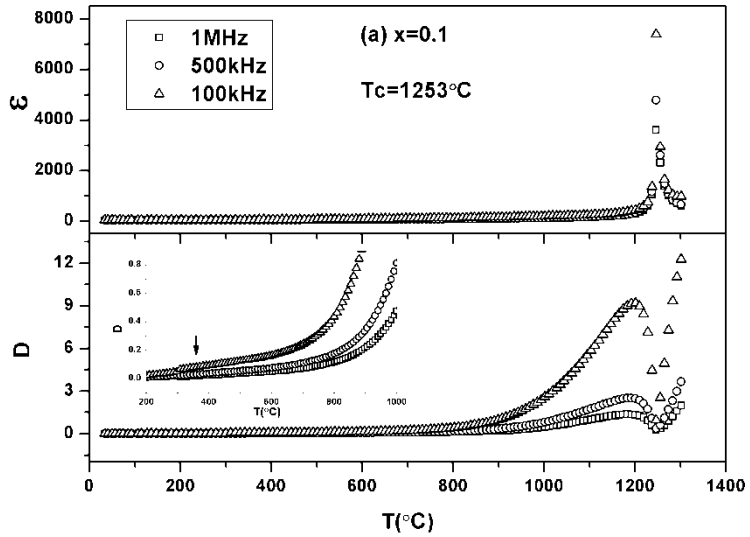
1MHz
500kHz
100kHz
(a) x=0.1
Tc=1253°C
ε
D
T(°C)

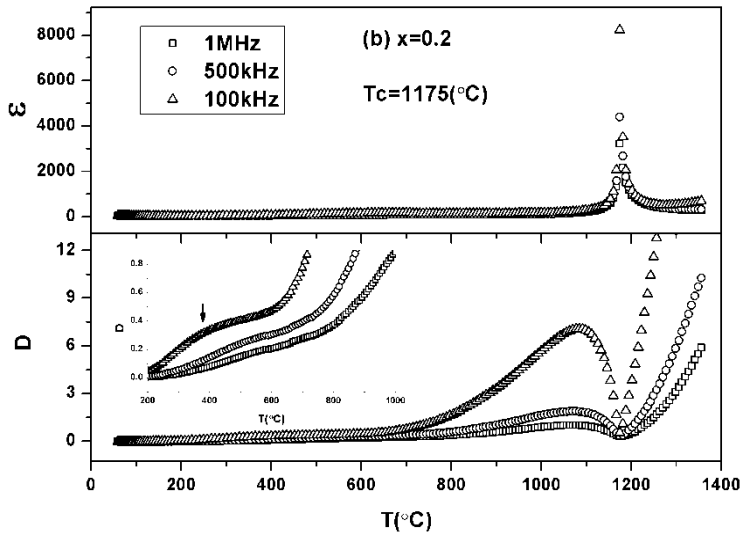
1MHz
500kHz
100kHz
(b) x=0.2
Tc=1175(°C)
ε
D
T(°C)

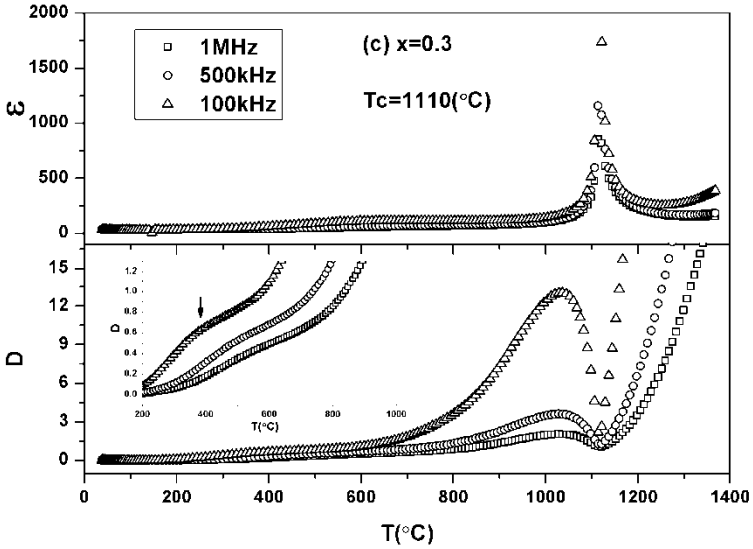
1MHz
500kHz
100kHz
(c) x=0.3
Tc=1110(°C)
ε
D
T(°C)

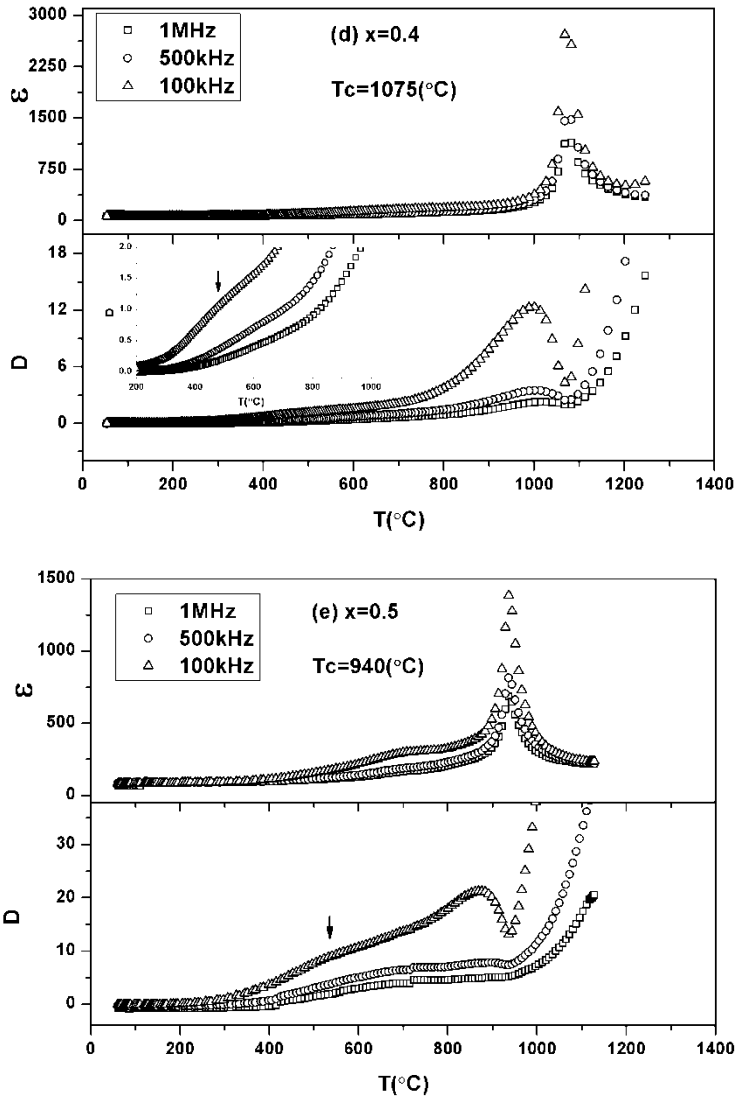

Fig.7.3.10. The temperature dependence of dielectric constant and loss of textured ceramics (⊥) of (a) SBNO1; (b) SBNO2; (c) SBNO3; (d) SBNO4; and (e) SBNO5. The inserts show the temperature dependent loss with higher resolution in the temperature range of 200 – 1000℃.

Fig.7.3.11 shows the frequency dependence of dielectric constant and loss of SNO,[6] SBNO1-5 ceramics measured at room temperature in the perpendicular direction. Typically, all of the losses are low in the whole frequency range which makes them promising materials for application. The loss decreases with increasing frequency. This can be explained by the defects mentioned above, which raise the loss value in the low frequency range. SNO has the lowest permittivity, and with increasing Ba, the

permittivity increases from SBNO to SBNO4. The variation of permittivity could be explained by the Ps is more moveable with increasing Ba substitution, which produced an increasing extrinsic contribution to the electric displacement. The permittivity of SBNO1 to SBNO5 decreases slightly in the range of 10^3 - 10^5 Hz and they are almost unchanged at higher frequency (10^5 - 10^7). Conversely, the permittivity of SNO is stable for the whole range of frequencies (10^3-10^7Hz).

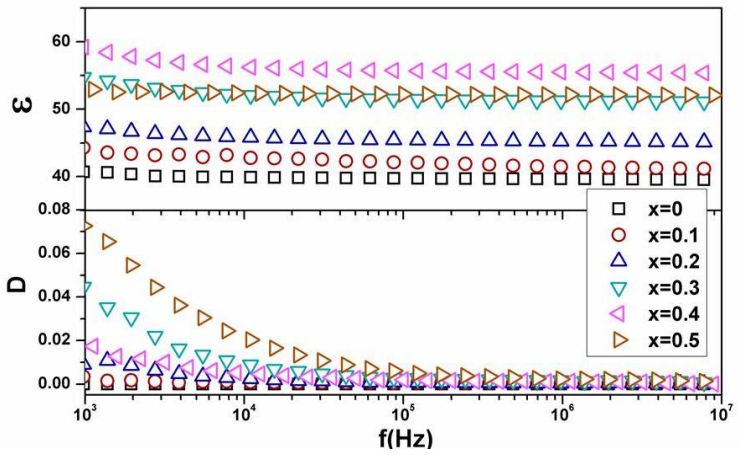

Fig.7.3.11. Frequency dependence of dielectric constant and loss of SNO,[4] SBNO1, SBNO2, SBNO3, SBNO4 and SBNO5 textured ceramics (⊥).

The DC resistivity of SBNO1, SBNO2, SBNO3, SBNO4 and SBNO5 ceramics are shown in Fig.7.3.12. The resistivities of SBNO1, SBNO2, SBNO3 and SBNO4 are about 10^{11} Ω·cm at 200°C and decrease gradually with the same trend to about 10^5 Ω·cm at 900°C. The resistivity of SBNO5 is lower than the other compounds at low temperature (<400 ℃), and then it has the same trend as the other compounds, decreasing from about 10^8Ω/cm at 400°C to 10^5Ω/cm at 900°C.

The insert shows the Arrhenius relation between resistivity and temperature. For SNO, SBNO1, SBNO2, SBNO3, SBNO4 and SBNO5 the energies are 1.04, 0.96, 0.95, 0.95,

0.94 eV and 0.65 eV. The half band gap of SNO was reported as 1.44 eV,[17] the activation energies of SNO to SBNO5 are lower, which reflects that the extrinsic charge carrier lower the activation energy. From SNO to SBNO5, the activation energy decreases with increasing Ba substitution. This might be explained by the point defects produced by the Ba substitution is increasing and affected the conductivity mechanism. This is also consistent with the hysteresis loop and temperature dependent permittivity results.[18]

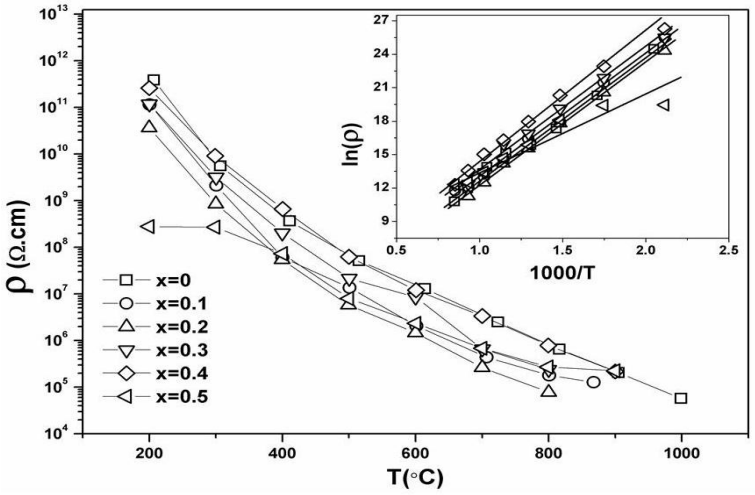

Fig.7.3.12. Direct-current resistivity of SNO,[4] SBNO1, SBNO2, SBNO3, SBNO4 and SBNO5 textured ceramics (⊥).

The piezoelectric constant d_{33} was measured by poling the samples in silicone oil at 120 ℃ under various DC electric fields (15-35 kV/mm). The measured d_{33} increases from SBNO1 to SBNO2 and then the d_{33} decreases with further increasing Ba content (Fig.7.3.13). The highest d_{33} is 3.6 ± 0.1pC/N for SBNO2, which is much higher than for SNO (lotgering factor: 0.86; density: 96.5%), reported as 2.8 pC/N.[6] The ferroelectric behavior of all these materials are confirmed by the d_{33} and the hysteresis loop results. The maximum d_{33} for SBNO2 can be explained by the coercive field

decreasing with increasing Ba substitution from SNO[6] to SBNO2, which makes ferroelectric switching easier, but the spontaneous strain also decreases, leading to the d_{33} decreasing with further increasing Ba. The thermal depoling data is shown in Fig.7.3.14. All of the compounds have very stable d_{33} below Tc. Especially SBNO1 and SBNO2, both of them can be used above 1150 ˚C. Compared to SNO,[35] the d_{33} is more stable for SBNO1 and SBNO2, and there is no thermal depoling is observed up to Tc.

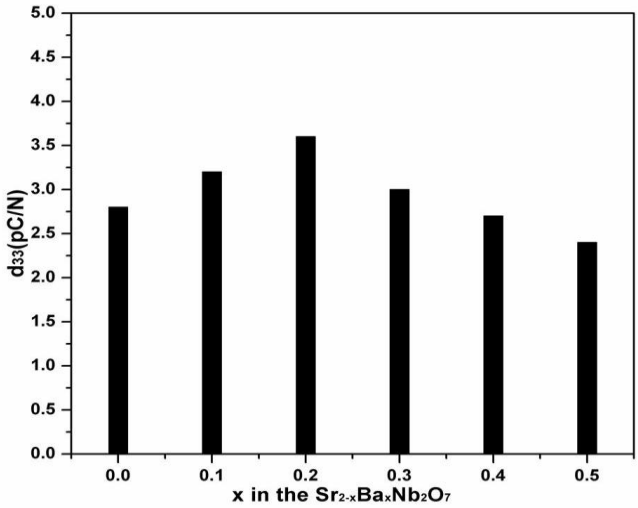

Fig.7.3.13. Piezoelectric constant (d_{33}) of textured ceramics (⊥).

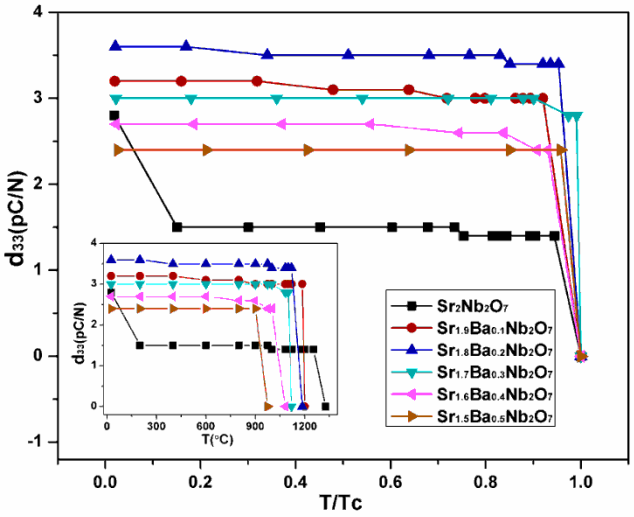

Fig.7.3.14. Effect of thermal depoling on piezoelectric properties; the d_{33} data plotted with homologous temperature. The insert is the real value of d_{33} after annealing.

7.4.Conclusions

The solid solution system of $Sr_{2-x}Ba_xNb_2O_7$ ($x<0.6$) were investigated. All these compounds were confirmed as very stable ferroelectric materials. The solid solution limit ($x<0.6$) of $Sr_{2-x}Ba_xNb_2O_7$ was determined by XRD as $x=0.6$. The a-, b-, c- axes and cell volume increase with Ba^{2+} addition because Ba^{2+} (160 Å) has a larger ion radius than Sr^{2+} (144 Å). The textured ceramics of $Sr_{2-x}Ba_xNb_2O_7$ were prepared for the first time. Substitution of Ba can decrease the spontaneous polarization and increase the mobility of domain switch. $Sr_{2-x}Ba_xNb_2O_7$ ($x=0.1$, 0.2) are the most promising materials for high temperature applications due to their stable piezoelectric constant and high Curie point. The highest d_{33} was measured as 3.6 ± 0.1pC/N for $Sr_{1.8}Ba_{0.2}Nb_2O_7$.

References

(1). Nanamatsu, S., Kimura, M., Doi, K., Takahashi, M., *Journal of the Physical Society of Japan*, 1971. **30**: p. 300-301.

(2). Nanamatsu, S., Kimura, M., Doi, K., Takahashi, M., *Nec Research and Development*, 1972. **13**: p. 17-21.

(3). Nanamatsu, S., M. Kimura, and T. Kawamura, *Journal of the Physical Society of Japan*, 1975. **38**(3): p. 817-824.

(4). Isupov, V.A., *Ferroelectrics*, 1999. **220**(1-2): p. 79-103.

(5). Podkrytov, A., Animitsa, I., Shindelman, N., Zhukovskii, V., Lozhkina, E., and Perelyaeva, L., *Inorganic Materials*, 1988. **24**: p. 1742-1745.

(6). Ning, H., Yan, H., and Reece, M., *Journal of the American Ceramic Society*, 2010. **93**(5): p. 1409-1413.

(7). Leshchenko, P., Lykova, L., Kovba, L., Ippolitova, E., Shevchenko, A., and Lopato, L., *Inorganic Materials*, 1983. **19**: p. 581-584.

(8). Ishizawa, N., Marumo, F., Kawamura, T., and Kimura, M., *Acta Crystallographica Section B-Structural Science*, 1975. 31: p.1912-1915.

(9). Zeng, T., Yan, H., Reece, M., *Journal of Applied Physics*, 2010. **108**: p. 096101.

(10). Xu, C., Xia, Y., Liu, Z., Meng, X., *Journal of Physics D: Applied Physics*, 2009. **42**: p. 085302.

(11). Atuchin, V., Grivel, J., Korotkov, A., and Zhang, Z., *Journal of Solid State Chemistry*, 2008. **181**: p. 1285-1291.

(12). Shah, L., Ali, B., Zhu, H., Wang, W., Song, Y., Zhang, H., Shah, S., and Xiao, J., *Journal of Physics: Condensed Matter*, 2009. **21**: p. 486004.

(13). Abrahams, S. C., S. K. Kurtz, and P. B. Jamieson, *Physical Review*, 1968. **172**(2): p. 551.

(14). Hardtl, K., *Ceramics International*, 1982. **8**: p. 121-127.

(15). Chen, A., Guo, R. Y., Bhalla, S., and Cross, L. E., *Integrated Ferroelectrics*, 2002. **42**: p. 419-431.

(16). Matsuo, Y., Takahashi, K., and Ikehata, S., *Journal of the Physical Society of Japan*, 2001. **70**: p. 2934-2938.

(17). Jeong, E. D., Ha, M. G., Won, M. S., Kim, H. G., Pak, H. K., Borse, P. H., Ji, S. M., and Lee, J. S., *Journal of the Korean Physical Society*, 2006. **49**: p. S671-S674.

(18). Su, H., Wang, R., Fuchs, H., Gardner, J., Evenson, W., Sommers, J., *Journal of the American Ceramic Society*, 1990. **73**: p. 3215-3219.

Chapter VIII. Results – Thermal depoling and phase transitions in $La_2Ti_2O_7$ and $Sr_2Nb_2O_7$

8.1. Introduction

$La_2Ti_2O_7$ and $Sr_2Nb_2O_7$ with perovskite-like layered structure have super high Curie points (LTO ~ 1461 ˚C; SNO ~ 1342 °C) and they are the most promising candidates for the high temperature ferroelectric applications even in PLS family due to their relatively high piezoelectric constant (> 2.0 pC/N) compared to other PLS ceramics.[1-7] However, the information on their thermal depoling behavior, which is critical to their application, is very limited. In the present work, the thermal stability of piezoelectric $La_2Ti_2O_7$ and $Sr_2Nb_2O_7$ ceramics was investigated. Their thermal depoling behavior and phase transition mechanism at Curie point have been studied.

8.2. Experiment Details

The LTO and SNO compounds were prepared by the solid reaction route. The calcination conditions were 1250 ˚C and 1200 ˚C for 4h for $La_2Ti_2O_7$ and $Sr_2Nb_2O_7$, respectively. To produce ceramics, $La_2Ti_2O_7$ and $Sr_2Nb_2O_7$ powders were sintered in graphite dies (20mm diameter) for 3 min at 1550 °C and 1425 °C, respectively, under a pressure of 100 MPa using SPS. A heating rate of 100 ˚C/min was used in all cases.

The thermal stability of d_{33} was tested by holding the samples at high temperatures in the furnaces for 2 hours, then d_{33} was measured at room temperature.

8.3. Results and Discussion

Fig.8.3.1 and Fig.8.3.2 show dielectric constant (ε) and dielectric loss (D) of LTO and SNO ceramics as a function of temperature at 1MHz, 500kHz and 100kHz measured during (a) heating and (b) cooling. The insert of Fig.8.3.1 (a) and Fig.8.3.2 (a) shows the dielectric constant at 100 kHz over a wide range of temperature. A heating rate of 3 ˚C/min was used in all cases. The insert in Fig.8.3.1 (b) and Fig.8.3.2 (b) shows a plot of 1/ε as a function of temperature above the Curie point, for the dielectric constant (ε) measured during heating process (100 kHz). Fig.8.3.3 (a) shows the free energy (G_0) as a function of polarization (P) for a first order and second order ferroelectric to paraelectric phase transition according to Ginzburg - Landau theory,[8-10] respectively.

The dielectric constant peaks indicate the ferroelectric to paraelectric phase transitions (Curie point, Tc). For LTO, the Tc for heating is observed as 1460 ˚C and for cooling as 1430 ˚C. The Tc during heating is in a good agreement with the literature.[6] From the Curie - Weiss fitting (Insert of Fig.8.3.1 (b)),[10,11] the Curie - Weiss temperature (T_0) is estimated as 1405 ˚C which is lower than Tc during heating . All of this suggests that The Curie transition for LTO is first order. In Ginzburg - Landau theory, the free energy is used to estimate the thermodynamic stability of ferroelectric and paraelectric phases (Fig.8.3.3 (a)). For LTO, only ferroelectric phase exists below T_0. In this temperature range the switching of spontaneous polarization (Ps) becomes easier with increasing temperature, thus contributing to the permittivity (ε) and mechanical loss (D).[12] Between T_0 and Tc, the paraelectric phase could begin nucleating but the main phase is

still ferroelectric. However, the small amount of paraelectric phase can decrease the internal stress and the friction of ferroelectric phase, so that the mechanical loss drops and the permittivity still increases with increasing temperature. The ferroelectric and paraelectric phases coexist at Tc and the paraelectric phase exceeds the ferroelectric to become the main phase between Tc and T_1.[10,11] T_1 is the temperature below which the ferroelectric phase can exist sub-stably. In the end, the ferroelectric phase disappears above T_1. The T_1 of LTO was estimated as 1592 ˚C according to Ginzburg - Landau theory.

For SNO, the Tc (1328 ˚C) measured during heating and cooling were the same, which indicates the ferroelectric to paraelectric phase transition is a second order transition. Different from a first order ferroelectric to paraelectric phase transition, T_0 is the same as Tc and T_1 in a second order transition. The T_0 of SNO was estimated as 1324 ˚C. Therefore, only ferroelectric phase exists below Tc and the paraelectric phase dominates above Tc for SNO.

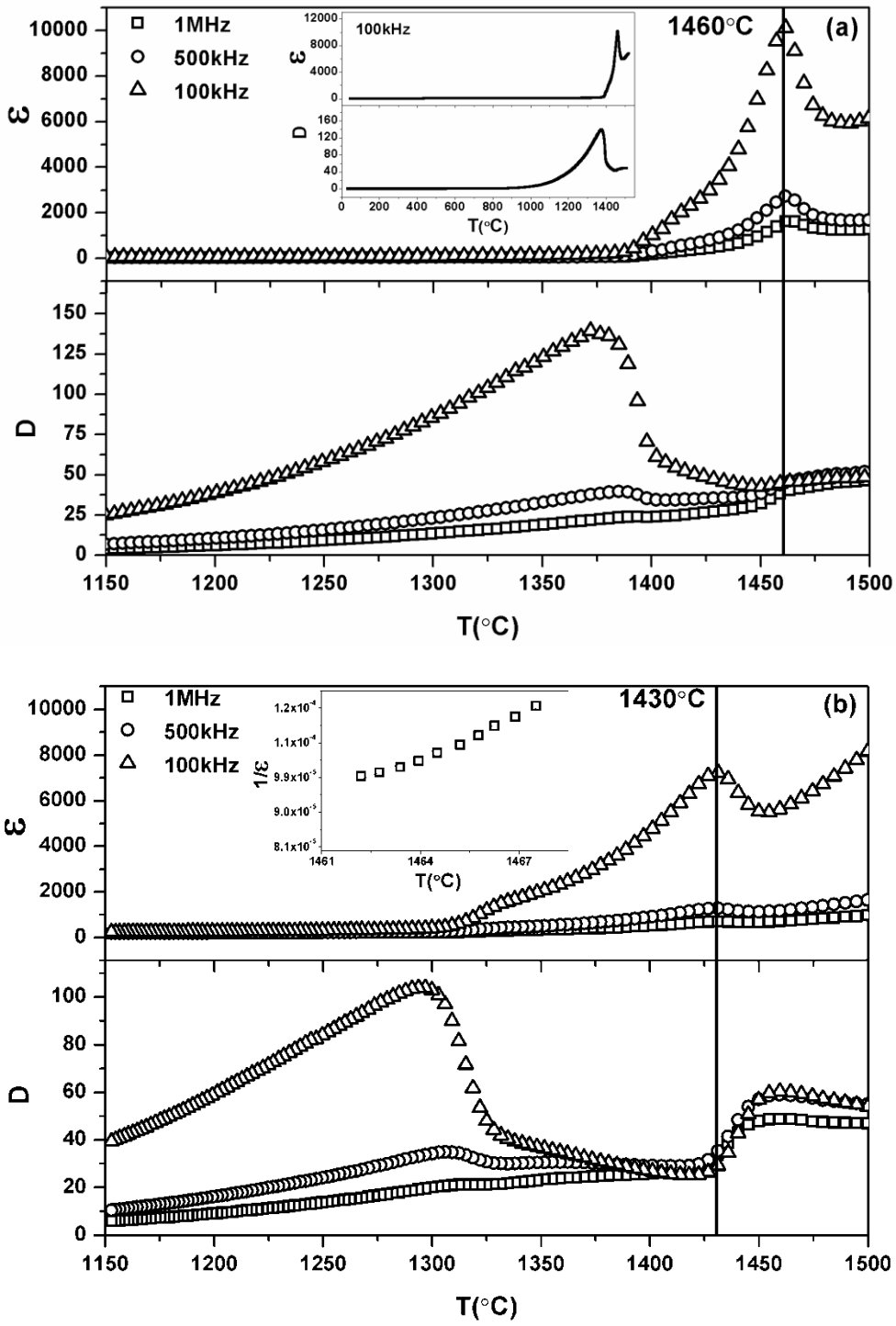

Fig.8.3.1. Dielectric constant and dielectric loss of $La_2Ti_2O_7$ ceramic as function of temperature (1150 - 1500 ˚C) at 1MHz; 500kHz and 100kHz measured During (a) heating and (b) cooling. The insert of (a) is the scan from 25 - 1500 ˚C at 100kHz; and the insert of (b) is 1/ε as a function of temperature above Curie point.

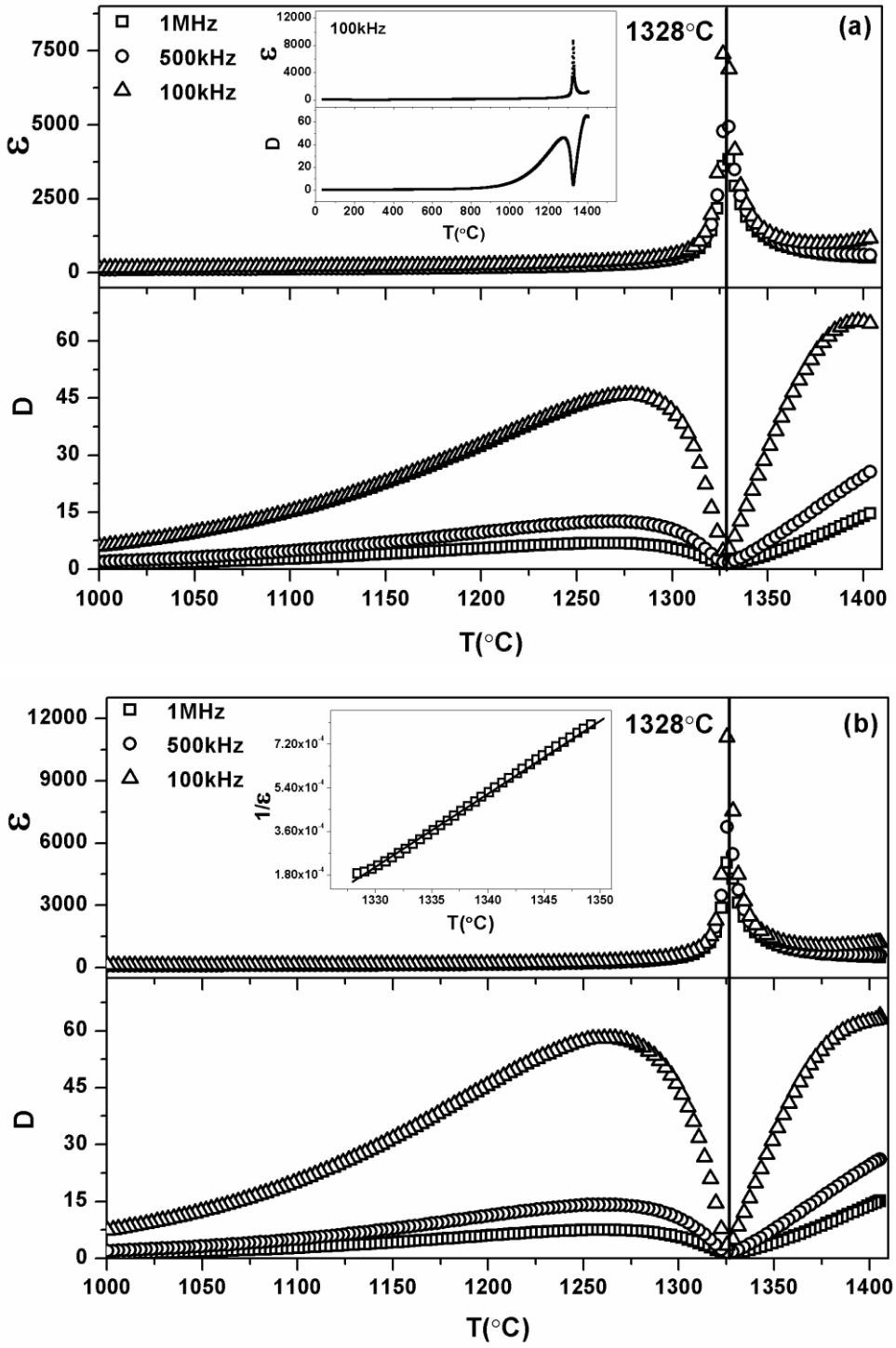

Fig.8.3.2. Dielectric constant and dielectric loss of $Sr_2Nb_2O_7$ ceramic as function of temperature (1000 - 1400 ˚C) at 1MHz; 500kHz and 100kHz measured at (a) heating and (b) cooling processes. The insert of (a) is the scan from 25 - 1400 ˚C at 100kHz and the insert of (b) is the 1/ε as a function of temperature above Curie point.

The plot of relative piezoelectric constant d_{33} of LTO and SNO ceramics to homologous annealing temperature is shown in Fig.8.3.3 (b) and the insert is the real value of d_{33} as a function of temperature. From the insert of Fig.8.3.3 (b) the d_{33} of LTO was measured as 2.6 pC/N at room temperature. With increasing temperature, the d_{33} of LTO is very stable up to the 1540 ˚C which is surprising since this is even above the Tc of LTO. This might be explained by three factors. Firstly, it has a high Tc (1460 ˚C), so the ferroelectric structure of LTO is very stable. It has a first order phase transition at Tc, so the ferroelectric phase, which can stabilize the d_{33}, can exist even above Tc (1460 ˚C) up to T_1 (1592 ˚C). This is also observed in other ferroelectric materials which have a first order transition.[13] Furthermore, there are only 180˚ domains in LTO and all the other PLS structure ferroelectric materials, which can "lock" each other and make the domains difficult to switch.[14,15] This is also supported by its high coercive field (>100 kV/cm) and the difficulty of poling it (220 ˚C, 200 kV/cm). Even if some of the ferroelectric domains disappear above Tc, it costs more energy to re-orientate the domain rather than keep the original direction, which is a kind of memory effect. Therefore, the d_{33} might drop above Tc due to some of the ferroelectric phase disappearing, but it could recover when the temperature is then reversed.

SNO has a different thermal depoling behavior compared to LTO. Its d_{33} was initially measured as 2.8 pC/N at room temperature. It drops by almost a half after annealing at about 200 ˚C due to a ferroelectric to ferroelectric phase transition.[16] The ferroelectric to paraelectric phase transition happens at Tc and the d_{33} drops to zero just below Tc.

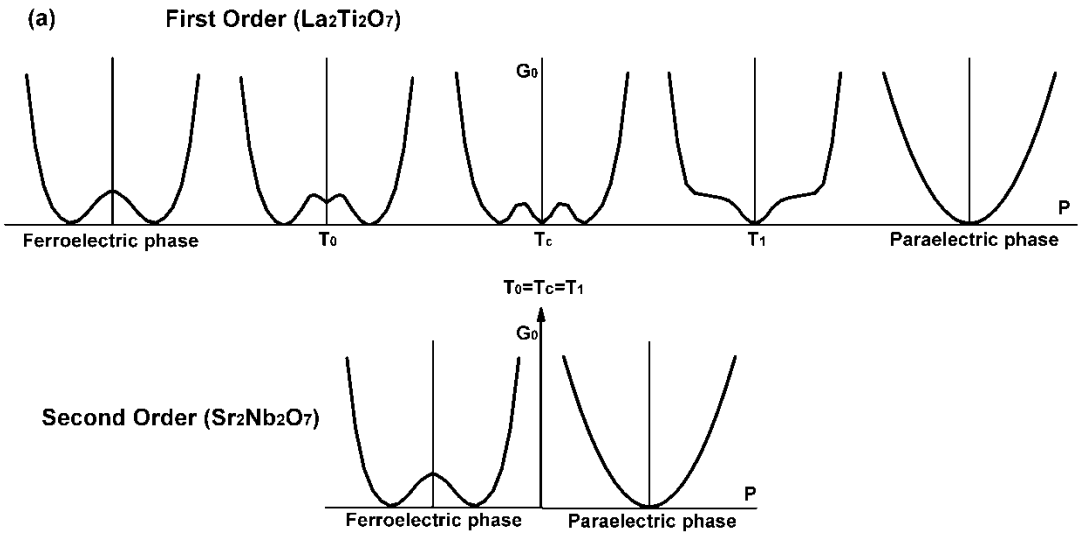

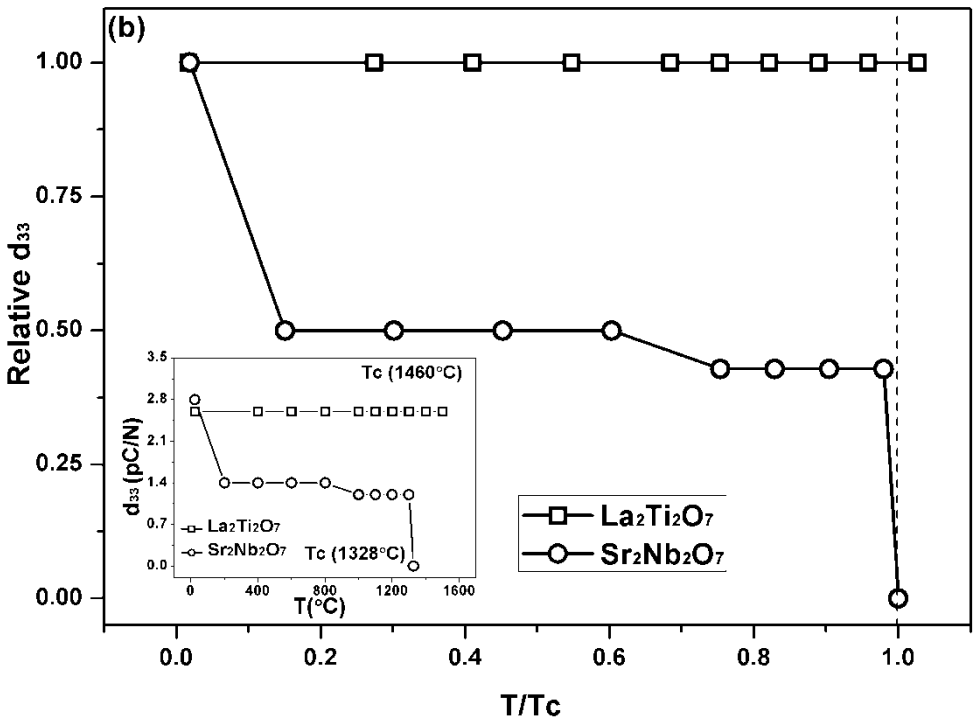

Fig.8.3.3. (a) Free energy (G_0) as a function of polarization (P) for ferroelectric materials. The ferroelectric to paraelectric phase transition is a first order transition for $La_2Ti_2O_7$ and a second order transition for $Sr_2Nb_2O_7$.(b) The plot of relative piezoelectric constant d_{33} of $La_2Ti_2O_7$ and $Sr_2Nb_2O_7$ ceramics to homologous temperature. The insert of (a) is the real value of d_{33} to temperature.

At room temperature LTO has $P2_1$ monoclinic symmetry with the spontaneous polarization (Ps) along the c-axis and lattice parameters are (a, b, c, β) = (7.80Å, 13.011Å, 5.546Å, 98.6 °). It then changes into $Cmc2_1$ orthorhombic symmetry at about 780 ˚C, and then becomes paralelectric phase with Cmcm orthorhombic symmetry at Tc.[2,17,18] SNO crystallizes into an incommensurate, modulated structure with the superspace group $Cmc2_1(\alpha 00)0s0$ at room temperature, with the Ps along the c-axis,.It changes into $Cmc2_1$ orthorhombic symmetry at about 215 ˚C and then changes into the paraelectric phase with Cmcm symmetry at Tc.[16,19-21]

According to the P-E loops results for single crystals, the Ps is reported as 5 $\mu C/cm^2$, and 9 $\mu C/cm^2$ along the c-axes for LTO and SNO, respectively.[1,2,5] However, the results are not accurate if the P-E loops were not saturated. Here, the Ps values for both LTO and SNO are calculated based on their atomic displacements. Atomic displacements along the c-axis from the corresponding positions in the paraelectric structure produce a net spontaneous polarization Ps. Displacements along the a- and b- axes are cancelled out due to the presence of centro-symmetric centers, and therefore do not contribute to the total Ps. Based on the atomic displacements, the total Ps of ferroelectric LTO and SNO were calculated using Shimakawa's model:[22]

$$Ps = \sum_i \frac{m_i \Delta x_i Q_{ie}}{V} \tag{8.1}$$

Where m_i is the site multiplicity and Δx_i is the atomic displacement along the c-axis, Q_{ie} is the ionic charge of the ion, and V is the volume of the unit cell.

According to the crystal structure parameters of LTO and SNO reported by Ishizawa et

al and Daniels et al.[16,21] The ion contribution to the total Ps are represented in Fig.8.3.4 (a-d). At room temperature, LTO and SNO have Ps of 15.4 and 32.2 pC/N, respectively, which are much higher than the previously reported experimental results (Fig.8.3.4.(a)(c)). At 780 ˚C, the Ps of LTO changes slightly to 15.7 pC/N (Fig.8.3.4.(b)). It is worthy to mention here that when the structure of LTO changes from $P2_1$ to $Cmc2_1$, the structure become more symmetric, so the symmetrically unique positions for the ions decrease by a half. For SNO, Ps falls to 21.7 pC/N at 215 ˚C, which can explain the drop of d_{33} at about 200 ˚C (Fig.8.3.4.(d)).

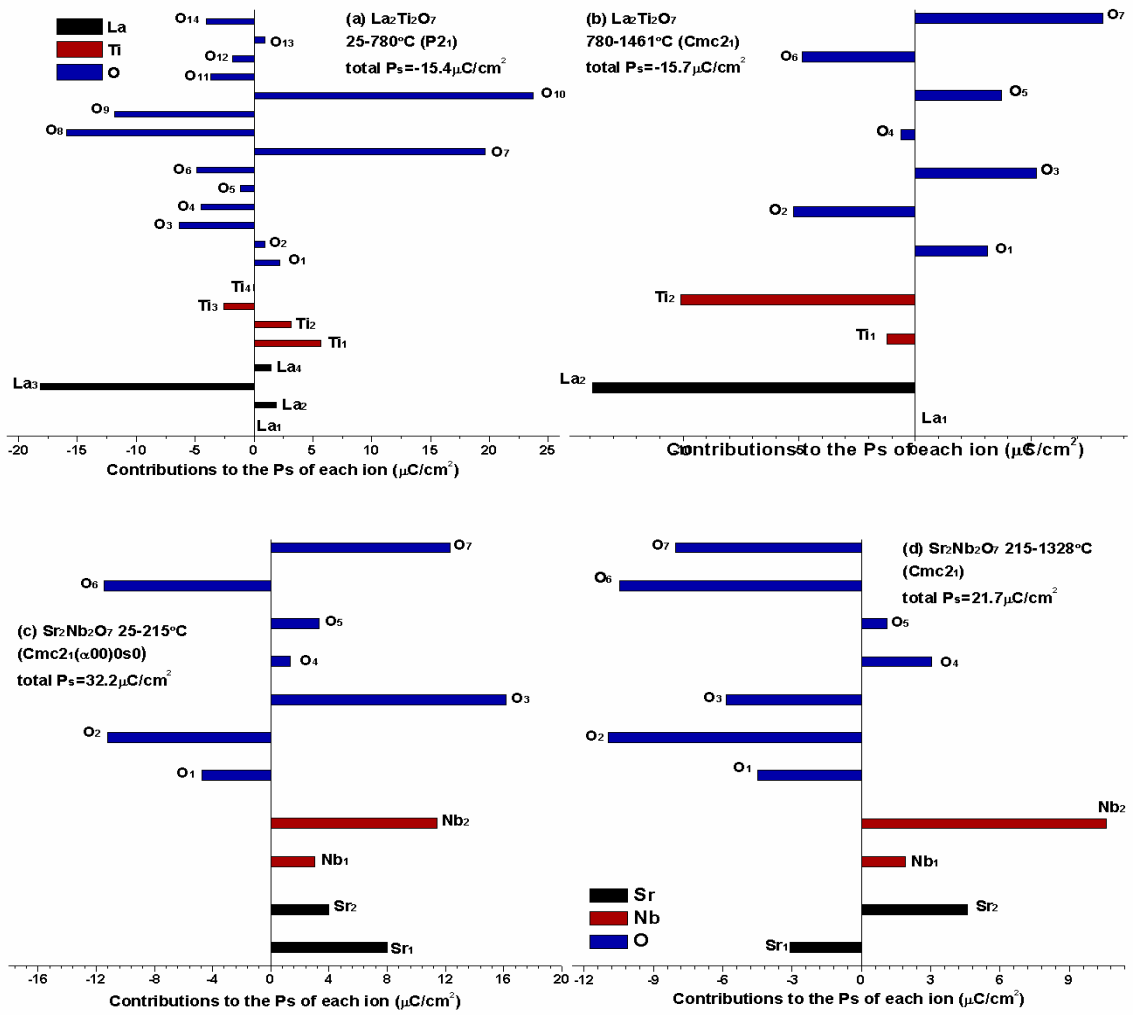

Fig.8.3.4. Ion contribution to total spontaneous polarization (Ps) of each ion of $La_2Ti_2O_7$ and $Sr_2Nb_2O_7$.

8.4.Conclusion

The phase transitions and thermal depoling behaviors of LTO and SNO have been investigated. LTO has a first order ferroelectric to paraelectric phase transition at its Curie point and SNO has a second order phase transition. Their spontaneous polarization have been accurately calculated. Both of them are stable, especially LTO, which make them excellent candidates for high temperature applications.

References

(1). Nanamatsu, S., Kimura, M., Doi, K., and Takahashi, M., *Journal of the Physical Society of Japan*, 1971. **30**: p. 300-301.

(2). Kimura, M., Matsushi, S., Nanamats, S., Takahash, M., and Doi, K., *Japanese Journal of Applied Physics*, 1972. **11**: p. 904-907.

(3). Kimura, M., Nanamats.S, Doi, K., Matsushi. S., Igarashi, S., and Takahash.M., *Nec Research and Development*, 1973. **17**: p. 10-14.

(4). Nanamats, S., Kimura, M., and Yamada, N., *Nec Research and Development*, 1974. **19**: p. 39-42.

(5). Nanamatsu, S., M. Kimura, and T. Kawamura, *Journal of the Physical Society of Japan*, 1975. **38**(3): p. 817-824.

(6). Yan, H., Ning, H., Kan, Y., Wang, P., and Reece, M., *Journal of the American Ceramic Society*, 2009. **92**(10): p. 2270-2275.

(7). Ning, H., Yan, H., and Reece, M., *Journal of the American Ceramic Society*, 2010. **93**(5): p. 1409-1413.

(8). Devonshire, A., *Philosophical Magazine*, 1949. **40**: p. 23-25.

(9). Devonshire, A., *Philosophical Magazine*, 1951. **42**: p. 14-17.

(10). Landau, L., and Lifshitz, E., *Statistical Physics*, Pergamon Press, Oxford, 1980.

(11). Kittel, C., and McEuen, P., *Introduction to solid state physics*, Wiley press, Hoboken, 2005.

(12). Gerthsen, P., Hardtl, K., and Schmidt, N., *Journal of Applied Physics*, 1980. **51**: p.

1131-1134.

(13). Hofer, A., Fechner, M., Duncker, K., Holzer, M., Mertig, I., and Widdra, W., *Physical Review Letters*, 2012. **108**: p. 087602.

(14). Chen, S., Wang, G., and Dong, X., *Ferroelectrics*, 2008. **363**: p. 21-26.

(15). Yan, H., H. Zhang, M.J. Reece, and X. Dong, *Applied Physics Letters*, 2005. **87**(8): p. 082911-3.

(16). Daniels, P., Tamazyan, R., Kuntscher, C. A., Dressel, M., Lichtenberg, F., van Smaalen, S., *Acta Crystallographica Section B-Structural Science*, 2002. **58**: 970-976.

(17). Ishizawa, N., F. Marumo, S. Iwai, M. Kimura, and T. Kawamura, *Acta Crystallographica Section B-Structural Science*, 1982. **38**: p. 368-372.

(18). Lichtenberg, F., Herrnberger, A., Wiedenmann, K., and Mannhart, J., *Progress in Solid State Chemistry*, 2001. **29**: p. 1-70.

(19). Takahash.M, Nanamats.S, and Kimura, M., *Journal of Crystal Growth*, 1971. **13**: p. 681.

(20). Scheunemann, K., and Mullerbuschbaum, H., *Journal of Inorganic and Nuclear Chemistry*, 1975. **37**: p. 1679-1680.

(21). Ishizawa, N., Marumo, F., Kawamura, T., and Kimura, M., *Acta Crystallographica Section B-Structural Science*, 1975. **31**: p.1912-1915.

(22). Shimakawa, Y., Kubo, Y., Nakagawa, Y., Goto, S., Kamiyama, T., Asano, H., and Izumi, F., *Physical Review B*, 2000. **61**: p. 6559-6564.

Chapter IX. Results – Resistivity, electrical degradation and conductivity mechanism of $Sr_2Nb_2O_7$

9.1. Introduction

The thermal stability of high temperature piezoelectrics is very important due to their high operating temperatures. In dielectric and piezoelectric ceramics, different failure modes can be induced by electric field and temperature. Dielectric breakdown is an instantaneous breakdown caused by the applied electric field exceeding the dielectric strength of the material.[1] Thermal breakdown is produced by self-heating due to a high leakage current in a dielectric material at high temperature.[1] Resistivity degradation is characterized by an increase of the leakage current under certain temperature and DC electric field, even if the temperature and electric field are much lower than the critical values for dielectric or thermal breakdown (Fig.9.1.1).[1] Because they represent limiting conditions for their application, both the dielectric and thermal breakdown are not serious problems during operation. However, degradation is a time dependent phenomenon that limits the lifetime of dielectric and piezoelectric materials.

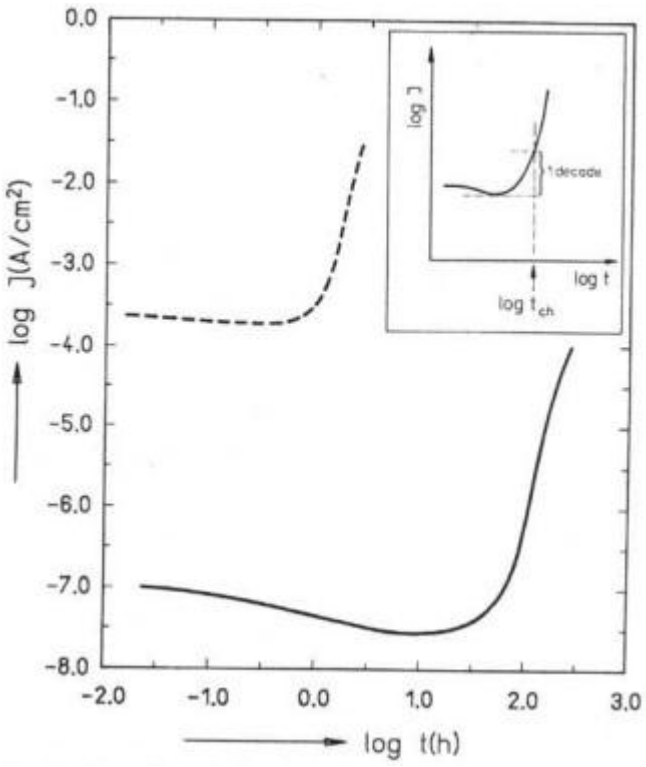

Fig.9.1.1. Example of the degradation of barium titanate; current density J vs time t at a temperature T = 210 ˚C and a DC electric field E = 8.0 kV/cm. Solid line is (BaCa)(TiZr)O_3 ceramic and dash line is $SrTiO_3$ ceramic.[1]

The first report on the insulation resistance degradation of $BaTiO_3$ was published in 1951.[2] Since then, there have been several reports for perovskite titanates.[1,3,4] Generally, the rate of the degradation increases with increasing temperature and DC field. The degradation rate can be affected by material parameters, such as, doping, grain size, second phases, porosity as well as electrode properties.[1,4-6] In most cases, donor doping can stabilize the resistivity while acceptor doping increases the degradation rate. There is still an argument as to whether grain size can affect the degradation of resistivity. Porosity in ceramics was reported to stimulate the degradation.[4]

Based on these studies, several theories were proposed to explain the degradation mechanism, which could be generally classified into two major categories. The first one

is the grain – boundary model.[3] Grain boundaries generally exhibit higher resistivity than the bulk of the grains. After a DC electric field is applied, the electrons may concentrate on the grain boundary and a high electrical field across the grain boundaries can be established. This phenomenon is known as Maxwell – Wagner polarization.[7] The model assumes that the local field leads to a breakdown process.

The Reduction model considers oxygen vacancies with relatively high mobility.[4,6,8] Oxygen vacancies widely exist in titanate ceramics.[9] They are positively charged and move towards the cathode. The oxygen vacancies pile up at the cathode and are oxidized by electrons injected from the cathode.[1] Conversely, the oxygen vacancies are produced at the anode in the reaction:

$$O_O \rightarrow \frac{1}{2}O_2(g) + V_O^{\bullet\bullet} + 2e' \qquad (9.1)$$

Therefore, the ceramic suffers an electrochemical reduction, which produces a growth of the n-conducting cathode region toward the anode. This increases the electronic conductivity.

According to Rainer Waser's study of perovskite - type titanates, the migration of oxygen vacancies across grain boundaries is rate - limiting for the degradation process and the electric potential drop per grain boundary is the key parameter for the degradation rate.[1] So, the grain boundary model is more consistent with the results.

For the $A_2B_2O_7$ PLS materials, many of them have high Tc and are good candidates for high temperature sensor materials.[10-12] Therefore, their high temperature degradation

properties are important and there are no reports on this in the literature. In this chapter, $Sr_2Nb_2O_7$ was chosen to study high temperature (> 400 ˚C) electric degradation due to its relatively high d_{33} and excellent dielectric properties. The dielectric properties have also been investigated to help to understand the conductivity mechanisms.

9.2. Experiment Details

The $Sr_2Nb_2O_7$ (SNO) was obtained by the mixed oxide route. The powders were ball milled and then calcinated for 4.5 h at 1250 ℃. The powders were then re-milled to break any agglomerates and reduce the particle size. The calcined SNO powder was sintered using a two-step method in the SPS furnace.[10]

The electrical stability measurements were carried out by holding the samples at different temperatures and measuring their resistance as a function of time. The voltages of 20V, 40V and 80V were used. All the SNO textured samples used for the electrical stability tests had the same electrode area (15 mm^2) and thickness (0.6 mm). The DC conductivity was calculated from the DC resistivity of SNO. The resistance data was recorded at 20 V after holding at different temperatures for 15 min.

The frequency dependent permittivity was obtained at different temperatures between 25 – 800˚C. The real part (ε') of permittivity and loss (D) were recorded and the imaginary part (ε'') could be calculated using the following equation:

$$\varepsilon'' = D\varepsilon' \tag{9.2}$$

The frequency dependent permittivity was collected after holding at different temperatures for 15min.

9.3. Results and Discusstion

The electrical stability of SNO was measured under 20V, 40V and 80V at 400 ℃, 600 ℃, and 800 ℃, with a holding time for 24 h (Fig.9.3.1 - 9.3.3). It was observed that the resistivity of SNO is very stable during the holding period at all of the conditions. The resistivity of SNO is about 9×10^8 Ω.cm at 400 ℃, 5×10^7 Ω.cm at 600 ℃, and 2×10^6 Ω.cm at 800 ℃ respectively under 20 V (Fig.9.3.1). The value is about 10^9 Ω.cm at 400 ℃, 7×10^7 Ω.cm at 600 ℃, and 2×10^6 Ω.cm at 800 ℃ under 40 V (Fig.9.3.2), while it is 1.5×10^9 Ω.cm at 400 ℃, 7.5×10^7 Ω.cm at 600 ℃, and 2×10^6 Ω.cm at 800 ℃ under 80 V. All the values are in a good agreement with the literature.[10] The resistivity decreases with increasing temperature; this is because more charge carriers are activated at higher temperature. At the same temperatures, the resisitivities change slightly under different DC field and they are almost the same under 80V. This is because of the experimental error. The resistivity is calculated from the current and voltage in the tests, but the resistivity of SNO is very high, so the current is very low during the tests at 20V and 40V.

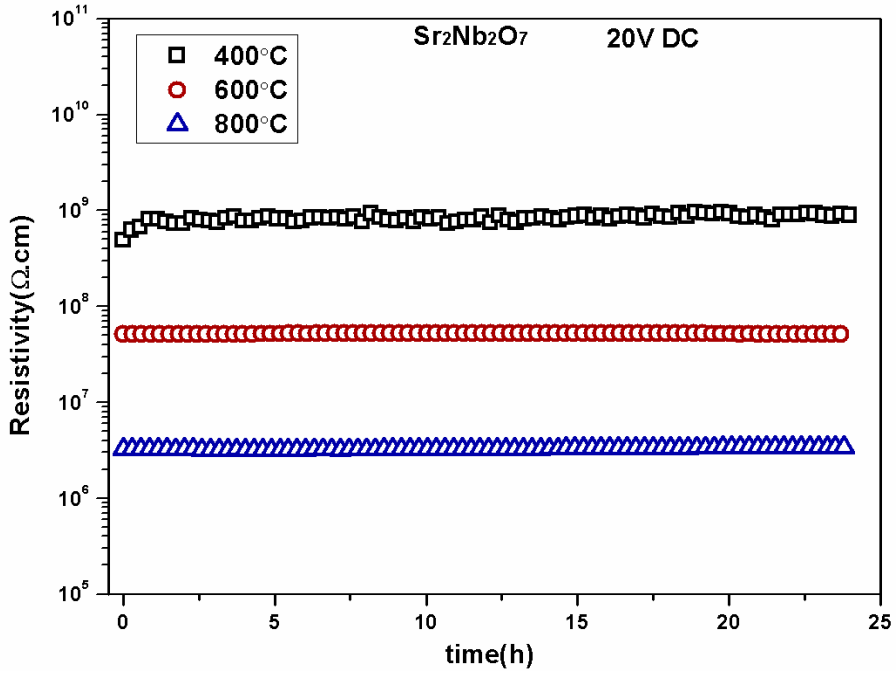

Fig.9.3.1. Electrical stability of SNO textured ceramics (⊥) measured under 20V at 400 ℃, 600 ℃, and 800 ℃.

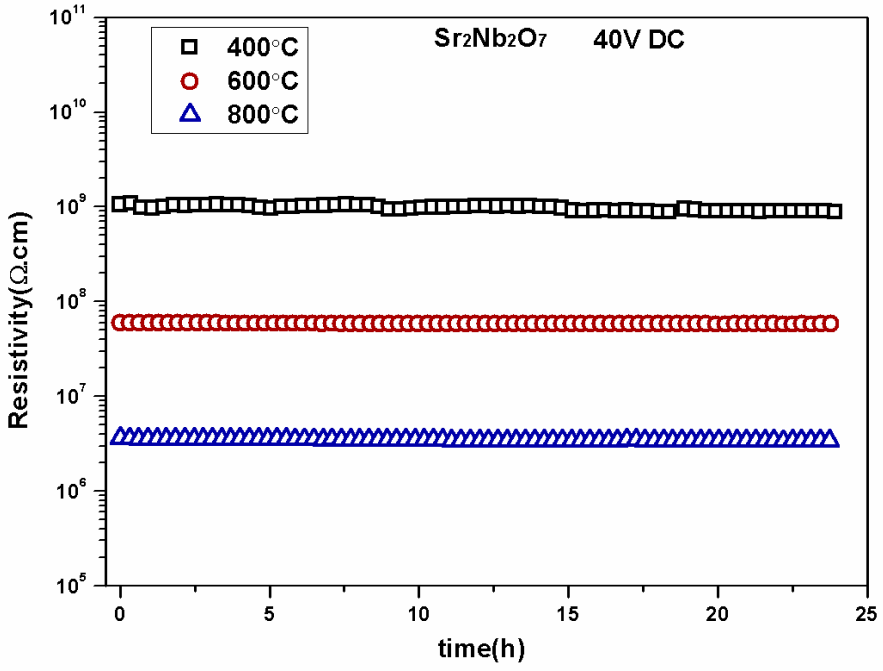

Fig.9.3.2. Electrical stability of SNO textured ceramics (⊥) measured under 40V at 400 ℃, 600 ℃, and 800 ℃.

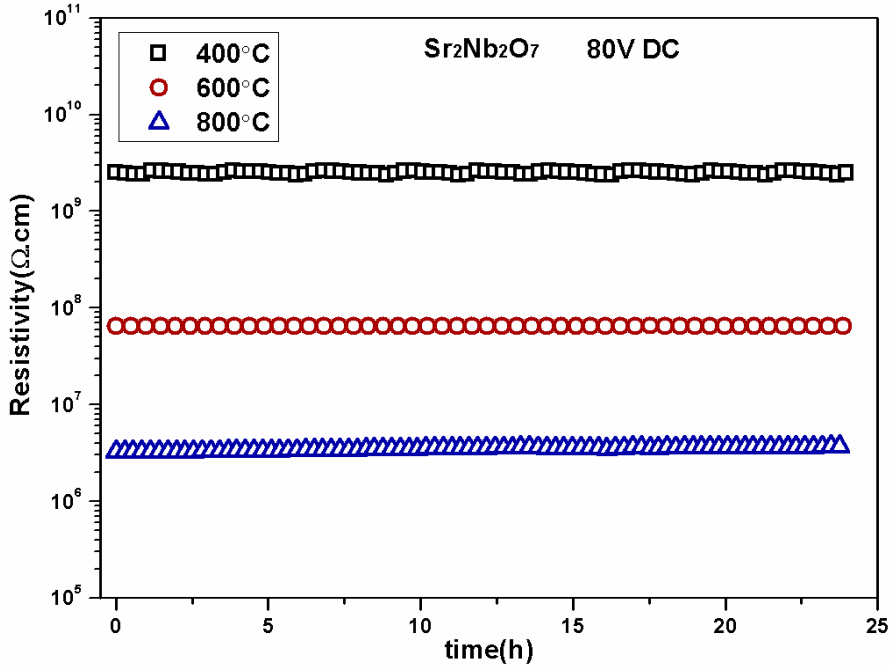

Fig.9.3.3. Electrical stability of SNO textured ceramics (⊥) measured under 80V at 400 ℃, 600 ℃, and 800 ℃.

The result of long term experiments at 800 ℃, 80V is shown in Fig.9.3.4. There is no obvious resistivity drop observed during 125 h. Fig.9.3.5 shows the stability measured under 80V at 980 ℃ and 1000 ℃ respectively. The resistivity degradation can be observed after 14 hours holding at 980 ℃ and just 0.6 hour at 1000 ℃. The experimental results suggest that SNO could be used below 800 ℃ for application.

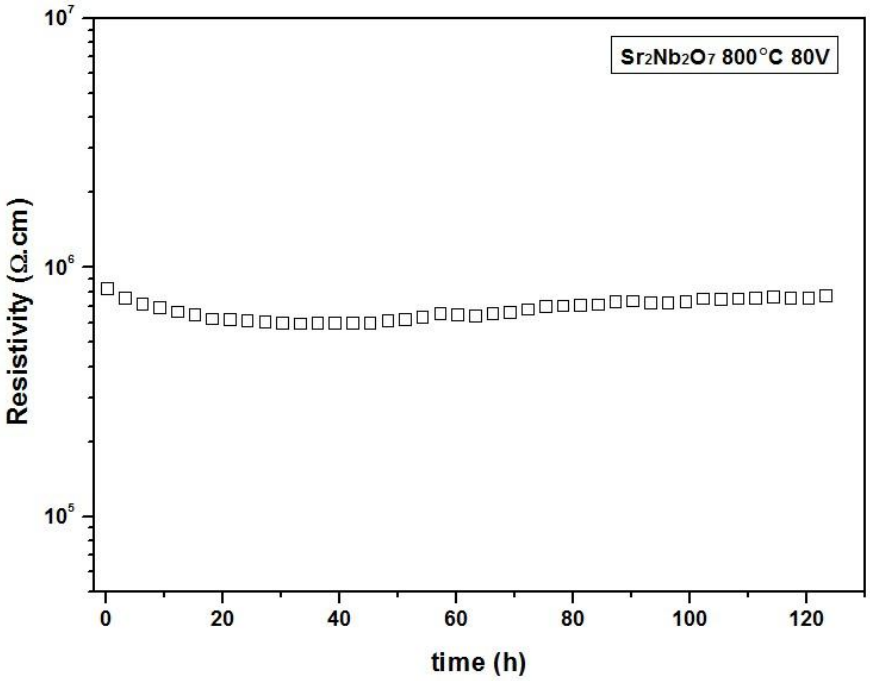

Fig.9.3.4. Electrical stability of SNO textured ceramic (⊥) measured under 80V at 800 ℃ for 125 hours.

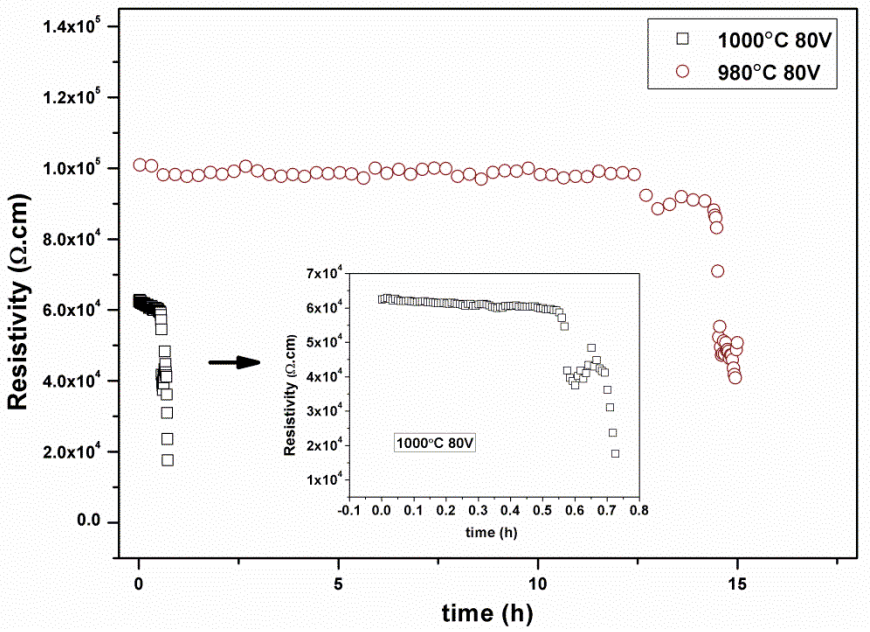

Fig.9.3.5. Electrical stability of SNO textured ceramic (⊥) measured under 80V at 980 ℃ and 1000 ℃.

Fig.9.3.6 shows the electrical degradation results for SNO textured ceramics in perpendicular direction (SPS (⊥)) and parallel direction (SPS (//)). The value of resistivity in SPS (//) is higher than SPS (⊥). This is because the SNO has PLS structure and the layer structured direction has higher electrical resistivity in single crystal.[13,14] Also, the grains in PLS material are plate-like and are orientated in the textured ceramic. In this case, the grain boundary density in SPS (//) is higher than SPS (⊥), so the resistivity in SPS (//) is higher than SPS (⊥) (Fig.9.3.7).[12] The degradation time for the SPS (//) is longer than SPS (⊥). This result is in good agreement with Rainer Waser's study.[1,3] There is a local field established on the grain boundary and the electric potential drop at the grain boundary is the key parameter for the degradation (Fig.9.3.7). In the parallel direction (//), the grain boundary density is much higher than in perpendicular direction (⊥) and the voltage is the same, so the electric potential drop on each grain boundary is smaller in SPS (//) than SPS (⊥). As grain - boundary theory, this local electric field is smaller and degradation time is longer. So, the resistivity degradation time is longer in in SPS (//) than SPS (⊥).

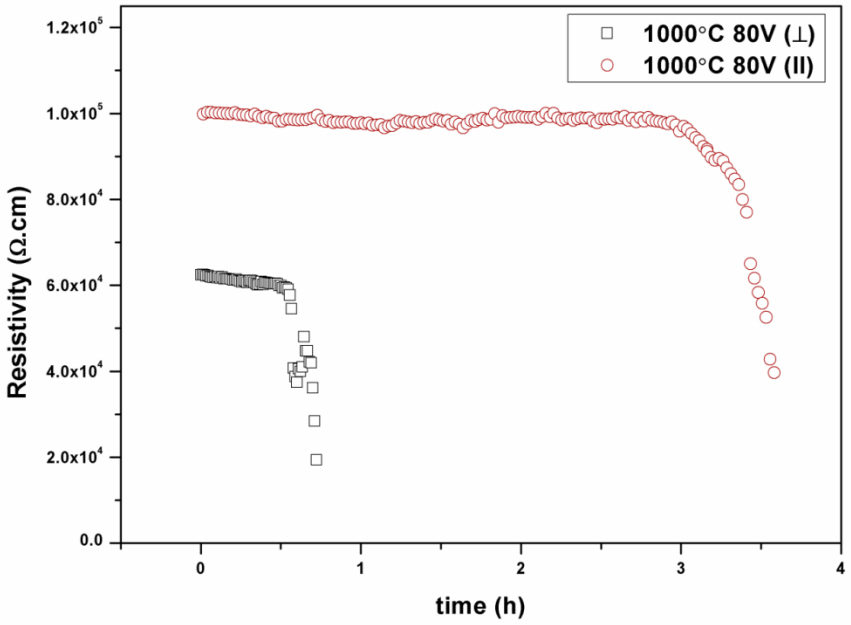

Fig.9.3.6. Electrical stability of SNO textured ceramic measured under 80V at 1000 ℃ in parallel direction (//) and perpendicular direction (⊥).

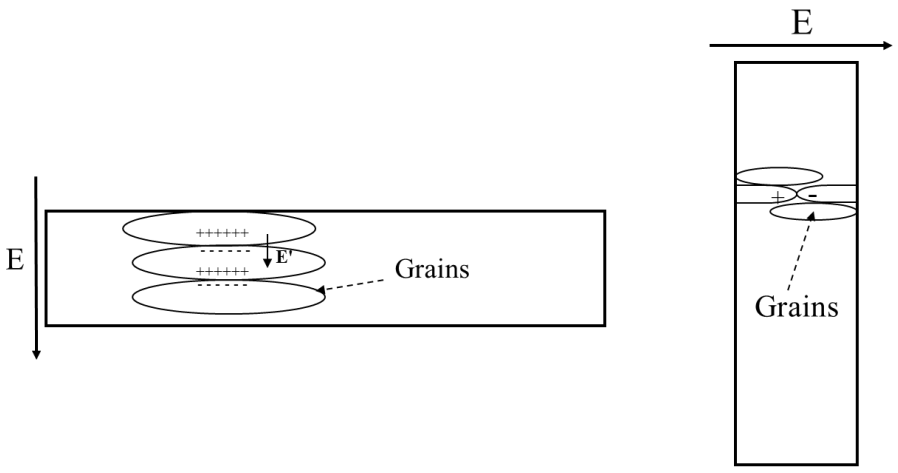

a). Parallel direction (//) b). Perpendicular direction (⊥)

Fig.9.3.7. Diagrammatic sketch of (a). SPS (//) and (b). SPS (⊥) samples under the applied DC field (E). E' is the local field established on the grain boundaries.

The frequency dependence of dielectric constant real part (ε') and imaginary part (ε'') measured at different temperatures is shown in Fig.9.3.8. The ln σ_{AC} to 1/T plots is shown in Fig.9.3.9. Here, T is the absolute temperature and σ_{AC} is the estimated

contribution to the AC conductivity from the dielectric loss, which was calculated using following equation:[15]

$$\sigma_{AC} = 2\pi f \varepsilon'' \varepsilon_0 \tag{9.3}$$

Here, ε'' is the imaginary part of permittivity; f is the frequency and ε_0 is the vacuum dielectric constant.

The activation energy of AC or DC conductivity can be calculated using the Arrhenius relation:[16]

$$\begin{aligned} &\sigma = \sigma_0 \exp(-\frac{Ea}{kT}) \\ &\Rightarrow \ln\sigma = \ln\sigma_0 - \frac{Ea}{kT} \end{aligned} \tag{9.4}$$

Here, σ_0 is a constant; k is the Boltzmann constant; T is the absolute temperature and Ea is the activation energy.

From Fig.9.3.9, three frequencies (100Hz, 1000Hz, 10000Hz) have been chosen to calculate the activation energy. The activation energy ($Ea_{(AC)}$) is 0.25eV, 0.28eV and 0.37eV at 10000Hz, 1000Hz and 100Hz respectively. Fig.9.3.10 shows the DC conductivity change with temperature increasing and the insert is the plots of $\ln(\sigma_{DC})$ to 1/T. From the equation (3), the slop is the activation energy for DC conductivity ($Ea_{(DC)}$) which is 1.0eV. The activation energy is smaller than the activation energy for intrinsic charge carriers (~1.44 eV),[16] which reflects the DC conductivity is dominated by the extrinsic charge carriers.

$Ea_{(AC)}$ are much smaller than $Ea_{(DC)}$ which means the charge carriers of AC conductivity are different from DC conductivity. Actually, the DC conductivity always contributes to the AC conductivity, but there are some other charge carriers, which cannot move long-range, that contribute to the AC conductivity. This is consistent with the results that the DC conductivity is much lower than AC conductivity and the activation energy for DC is much higher than AC. In our case, the real and imaginary permittivity both decrease with increasing frequency which means that the defect can only follow at low frequency and cannot respond with increasing frequency. The permittivity increases with increasing temperature and indicates more dipoles are activated at high temperature. All the switchable dipoles could contribute AC conductivity.

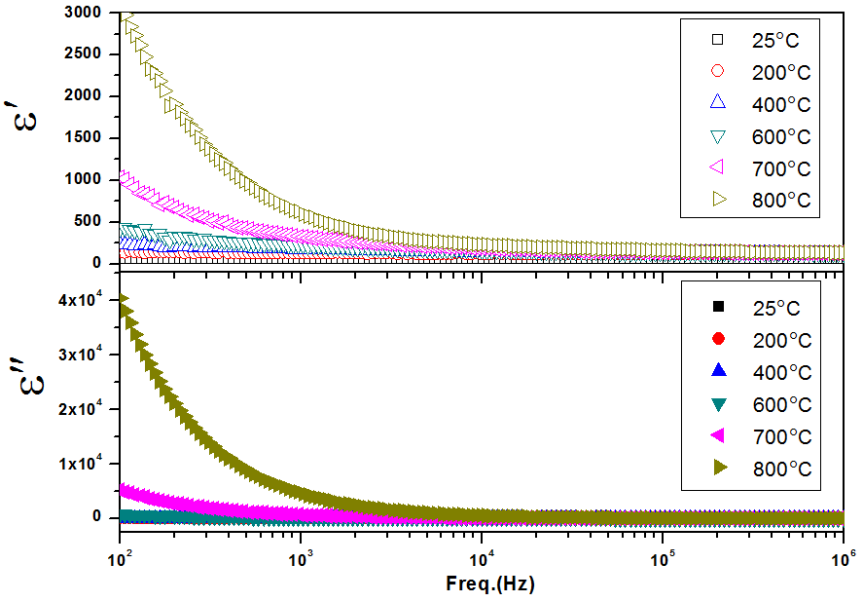

Fig.9.3.8. The frequency dependence of dielectric constant real part (ε′) and imaginary part (ε") measured at different temperatures.

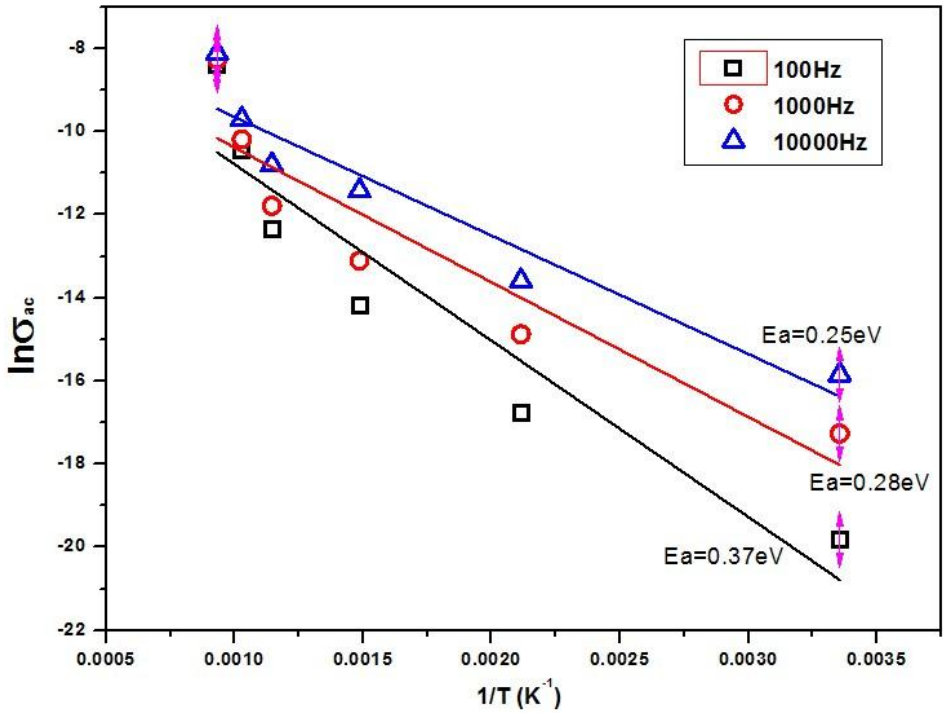

Fig.9.3.9. The plots of ln σ_{AC} to 1/T.

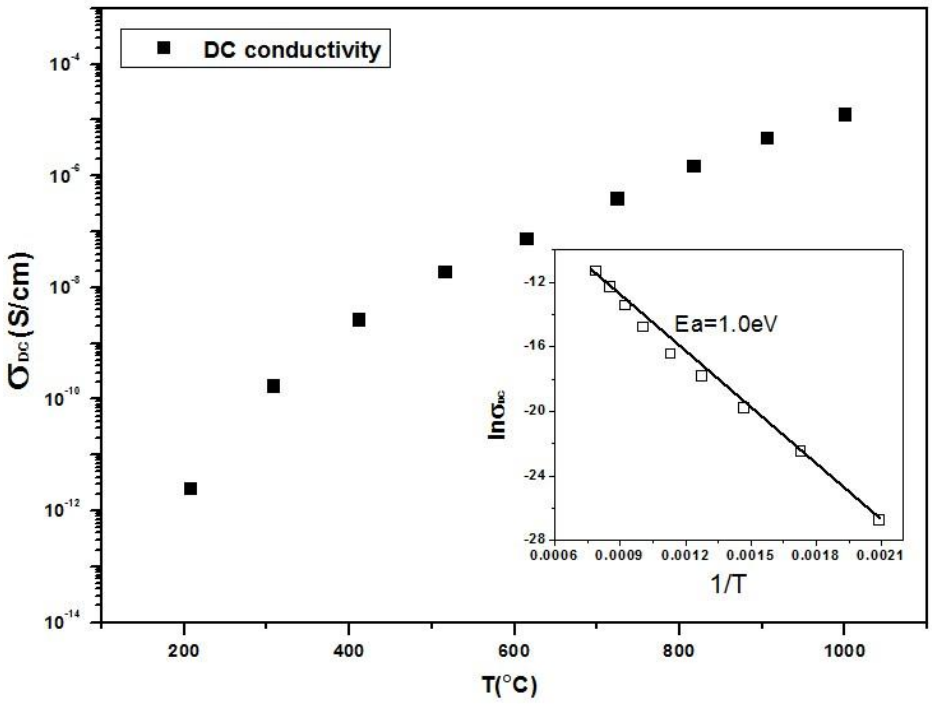

Fig.9.3.10. The DC conductivity change with temperature increasing. The insert is the plots of ln σ_{DC} to 1/T.

9.4. Conclusion

In this chapter the electric stability of SNO has been investigated. The experimental results suggest that SNO could be used in applications below 800 ℃. The degradation mechanism of SNO can be explained by the grain boundary model. The AC conductivity of SNO is dominated by dipole hopping. The activation energy for DC conductivity suggests that DC conductivity is dominated by extrinsic charge carriers.

Reference

(1). Waser, R., *Journal of the American Ceramic*, 1990. **73**: 8-15.

(2). Bunting, E., Sheltonl, G., Creamerl, A., and Jaffe, B., *Journal of Research of the National Bureau of Standards*, 1951. **47**: p. 10-13.

(3). Loh, E., *Journal of Applied Physics*, 1982. **53**: p. 7-10.

(4). Macchesney, J., Gallagher, P., and Dimarcello, F., *Journal of the American Ceramic*, 1963. **46**: 6-8.

(5). Waser, R., *Journal of the American Ceramic*, 1990. **73**: 8-13.

(6). Li, J., Zhao, X., Gu, F. and Li, S., *Applied Physics Letters*, 2012. **100**(20): p. 202905 - 202905-4.

(7). Neumanna, H., and Arlta, G., *Ferroelectrics*, 1986. **69**: p. 179-186.

(8). Harmera, M., Hua, Y., Lala, M., and Smytha, D., *Ferroelectrics*, 1983. **49**: 71-74.

(9). Lee, H., *IEEE Transactions on Components, Hybrids, and Manufacturing Technology*, 1986. **9**: p. 469-474.

(10). Ning, H., Yan, H., and Reece, M., *Journal of the American Ceramic Society*, 2010. **93**(5): p. 1409-1413.

(11). Yan, H., Ning, H., Kan, Y., Wang, P., and Reece, M., *Journal of the American Ceramic Society*, 2009. **92**(10): p. 2270-2275.

(12). Nanamatsu, S., Kimura, M., Doi, K., Takahashi, M., *Journal of the Physical Society of Japan*, 1971. **30**: p. 300-301.

(13). Lichtenberg, F., A. Herrnberger, and K. Wiedenmann, *Progress in Solid State Chemistry*, 2008. **36**(4): p. 253-387.

(14). Lichtenberg, F., Herrnberger, A., Wiedenmann, K., and Mannhart, J., *Progress in Solid State Chemistry*, 2001. **29**: p. 1-70.

(15). Levstik, A., Filipic, C., Bobnar, V., Drnovsek, S., Holc, J., and Kosec, M., *Physica. B, Condensed Matter*, 2010. **405**: p. 4271-4273.

(16). Jeong, E. D., Ha, M. G., Won, M. S., Kim, H. G., Pak, H. K., Borse, P. H., Ji, S. M., and Lee, J. S., *Journal of the Korean Physical Society*, 2006. **49**: p. S671-S674.

Chapter. X. Conclusion and Future work

10.1. Conclusions

In this project, the ferroelectric ceramics of $Pr_2Ti_2O_7$, $La_2Ti_2O_7$, $Sr_2Nb_2O_7$, $La_{2-x}Ce_xTi_2O_7$ (x=0.15, 0.25, 0.35), $Nd_{2-x}Ce_xTi_2O_7$ (x=0.05, 0.25, 0.5, 0.75) and $Sr_{2-x}Ba_xNb_2O_7$ (x=0.1, 0.2, 0.3, 0.4, 0.5) were prepared. All of the compounds have a perovskite-like layered structure (PLS). For $Pr_2Ti_2O_7$ and $Sr_{2-x}Ba_xNb_2O_7$, the grains are plate-like. However, the grains of $La_{2-x}Ce_xTi_2O_7$ and $Nd_{2-x}Ce_xTi_2O_7$ are less plate-like compared to the unsubstituted compounds, $La_2Ti_2O_7$ and $Nd_2Ti_2O_7$, which is due to the influence of Ce substitution. All the compounds can be textured by a two-step sintering method using SPS. Generally, the compounds with more plate-like grains have a higher degree texture. The two step texture method was proved to be a good way to texture PLS ceramics.

The lattice parameters were calculated based on the XRD data. The structure changes with substitution in all the solid solution systems. Ce substitution can decrease the cell volume in $La_{2-x}Ce_xTi_2O_7$, but increase cell volume in $Nd_{2-x}Ce_xTi_2O_7$. In $Sr_{2-x}Ba_xNb_2O_7$, the volume increases with increasing Ba substitution. In this study, the substituted elements are in the same periodic group as substituting elements. The ions therefore have similar properties and the structure change can be explained by the difference in ion size on the A site. The ionic radius of Ce^{3+} is smaller than that of La^{3+}, but larger than that of Nd^{3+}, while Ba^{2+} is much bigger than Sr^{2+}.

The electrical, piezoelectric and ferroelectric properties were characterized for these materials. $Pr_2Ti_2O_7$ has the highest Curie point know of any known material, which is greater than 1560 ℃. In $La_{2-x}Ce_xTi_2O_7$($x < 0.35$), $Nd_{2-x}Ce_xTi_2O_7$($x < 0.75$), and $Sr_{2-x}Ba_xNb_2O_7$ ($x < 0.6$) solid solution systems, all the substitutions decrease the Curie point. The piezoelectric constant for $Pr_2Ti_2O_7$ is small, 0.5 ± 0.1pC/N. In these solid solution systems, though the Tc decreases, the piezoelectric activity is improved. The highest d_{33} values were 3.9 ± 0.1pC/N and 3.6± 0.1pC/N for $La_{1.85}Ce_{0.15}Ti_2O_7$ and $Sr_{1.8}Ba_{0.2}Nb_2O_7$, respectively which are higher than the d_{33} values of $La_2Ti_2O_7$ (2.6± 0.1pC/N) and $Sr_2Nb_2O_7$ (2.8± 0.1pC/N). The Tc and d_{33} change in $Sr_{2-x}Ba_xNb_2O_7$ could be explained by the spontaneous polarization decreasing and domain mobility increasing with increasing Ba substitution. The resistivities decrease sharply with increasing Ce substitution in both $La_{2-x}Ce_xTi_2O_7$($x < 0.35$) and $Nd_{2-x}Ce_xTi_2O_7$($x < 0.75$) systems. With Ba substitution, the drop of resistivity is not very obvious in $Sr_{2-x}Ba_xNb_2O_7$ ($x < 0.6$). This is because the Ce has two possible valencies of Ce^{3+} and Ce^{4+} existing in the materials, so it acts as donor dopant in contrast to the situation in $Sr_{2-x}Ba_xNb_2O_7$ wheresimple isovalent substitution occurs.

The phase transitions and thermal depoling behaviors of $La_2Ti_2O_7$ and $Sr_2Nb_2O_7$, have been investigated. $La_2Ti_2O_7$ has a first order ferroelectric to paraelectric phase transition at its Curie point and $Sr_2Nb_2O_7$ has a second order transition. $La_2Ti_2O_7$ is super stable which makes it an excellent candidate for high temperature applications. The spontaneous polarizations of $La_2Ti_2O_7$ and $Sr_2Nb_2O_7$ have been calculated.

Overall, all the compounds have a high Tc (>900 ˚C) and the properties can be changed by the substitution. Some of the compounds in solid solution systems have very good ferroelectric and piezoelectric properties. This project makes a further contribution on the study of PLS ferroelectric materials for high temperature applications and has identified candidate materials for these applications.

10.2. Recommendations for Future work

10.2.1.TEM study

There is limited information of the TEM study on $A_2B_2O_7$ ferroelectrics. Most of $A_2B_2O_7$ materials have very high Curie point and the PLS structure. The 180 ^{o}domains are only suggested rather than observed. So the transmission electron microscopy (TEM) study is recommended to utilize to obtain more information on the ferroelectric domain structure. The information might be helpful to analyse why these materials have such stable structure and high Curie points.

10.2.2. Two and three layers PLS ferroelectrics

In the PLS family, some of the two and three layer compounds ($LaTaO_4$, $LaNbO_4$, $Pr_3Ti_2TaO_{11}$, $La_3Ti_2TaO_{11}$) were reported to have noncentro-symmetric structure, which make these materials potential ferroelectrics. However, little information is available on the ferroelectric properties of the two and three layers ferroelectrics due to the difficultly of processing them and inaccessible poling conditions. However, it may be possible to obtain good ferroelectric and piezoelectric properties in these unexplored materials.

10.2.3. Electrical Degradation and Thermal depoling

The electrical degradation behavior is critical for applications. The high temperature electrical stability of $Sr_2Nb_2O_7$ was studied in this project. The degradation of resistance

depends on both intrinsic parameters (defects, grain size) and extrinsic parameters. It is also a statistical process. It would therefore be useful to perform a more systematic study in order to identify the mechanisms of degradation.

The thermal depoling behaviours $Sr_2Nb_2O_7$ and $La_2Ti_2O_7$ have been studied, but why $La_2Ti_2O_7$ is super stable is not clear. Further research is needed to answer this question.

10.2.4 Grain size effect

The grain size effect could significantly affect the ferroelectric and dielectric properties on ferroelectrics. It is poorly studied in PLS family. Hence, it would be very useful to investigate the influence of grain size on the electrical properties of these $A_2B_2O_7$ ceramics, as well as the effect on their ferroelectric domain structure. SPS is a good method to prepare the ceramics with nano-size grains due to the high heating rate and pressure.

List of My Publications

1. H. Yan, F. Inam, G. Viola, H. Ning, H. Zhang, Q. Jiang, T. Zeng, **Z. Gao** and M.J. Reece, "Contribution of Electrical Conductivity, Dielectric Permittivity and Domain Switching in Ferroelectric Hysteresis Loops" *Journal of Advanced Dielectrics*, 1, 107-118 (2011).

2. **Z. P. Gao**, H. X. Yan, H. P. Ning and M. J. Reece, "Ferroelectricity of $Pr_2Ti_2O_7$ Ceramics with Super-High Curie Point" *Advances in Applied Ceramics*, Doi: http://dx.doi.org/10.1179/1743676112Y.0000000030 (2012).

3. **Z. P. Gao**, G. Viola, B. Milsom, I. Whitaker, H. Yan and M. J. Reece, "Kinetics of Densification and Grain Growth of Pure Tungsten During Spark Plasma Sintering" *Metallurgical and Materials Transactions B*, Doi: 10.1007/S11663-012-9704-9 (2012).

4. B. Milsom, G. Viola, **Z. P. Gao**, F. Inam and T. Peijs**, "**The effect of carbon nanotubes on the sintering behaviour of zirconia" *Journal of the European Ceramic Society*, 32, (16) 4149-4156 (2012).

5. **Z. P. Gao**, H. P. Ning, C. Chen, R. Wilson, B. Shi, H. Ye, H. X. Yan and M. J. Reece, "The effect of Barium substitution on the ferroelectric properties of $Sr_2Nb_2O_7$ ceramics" *Journal of American Ceramic Society*, Doi: 10.1111/jace.12121 (2012).

6. **Z. P. Gao**, H. X. Yan, H. P. Ning, R. Wilson, X. Y. Wei, B. Shi, H. Ye and M. J. Reece, "Piezoelectric and dielectric properties of Ce substituted $La_2Ti_2O_7$ ceramics" *Journal of the European Ceramic Society*, Doi: 10.1016/j.jeurceramsoc.2012.11.015 (2012).